Development of advanced nanofiltration membranes for Mg^{2+}/Li^{+} separation

房，上

(Degree)
博士（学術）

(Date of Degree)
2024-09-25

(Date of Publication)
2025-09-01

(Resource Type)
doctoral thesis

(Report Number)
甲第9027号

(URL)
https://hdl.handle.net/20.500.14094/0100492536

Doctoral Dissertation

Development of advanced nanofiltration membranes for Mg^{2+}/Li^{+} separation

(Mg^{2+}/Li^{+}分離のための革新的ナノろ過膜の開発)

July 2024

Graduate School of Engineering

Kobe University

FANG SHANG

房 上

Acknowledgment

Today, my doctoral studies are coming to an end, leaving me with many emotions. It is a great honor to have been a doctoral student at Kobe University. This journey of learning has been an unforgettable time in my life. As this dissertation is nearly completed, I would like to express my deep gratitude to all the professors, staff, and friends who have accompanied and helped me over the past two and a half years.

First of all, I'd like to express my sincere gratitude to my supervisor, Pro. Matsuyama, for his academic guidance and assistance. His responsible attitude and rigorous scholarly style have always influenced me. Pro. Matsuyama provides us with excellent research conditions, which have given us a high degree of freedom in experiments, allowing us to fully explore various interests and gain a lot. I also owe a special debt of gratitude to Takagi sensei for his valuable guidance in every group meeting. With his professional and academic knowledge, he taught me how to do research. Additionally, I would like to thank Asst. Prof. Kecheng Guan for his guidance in experimental design, experimental operations, and paper writing. He taught me so much during the more than two years we have worked together.

Secondly, I would like to thanks to Prof. Mori, and Prof. Ogino for their reviews of this dissertation, and express my gratitude to Kamio sensei, Nakagawa sensei, Kumagai sensei, Ms. Miyake, Ms. Kamio, and Ms. Ono in Membrane Engineering Group; the smooth development of scientific research is closely related to their kind support and help. In addition, may all your dreams and plans turn to fulfillment and success.

Last but not least, I am deeply grateful to my family for their support and nurturing over the years; you are my solid backing on my academic journey. I also want to thank my girlfriend, Wanyue Liu. Meeting you is my greatest fortune. In short, I have spent two wonderful years here, and I am grateful to everyone I have met during this time.

FANG SHANG

Kobe University, Japan

July 2, 2024

Table of contents

Chapter 1

General introduction

1.1 Research background

With the rapid development of the new energy industry and the increasing popularity of mobile electronic devices, there has been a sharp and unprecedented growth in the demand for lithium resources (**Fig. 1.1a**). This growth can be attributed to several factors, including the widespread adoption of electric vehicles (EVs) and the growing reliance on rechargeable lithium-ion batteries in various applications such as smartphones, laptops, and energy storage systems (**Fig. 1.1b**). In light of these developments, ensuring the sustainable supply of lithium resources has become an urgent issue. Efforts are underway to explore new lithium deposits, improve extraction technologies, and promote recycling initiatives to address this challenge and support the continued growth of the new energy industry and the market for mobile electronic devices.

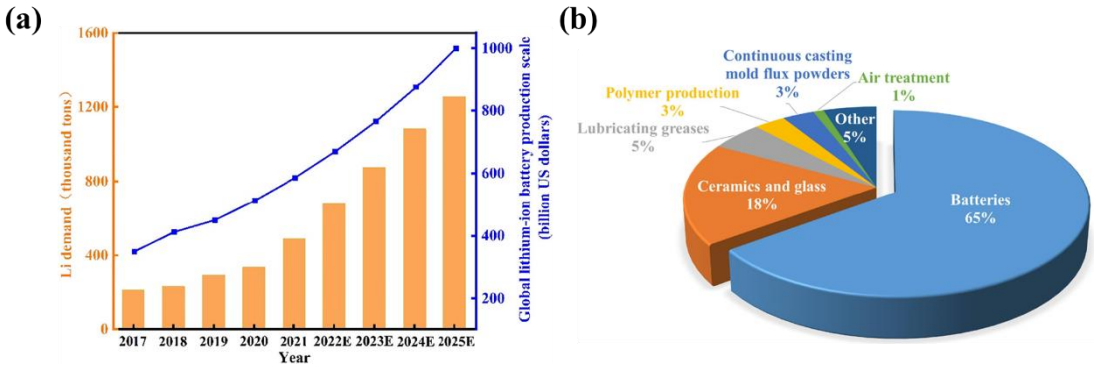

Fig. 1.1 (a) Global lithium resource demand and lithium-ion battery industry scale from 2017 to 2025; (b) Distribution of global end-use markets of lithium [1, 2].

Lithium resources primarily exist in two forms in nature: solid lithium-containing materials and liquid lithium-containing solutions. Solid lithium resources mainly include lithium clay, zeolite, and ores, while liquid lithium resources mainly comprise seawater, geothermal brine, oilfield brine, and salt-lake brines (**Fig. 1.2**). These liquid sources typically contain dissolved lithium ions and require specialized extraction techniques for efficient recovery. Understanding the diversity of solid and liquid lithium resources is crucial for developing sustainable extraction methods and ensuring a stable supply chain to meet the growing demands across various industries.

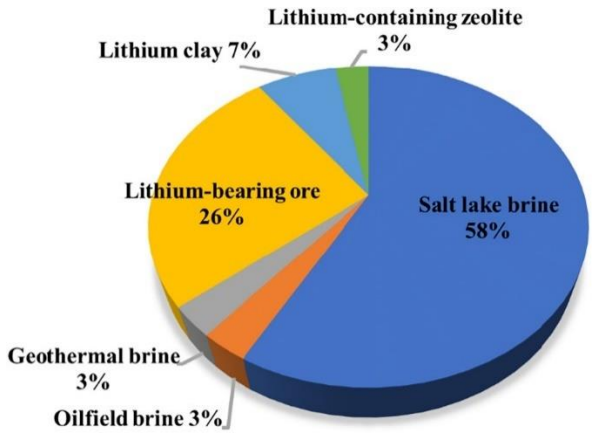

Fig. 1.2 Distribution of continental lithium resources [1].

Salt-lake brines (**Fig. 1.2**) account for approximately 58% of the world's total lithium resources (evaluated by the United States Geological Survey [3]). Additionally, compared to extracting lithium from water, extracting lithium from ores is expensive and energy-intensive. Therefore, extracting lithium resources from lithium-containing water, especially salt-lake brine, is of paramount significance. This not only helps reduce extraction costs and energy consumption but also facilitates the sustainable utilization of lithium resources.

1.2 Mg^{2+}/Li^{+} separation techniques

The salt-lake brine contains a higher concentration of Li^{+}, ranging from hundreds to thousands of parts per million (ppm) [4]. However, the problem is that it contains many coexisting cations in high concentration. This situation makes very difficult to

separate Li^+ from other coexisting cations, especially from Mg^{2+} since ionic size of Mg^{2+} is very similar to that of Li^+, and Mg^{2+}/Li^+ ratio is very high. To date, various technologies have been developed for extracting lithium from salt-lake brines, including precipitation [5, 6], adsorption, solvent extraction [7, 8], electrodialysis [9], nanofiltration [10], and others. These methods involve different processes and mechanisms aimed at separating lithium ions from the brine solution, each with its own unique advantages and limitations. The selection of the most suitable extraction technology depends on factors such as the concentration of lithium in the brine, the presence of other impurities, energy requirements, environmental considerations, and economic viability.

1.2.1 Precipitation

The fundamental principle of the chemical precipitation method lies in sequentially removing various coexisting ions and recovering lithium salts by adding chemical precipitants into evaporated concentrated brine, thereby achieving selective separation of lithium [11, 12]. The precipitants mainly consist of two major categories: carbonate precipitants [13, 14] and aluminate precipitants [15, 16]. Currently, the most widely used precipitant in industry is aluminate precipitant, and its reaction equation is as follows:

$$LiCl + 2AlCl_3 \cdot H_2O + 6NaOH = LiCl \cdot 2Al(OH)_3 \cdot xH_2O \downarrow + 6NaCl$$

Initially, $AlCl_3 \cdot H_2O$ is introduced into the brine, leading to the formation of $LiCl \cdot 2Al(OH)_3 \cdot xH_2O$ precipitate through its reaction with Li^+ under alkaline conditions. Subsequently, the precipitate is subjected to calcination and leaching, resulting in the precipitation of insoluble Al_2O_3 and obtaining a solution of LiCl [16]. Finally, the addition of Na_2CO_3 results in the precipitation of Li_2CO_3. However, this process is relatively complex, time-consuming, costly, and demonstrates lower economic efficiency, making it unsuitable for separating brines with a high Mg^{2+}/Li^+ mass ratio [1, 17].

1.2.2 Adsorption method

The adsorption method for Mg^{2+}/Li^{+} separation relies on an adsorbent with high selectivity for lithium ions, facilitating the adsorption of lithium from a solution containing magnesium, and thereby achieving lithium-magnesium separation [18]. Due to the advantages of being environmentally friendly, simple operation, high selectivity, and reversibility, the adsorption method has been proved to be an efficient separation strategy [19]. Adsorbents can be broadly categorized into two types: inorganic adsorbent materials (such as aluminum-based adsorbents, natural minerals, and lithium-ion sieves) and organic adsorbent materials (including crown ethers, calixarenes, and phosphoric esters). However, inorganic adsorbent materials often exist in powdered form, and sometimes may dissolve in solution during the adsorption-desorption process. Meanwhile, the preparation conditions for organic adsorbent materials tend to be excessively stringent.

1.2.3 Solvent extraction

The solvent extraction method exploits the difference in solubility of Li^{+} in various solvents to facilitate its transfer from the feed solution (salt-lake brine) to an organic solution, thereby enabling lithium recovery. The crucial aspect involves the selection of appropriate extractants. Commonly used extractants include crown ether extractants [20-22], diketone extractants [23, 24], organophosphorus extractants [25, 26], and ionic liquid extractants [7, 27]. **Fig. 1.3** illustrates the extraction and reverse extraction mechanism of the TBP (tributyl phosphate)/$FeCl_3$/P507 (2-ethylhexyl phosphonic acid mono 2-ethylhexyl) system, wherein TBP (as the extractant) and $FeCl_3$ coordinate with Li^{+} to form $Li{\cdot}2TBP{\cdot}FeCl_4$, with P507 remaining uninvolved in coordination. Notably, this system utilizes only water in the stripping process, avoiding the use of concentrated hydrochloric acid [8]. Nonetheless, the solvent extraction method is associated with high costs and may cause equipment corrosion, thereby limiting its industrial applicability.

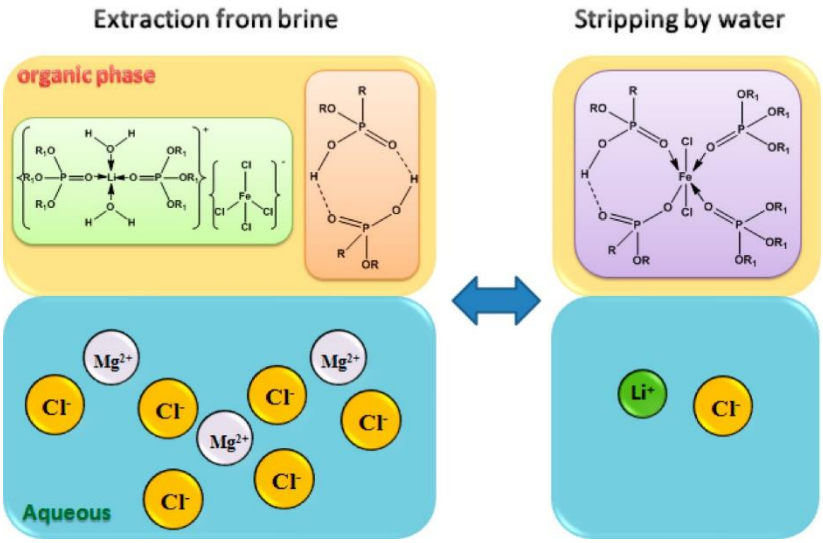

Fig. 1.3 Mechanism of lithium extraction and stripping by the TBP/$FeCl_3$/P507 system [8].

1.2.4 Membrane separation technique

Membrane separation technology has the potential to save cost in the extraction of lithium resources [28]. For example, processes like electrodialysis and nanofiltration achieve selective ion separation through physical means without the need for large amounts of chemicals or high temperatures. This means that membrane separation technologies can reduce energy consumption, which is particularly advantageous when dealing with large volumes of lithium resources such as salt-lake brines. Therefore, the adoption of membrane separation technology for lithium extraction holds promise for energy savings and environmental friendliness, promoting the sustainable utilization of lithium resources.

1.2.4.1 Electrodialysis

Electrodialysis (ED) is a separation technique that combines an electric field with ion exchange membranes (IEM). Under the influence of an external electric field, the directional movement of ions occurs in the solution. Ion exchange membranes selectively allow counter-ions to permeate through IEM, and reject co-ions, achieving the separation and concentration of ions. In the ED stack [29], anion and cation exchange membranes are arranged alternately as shown in **Fig. 1.4**. In the separation of

Li^+ and Mg^{2+} ions, monovalent cation selective cation exchange membrane is used. Thus, monovalent lithium ions can migrate through the cation exchange membrane to the concentrated compartment, while most of divalent magnesium ions cannot migrate through the cation exchange membrane and retain in the diluted compartment, thereby achieving the separation of magnesium and lithium. Although ED has high separation efficiency, its high energy consumption, elevated costs, and challenges related to membrane fouling restrict its industrial application.

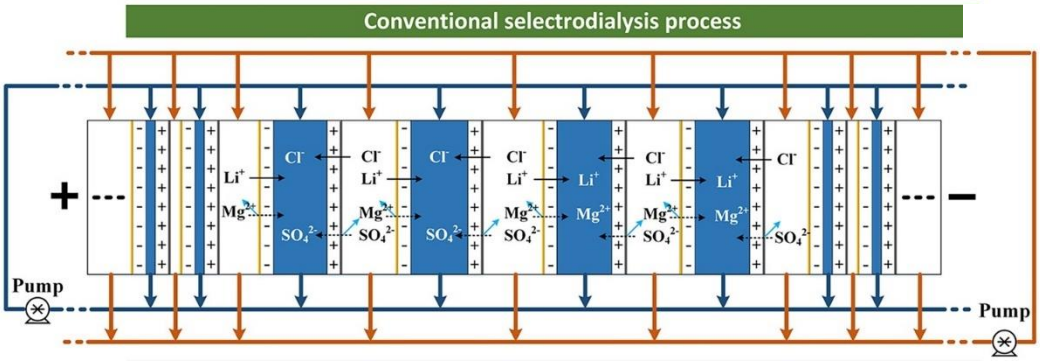

Fig. 1.4 Schematic illustration of an electrodialysis membrane stack [30].

1.2.4.2 Nanofiltration Membrane separation

Nanofiltration (NF) separation technology has attracted increasing attention due to its high selectivity and permeability. Based on the electrostatic repulsion and size exclusion, NF membranes retain multivalent ions while allowing monovalent ions to pass through, thus offering significant advantages in Mg^{2+}/Li^+ separation. Utilizing NF membranes to separate lithium-magnesium mixed solutions is efficient, simple to operate, and recyclable, making it an important research direction for lithium extraction from salt lakes. Thus, more detailed description of NF membrane is provided in the following section, Section 1.3.

1.3 Nanofiltration membrane

Membrane separation technologies can be classified into different types based on pore size (**Fig. 1.5)**. These types include microfiltration (MF), ultrafiltration (UF), nanofiltration (NF), and reverse osmosis (RO) membranes [31, 32]. MF membranes

have relatively large pores and are typically used for removing suspended solids and large particles [33]. UF membranes have smaller pores and can be used to remove colloids, bacteria, and large molecules. RO membranes have the smallest pores and can effectively retain ions, dissolved salts, and organic solutes, making them suitable for efficient desalination and concentration processes. The pore size of NF membrane is between that of UF and RO.

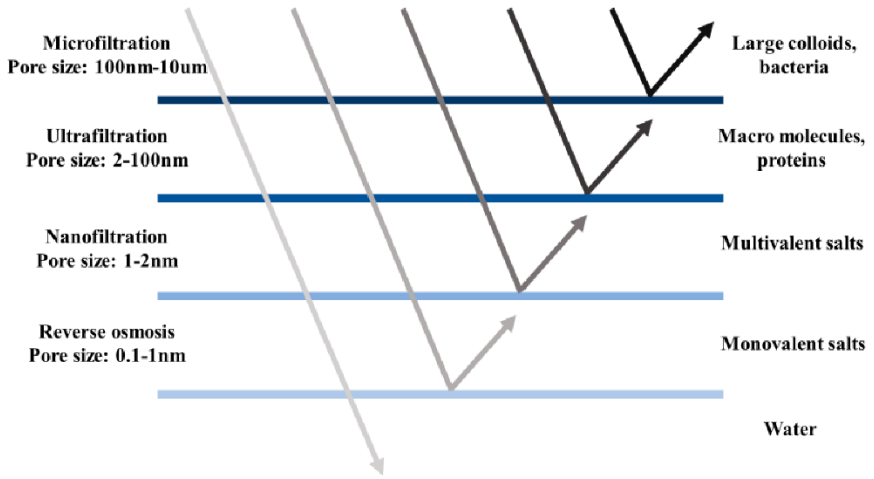

Fig. 1.5 Classification of membrane processes based on the pore size [nm] and retained solute [32].

NF research commenced in the mid-1970s and transitioned into commercialization by the mid-1980s. Positioned between reverse osmosis and ultrafiltration along the filtration spectrum (**Fig. 1.6)**, it was initially labeled as loosely-structured RO membranes in early investigations (molecular weight cut-off ranging from 200 to 1000 Da). Subsequently, owing to the membrane's pore size falling within the nanometer range, it earned the designation of nanofiltration membrane. Nanofiltration membranes excel in the separation of high-valence ions and organic compounds with molecular weights in the hundreds. Presently, they find extensive applications in diverse fields, including the pharmaceutical, food industries, and water softening.

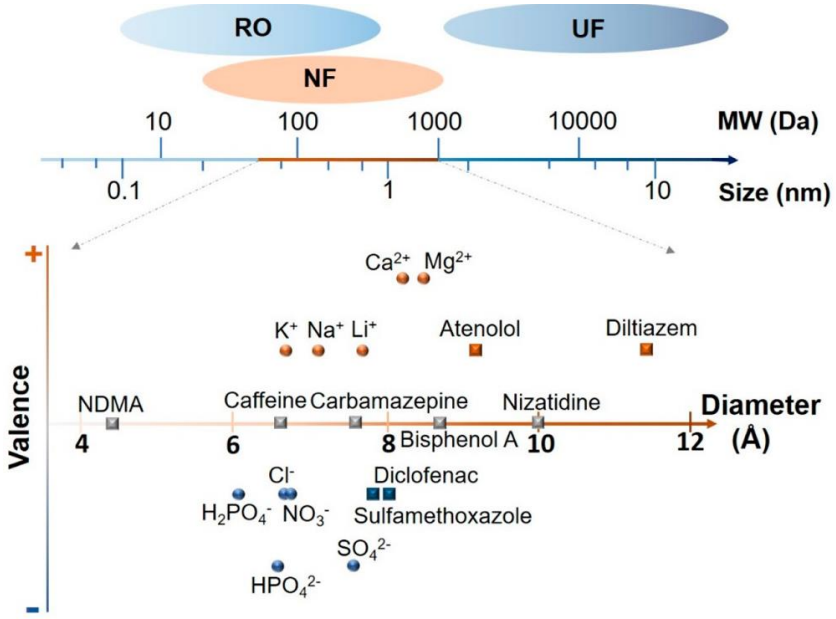

Fig. 1.6 Effective pore sizes of membranes for different applications and typical sizes of solutes [34].

1.3.1 Categories

Based on the membrane structure, the NF membrane can be divided into integrally skinned asymmetric (ISA) and thin-film composite (TFC) membranes [31, 35, 36], as shown in **Fig. 1.7a-b**.

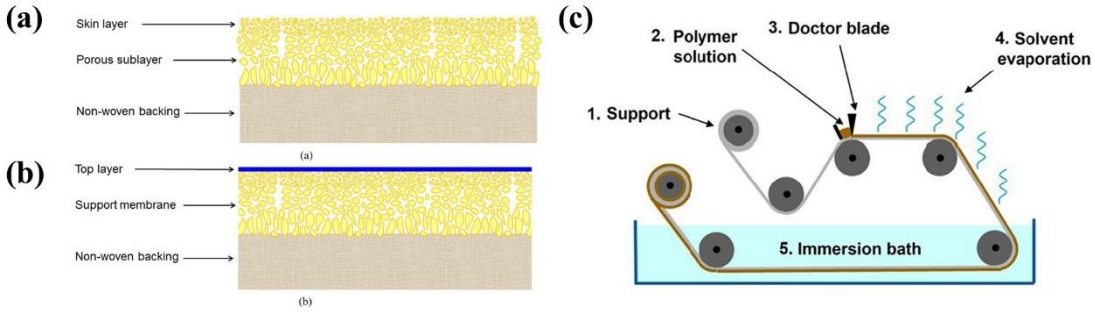

Fig. 1.7 Schematic illustration of (a) integrally skinned asymmetric (ISA) membrane; (b) thin film composite (TFC) membrane (bottom) [31]; and (c) a continuous phase inversion process for fabricating ISA membranes [35].

1.3.1.1 Integrally skinned asymmetric (ISA) NF membrane

ISA NF membranes are typically prepared using a one-step phase inversion method (**Fig. 1.7c**). In 1962, Loeb and Sourirajan successfully fabricated ISA

membranes using this approach [37]. Phase inversion involves immersing a thermodynamically stable polymer solution into a nonsolvent bath, inducing phase separation to form a polymer-rich phase and a polymer-lean phase, thus completing the transition from liquid phase to solid phase. The polymer-rich phase forms the membrane matrix, while the polymer-lean phase forms a porous support layer. The properties of the membrane are influenced by various factors [35], including the type of polymer, composition of the casting solution (including solvents, polymer concentration, additives, volatile solvents, nonsolvent additives, and pore-forming agents), evaporation time and temperature, coagulation bath, and post-treatment (such as grafting and crosslinking). The advantages of the phase inversion method for preparing separation membranes lie in its simplicity, scalability, and versatility. In addition, various polymer materials can be utilized to prepare ISA membranes (such as polysulfone (PSF) [38], polyaniline (PANI) [39], polyetheretherketone (PEEK) [40], polyimide (PI) [41], polyvinylidene difluoride (PVDF) [42], polybenzimidazole (PBI) [43], etc.), providing flexibility in membrane design and enabling customization of membrane properties to suit specific separation tasks.

1.3.1.2 Thin film composite (TFC) membrane

TFC nanofiltration membranes consist of a porous substrate and a thin active layer. Common preparation methods include layer-by-layer (LbL) self-assembly [44], two-dimensional material deposition [45], and interfacial polymerization (IP) [46]. Layer-by-layer self-assembly involves the alternate deposition of multiple molecular layers to construct the membrane structure, while two-dimensional material deposition utilizes materials such as graphene or graphene oxide to form a thin film layer, and interfacial polymerization involves the polymerization of two different monomers at the interface to generate the active layer. These methods have their characteristics, and the most suitable preparation method can be selected according to the desired membrane performance and application requirements.

(1) Layer-by-layer assembly

LbL assembly technology, a widely used technique in membrane fabrication and surface modification, involves the sequential deposition of polyelectrolytes or other materials with opposite charges onto a substrate to create nano-scale thin films (**Fig. 1.8**) [47-49]. The main interactions encompass the hydrogen bonds, covalent bonds, van der Waals forces, electrostatic interactions, etc. These interactions govern the assembly process, influencing the membrane's morphology, thickness, and properties [50]. Thus, choosing the appropriate polyelectrolytes is crucial for modulating the structure and properties of LbL membranes. The typical cationic polyelectrolytes include poly (diallyl dimethyl ammonium chloride) (PDADMAC), poly (ethyleneimine) (PEI), and poly (allylamine hydrochloride) (PAH), while anionic polyelectrolytes include poly (vinyl sulfate) (PVS), polyacrylic acid, and poly (sodium 4-styrene sulfonate) (PSS). In addition, the thickness, composition, and structure of the film can be precisely controlled by adjusting assembly conditions, such as deposition cycle and time [51].

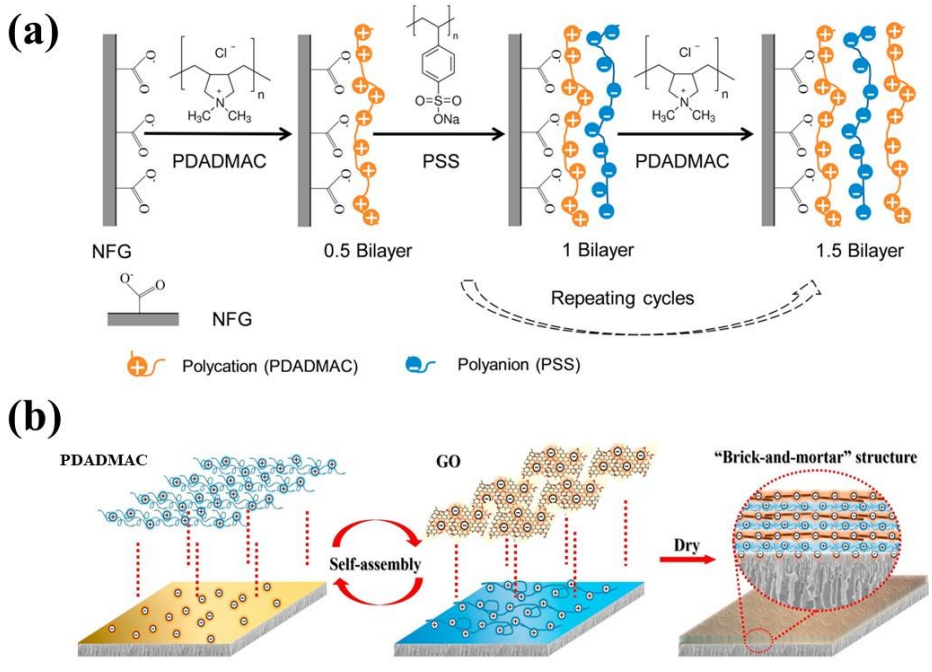

Fig. 1.8 Schematic illustration of the fabrication of (a) PDADMAC/PSS and (b) PDADMAC /GO multilayer membranes via LbL self-assembly [48, 49].

(2) Two-dimensional material deposition

Since the discovery of two-dimensional materials (including graphene oxides (GOs) [52], MXenes [53], metal-organic frameworks (MOFs) [54], covalent organic frameworks (COFs) [55], 2D zeolites [56], layered metal dichalcogenides (LMDCs) [57], etc.), two-dimensional membranes have exhibited significant potential in applications such as gas separation, water purification, and molecular sieving due to their outstanding performance. GO is one of the most extensively studied and promising two-dimensional layered membrane materials to date. The GO membrane forms a layered structure by stacking nanosheets, providing different pathways for molecule passage, including pore defects, inter-edge pores, and interlayer spacing (**Fig. 1.9a**) [58, 59]. However, the presence of a large number of hydrophilic groups can cause membrane swelling and an increase in interlayer spacing under other wet conditions, severely affecting separation efficiency (**Fig. 1.9b**). Utilizing methods such as cross-linking, reduction, and doping with supporting materials can regulate the interlayer spacing between GO nanosheets [58], achieving precise filtration of organic substances and ions (**Fig. 1.9c**).

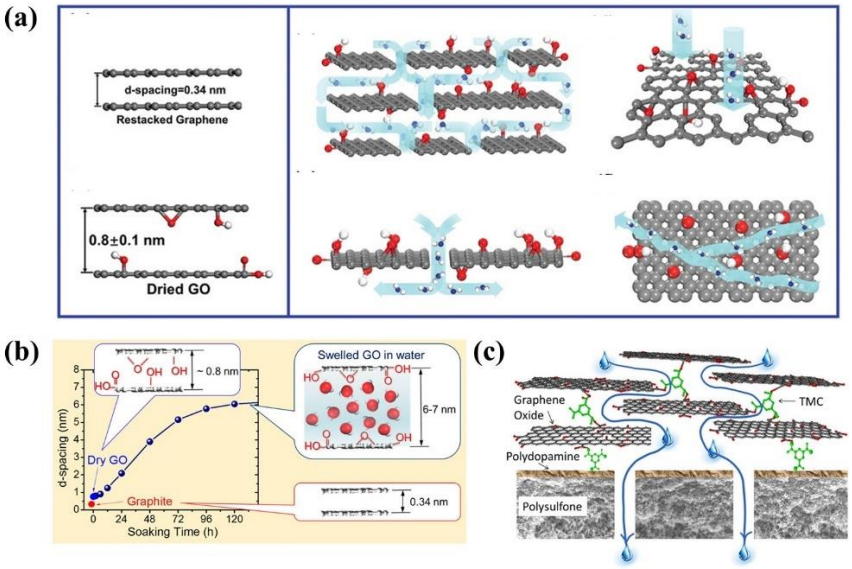

Fig. 1.9 (a) The transport pathways of GO membrane (including pore defects, inter edge pores, and interlayer spacing) [59]; (b) d-Spacing of GO membrane varies over time in water [60]; (c) chemical cross-linking of a GO membrane with trimesoyl chloride (TMC) [45].

(3) Interfacial polymerization

Due to the high permeance and salt rejection, polyamide (PA) film has been the most widely used selective layer for NF membrane. The PA selective layer is fabricated on the UF substrate through the interfacial polymerization (IP) method [31]. The UF substrate was impregnated with an aqueous phase (containing diamine monomers, such as piperazine (PIP), and m-Phenylenediamine m-Phenylenediamine (MPD)). Then, after removing the excess water, the organic phase (containing trimesoyl chloride (TMC)) was applied onto the substrate. The IP reaction quickly occurred at the interface of the two immiscible phases. The diamine monomers diffuse from the aqueous phase to the organic phase and react with TMC [35] as shown in **Fig. 1.10**. The initially formed dense PA layer will suppress further monomer diffusion, thus IP is a self-inhibitory process that can generate thin active layers with thicknesses ranging from tens to hundreds of nanometers [34]. Meanwhile, the properties of the PA active layer can be adjusted by tuning monomer types and improving operating conditions, making IP an easily operable method for preparing nanofiltration membranes. Hereafter, this type of TCF NF membrane is referred to as TFC-PA NF membrane.

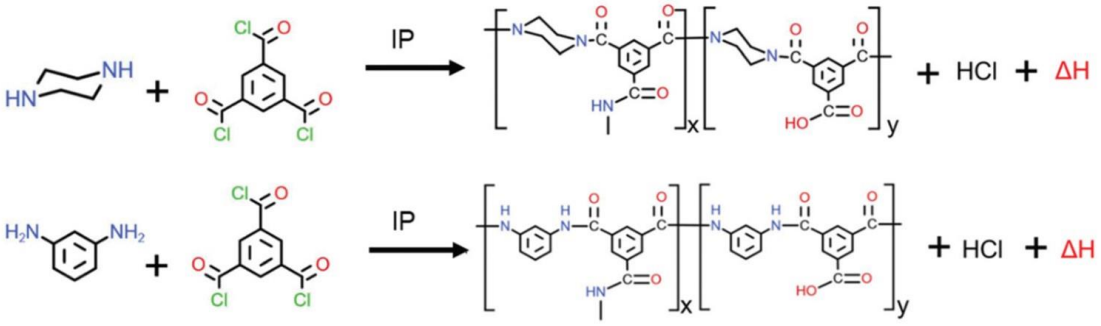

Fig. 1.10 Reactions between diamine monomers (PIP and MPD) and TMC (ΔH represents the change in enthalpy in IP reaction system) [61].

Most of traditional commercial TFC NF membranes are fabricated by the IP method. These days, TFC-PA NF membrane is very common and widely applied to many industries. In this dissertation, TFC-PA NF membrane is treated. Section 1.3.3 of

this chapter gives a detailed description of TFC-PA NF membrane.

1.3.2 *Separation mechanism*

The separation mechanism of the NF membrane is complex, mainly involving size sieving, Donnan effect, and dielectric exclusion (**Fig. 1.11**) [62, 63]. Due to the synergistic and competitive interactions of these mechanisms, it is challenging to demonstrate their respective contribution to ion selectivity [62].

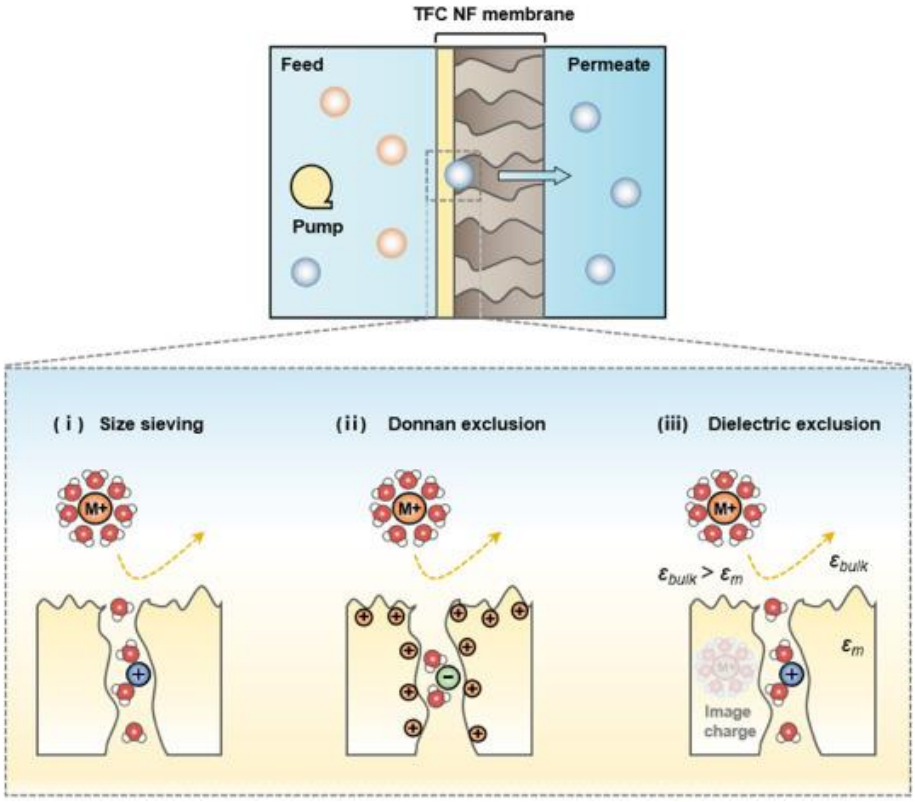

Fig. 1.11 Separation mechanism of TFC NF membrane: (i) size sieving, (ii) Donnan exclusion, and (iii) dielectric exclusion [62].

1.3.2.1 Size sieving

The size sieving effect means that when the solute is smaller than the pore size of the membrane, it can easily pass through, whereas larger solutes are effectively rejected, to achieve the solute separation (**Fig. 1.11**). Due to the presence of the solvation shells of ions in water, the difference between the hydrated radius of ions and membrane pore size plays a major role in the ion-separation process [64, 65]. **Table 1.1** shows the

characteristics of the common ions that existed in salt-lake brines. The hydrated Radius of Mg^{2+} and Li^{+} are 4.23 and 3.82 Å, respectively. When the hydrated ions pass through the smaller membrane pores, the solvation shells will be rearranged or removed (dehydration) [66, 67]. The hydrated/dehydrated ability of ions is related to their valence. Generally, both the hydration radius and dehydration energy barrier of high-valent ions are higher than that of low-valent ions [64, 65]. As shown in **Fig. 1.12**, the Li^{+} ions dehydrate more readily than Mg^{2+} ions under a pressure-driven separation process [68-70]. Therefore, based on the hydrated radius difference of different ions, selecting the NF membrane with suitable pore size distribution can achieve the precise separation of monovalent/multivalent (Mg^{2+}/Li^{+}) ions.

Table 1.1 Ion radius of the co-existing ions in salt-lake brine [71].

	Ion Radius (Å)	Stokes Radius (Å)	Hydrated Radius (Å)	Hydration energy (kcal mol^{-1})
Mg^{2+}	0.65	3.47	4.23	-437.4
Ca^{2+}	0.99	3.10	4.12	-359.7
Li^{+}	0.60	2.38	3.82	-113.5
Na^{+}	0.95	1.84	3.58	-87.2
K^{+}	1.33	1.25	3.31	-70.5
Cl^{-}	1.81	1.20	3.32	-91
SO_4^{2-}	2.90	2.30	3.82	-258.1

In addition to the physical pore size sieving effect, the interactions between the solutes and membrane also influence the separation performance of NF membrane, involving the electrostatic interaction, dielectric interaction, affinity, hydrophilic or hydrophobic interaction, etc. [62, 72].

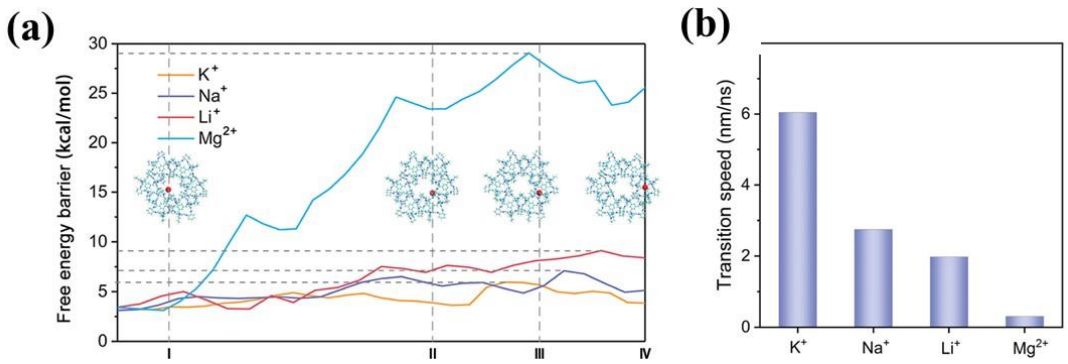

Fig. 1.12 (a) Free energy barriers of ions (K^+, Na^+, Li^+, and Mg^{2+}) transported in covalent cage 3 channels (a porous organic cage material) at four representative positions (I, II, III and IV) and (b) transition speeds of ions (K^+, Na^+, Li^+, and Mg^{2+}) in covalent cage 3 channels [70].

1.3.2.2 Donnan exclusion

Donnan exclusion is a classical theory to interpret the electrostatic interaction between the charged solutes and membrane (**Fig. 1.11**), which was proposed by Donnan in 1911 [73]. Under neutral pH conditions, the NF membranes usually carry charges (negative or positive charge) due to different chemical groups on the membrane surface (such as $–COO^-$, $–SO_3^-$, and $–NH_4^+$), which results in strong electrostatic interactions between the membrane and ions. When the ions and membranes carry opposite charge, many ions are partitioned into the membrane to keep the electroneutral condition within the membrane [74, 75]. When the ions and membranes carry the same charges, the rejection for these ions usually increases due to the strong electrostatic repulsion, especially for the multivalent ions [76-78]. Therefore, adjusting the membrane charge can enhance the selectivity for specially charged ions, such as reversing the membrane charge from negative to positive is beneficial for Mg^{2+}/ Li^+ separation [75].

1.3.2.3 Dielectric exclusion

The dielectric exclusion interprets the repulsion behavior of polarization charges (caused by the dielectric constant difference between the membrane and aqueous solution) on the NF membrane surface to the charged ions (**Fig. 1.11**). The dielectric

constant of the common polymeric membrane (ε_m) is usually less than 10, while that of the aqueous solution (ε_{bulk}) is about 80 [62, 79]. In addition, when the water molecules enter the nanoscale pore of the NF membrane, the conformation of the water clusters has changed, thus leading to the decrease of the aqueous solution dielectric constant in pores [79]. The polarization behavior of charged groups on the membrane surface finally influences the ion transfer behavior during the membrane separation process. Notably, the dielectric exclusion strength is only related to the ion valence rather than its sign (proportional to the square of ionic charge), and it means that both positively and negatively charged ions can be blocked by the dielectric exclusion [80]. Therefore, the dielectric exclusion behavior serves as an additional separation mechanism for the NF membrane, and the synergistic effect of dielectric and Donnan exclusion contributes to the ion separation, which was proved by Wen et al [81]. In addition, they found that the Donnan exclusion plays the most important role in the Mg^{2+}/ Li^{+} separation process for the positively charged NF membrane.

1.3.3 TFC-PA NF membrane for Mg^{2+}/Li^{+} separation

TCF NF membrane process is one of the pressure-driven membrane processes, and commonly operated under the cross-flow filtration system (Fig. 1.13), The driving force is an applied pressure to feed solution.

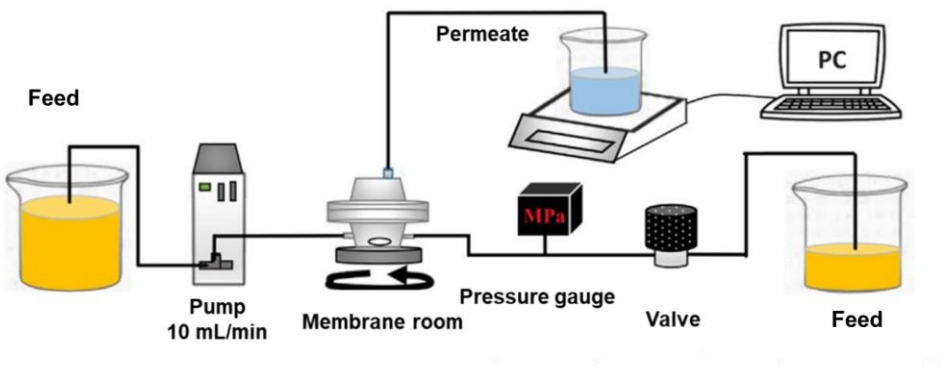

Fig. 1.13 Schematic illustration of cross-flow filtration set-up.

NF separation technology has attracted increasing attention due to its high ion selectivity. Especially, TFC NF membrane with PA selective layer fabricated by IP

process (TFC-PA NF membrane) is widely applied in ion separation. Based on the synergistic effect of size sieving, Donnan effect, and dielectric exclusion, TFC-PA NF membranes can retain multivalent ions while allowing monovalent ions to pass through, thus offering significant advantages in Mg^{2+}/Li^{+} separation [82]. Utilizing TFC-PA NF membranes to separate Mg^{2+}/Li^{+} mixed solutions is efficient, simple to operate, and recyclable, making it an important research direction for lithium extraction from salt lakes. These membranes can be divided into three kinds: (1) Negatively charged NF membrane, (2) Positively charged NF membrane, and (3) Mix-charged NF membrane.

1.3.3.1 Negatively charged NF membrane

In general, the traditional commercial TFC NF membranes (including Desal (DL), DK, NF90, NF270, etc.) are fabricated by the IP method. Then, these membranes usually display a negative charge, due to the existence of carboxyl group (derived from unreacted acyl chloride hydrolysis during IP process). Up to now, these membranes have been attempted to be applied in Mg^{2+}/Li^{+} separation (**Table 1.2**). The Desal DL-5 membrane was first used to extract LiCl from diluted brine, and the corresponding separation factor ($S_{Mg^{2+}/Li^{+}}$) could reach 3.5 [81]. The corresponding $S_{Mg^{2+}/Li^{+}}$ was defined by the following equation:

$$S_{Mg^{2+}/Li^{+}} = \frac{C_F(Mg)/C_F(Li)}{C_P(Mg)/C_p(Li)} \quad (1.1)$$

where C_F (Mg) and C_F (Li) and C_P (Mg) and C_P (Li) represent the concentrations of Mg^{2+} and Li^{+} in the feed and permeate solutions, respectively.

The Desal DL-2540 had a similar $S_{Mg^{2+}/Li^{+}}$ of 3.3 for the Mg^{2+}/Li^{+} mass ratio of 64 [83]. Various operating conditions were investigated, such as pH, operating pressure, Mg^{2+}/Li^{+} mass ratio, and water temperature. The results indicated that all of these factors have a great influence on DL-2540 membrane separation performance. Briefly, lower pH value and higher operating pressure are beneficial to the Mg^{2+} rejection, while higher Mg^{2+}/Li^{+} mass ratio having a negative effect on the Mg^{2+} rejection. The Desal DK membrane also was chosen to investigate the possibility of recovering Li^{+} from the Mg^{2+}/Li^{+} mixture with the Mg^{2+}/Li^{+} mass ratio of 24, and the $S_{Mg^{2+}/Li^{+}}$ reach 3.22, which

could not be affected by the Mg^{2+}/Li^{+} mass ratio and Li^{+} concentration [84].

Table 1.2 Separation performance of various commercial NF membranes.

Membrane	Mg^{2+}/Li^{+} ratio	$R_{Mg^{2+}}$ (%)	$R_{Li^{+}}$ (%)	$S_{Mg^{2+}/Li^{+}}$	Ref.
Desal DL-5*				3.5	[81]
Desal DL-2540*	64	~60	< -10	3.3	[83]
Desal DK*	24			3.22	[84]
NF270**	10	91	56	4.8	[85]
NF90**	10	99	77	52.6	[85]

$R_{Mg^{2+}}$, $R_{Li^{+}}$: rejection of Mg^{2+} and Li^{+} ion, respectively; $S_{Mg^{2+}/Li^{+}}$: separation factor; *: Suez Environnement, **: Dow Chemical Company.

Additionally, a NF90 membrane was utilized for the separation of lithium from ten-times diluted Chotte Djerid brine (Mg^{2+}/Li^{+} mass ratio 56.76) [86]. Under low operating pressure (<15 bar), the Mg^{2+} rejection was about 100% while Li^{+} rejection was only 15 %, demonstrating a great Mg^{2+}/Li^{+} separation performance. However, after filtration (6 h), the permeance decreased to 0.7 L m^{-2} h^{-1} bar^{-1} with nearly 50% loss compared with the initial permeance, which was caused by the membrane fouling. The negatively charged commercial NF membranes could adsorb these positively charged ions (like Mg^{2+} and Ca^{2+}) due to the strong electrostatic interaction, causing scaling on the membrane surface. In addition, the electrostatic interaction could promote the permeate of Mg^{2+} through the negatively charged commercial NF membrane, leading to a decrease in Mg^{2+} rejection[87, 88].

1.3.3.2 Positively charged NF membrane

Compared to monovalent ions (Li^{+}), positive membranes usually show a stronger exclusion effect on divalent ions (Ca^{2+} and Mg^{2+}) due to the stronger electrostatic repulsion (Donnan exclusion effect). The positively charged NF membrane was considered as a promising choice for the cation rejection, especially for multivalent/

monovalent cation separation such as Mg^{2+}/Li^{+} separation. Therefore, various positively charged NF membranes fabricated by the IP method have been designed for lithium recovery. It is known that TFC-PA NF membranes with different properties (such as membrane charge and pore size distribution) can be fabricated by adjusting the type of reaction monomer in the IP process. Li et al. [89] first reported the positively charged selective layer on the polyacrylonitrile (PAN) ultrafiltration hollow fiber membrane for Mg^{2+}/Li^{+} separation via IP method using 1,4-Bis (3-aminopropyl) piperazine (DAPP) and TMC as the monomers in aqueous and organic phase, respectively (**Fig. 1.14a**). Results showed that the rejection of Mg^{2+} and Li^{+} are approximately 46 and -40.7 respectively, and the corresponding Mg^{2+}/Li^{+} ratio decreased from 20 (feed) to 7.7 (permeate). Some multi-amine monomers were further utilized as aqueous phase monomers to adjust the membrane performance. Xu et al. [90] fabricated the PEI/TMC-based positively charged TFC-PA NF membrane. The Mg^{2+}/Li^{+} mass ratio decreased from 20 to 1.3 with a $S_{Mg^{2+}/Li^{+}}$ of 20, and the difference in rejection of Mg^{2+} and Li^{+} was 76%. The unreacted amine groups on the PEI branch chains significantly enhance the positive charge of the polyamide layer. Subsequently, Xu et al. [91] further developed the utilization of polyallylamine (PAA) as the novel aqueous amine monomer, which has a higher density of amine groups than PEI (**Fig. 1.14b**). The fabricated PAA/TMC membrane exhibited excellent Mg^{2+}/Li^{+} separation performance with a high $S_{Mg^{2+}/Li^{+}}$ of 82.8. In addition, some fascinating IP processes were evolved (**Fig. 1.14c-d**), such as reversed interfacial polymerization (RIP) [92] and gas/liquid interfacial polymerization (GLIP) [93] methods. For the RIP method, the operation sequence of PEI and TMC monomers was reversed, and acetone was used as the solvent of PEI instead of water, preventing the premature hydrolysis of acyl chlorides and increasing the positive charge of the membrane surface. In the GLIP process, ethylenediamine (EDA) amine gas was used instead of the aqueous solution, and the IP reaction occurred at the gas/liquid interface. During the GLIP process, the excessive amine monomers led to the retention of more unreacted groups, thus the positively-charged PA NF membranes were successfully prepared. Besides the simple

IP process, various methods were used to adjust the IP process, and more specific details were elaborated in Section 1.4 of this chapter.

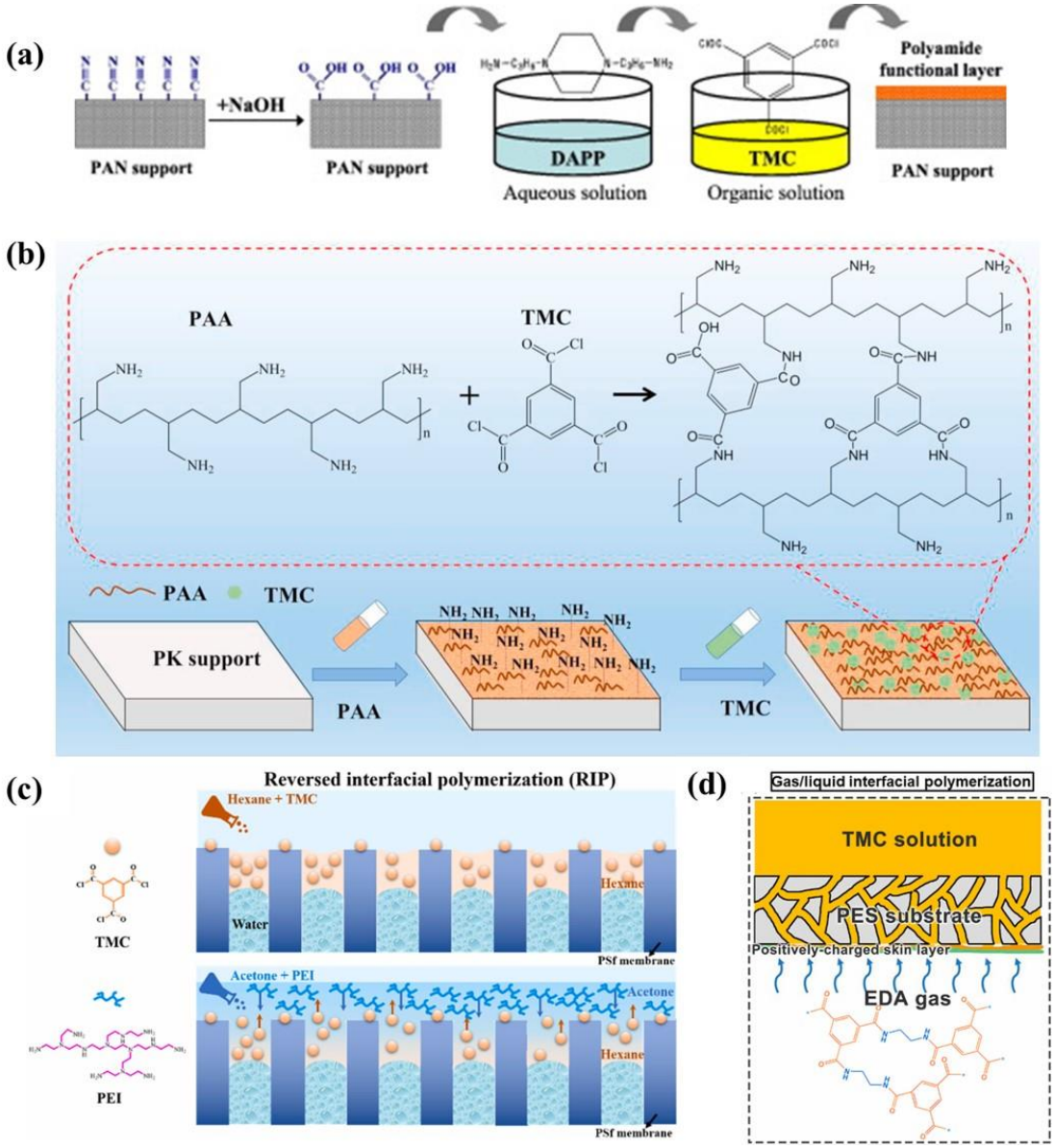

Fig. 1.14 Schematic illustration of the preparation process of (a) DAPP/TMC NF membrane [89]; (b) PAA/TMC-based NF membrane; (c) RIP: PEI/TMC NF membrane, (d) GLIP: EDA/TMC NF membrane [93].

1.3.3.3 Mix-charged NF membrane

Besides single-charged nanofiltration membranes, some mix-charged NF membranes have been designed, which exhibit excellent rejection for both monovalent and divalent ions. The mix-charged NF membrane can be divided into three types (**Fig.**

1.15) according to the spatial charge distribution, including charge-mosaic [94], dually-charged (Janus) [95-97] and polyelectrolyte complex NF membrane [98]. All of these mix-charged NF membranes were attempted for the separation of the Mg^{2+}/Li^{+} mixture.

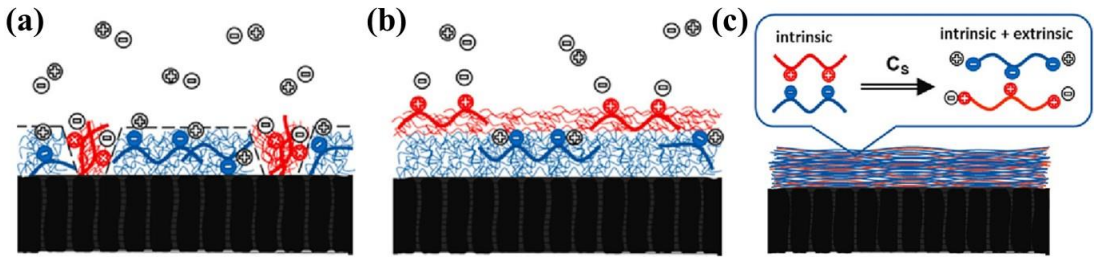

Fig. 1.15 Schematic illustration of the (a) charge-mosaic, (b) dually-charged, (c) polyelectrolyte complex NF membranes [63, 99].

Zhao et al. [78] added the positively charged amino-functionalized polyhedral oligomeric silsesquioxane (NH_2-POSS) into the PIP aqueous phase and successfully fabricated the mix-charged PA-NH_2-POSS membrane (**Fig. 1.16a**). The membrane showed high NaCl/Na_2SO_4 and LiCl/$MgCl_2$ salt selectivity (48.2 and 43.9). Lu et al. [96] developed a charge-inversion method via a secondary interfacial reaction of branched PEI (**Fig. 1.16b**). The utilization of low-molecular-weight PEI can enhance the amine grafting density. For the mixed solution with a high Mg^{2+}/Li^{+} ratio of 150, the optimized membrane showed a high $S_{Mg^{2+}/Li^{+}}$ of 12.37. He et al. [98] fabricated the PSS/PAH membrane via the LBL deposition method (**Fig. 1.16c**), and the membrane exhibited a record-high rejection of Mg^{2+} (99.9%) and $S_{Mg^{2+}/Li^{+}}$ of 430.

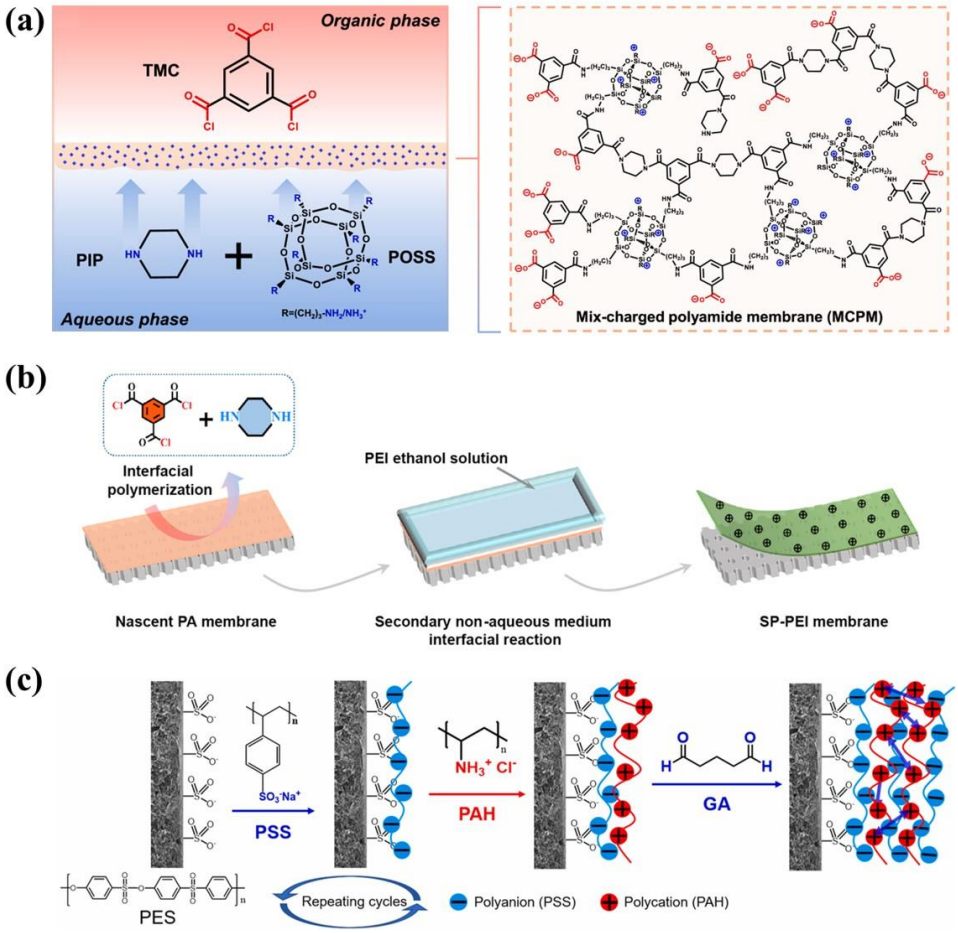

Fig. 1.16 Schematic illustration of the preparation process of (a) PA-NH_2-POSS mix-charged PA membrane [78]; (b) surface-charge inversed SP-PEI membrane [96]; (c) PSS/PAH LBL polyelectrolyte membrane [98].

1.4 Performance optimization of PEI/TMC-based NF membrane

Due to the high permeance, satisfactory Mg^{2+} rejection, and simple fabrication method, the positively charged TFC-PA NF membranes fabricated by the IP method were widely used for Mg^{2+}/Li^{+} separation, and PEI was the most commonly utilized aqueous phase multi-amine monomer in the IP process. In the typical IP process, the UF substrate was impregnated with a PEI aqueous phase, then the excess water was removed and the TMC organic phase was applied onto the substrate. The IP reaction quickly occurred at the interface of the two immiscible phases. The PEI monomers diffuse from the aqueous phase to the organic phase and react with TMC. To date, some novel strategies have been developed to optimize the PEI/TMC-based NF membranes

(**Fig. 1.17**). The substrate can be modified to regulate the kinetics of the IP reaction by constructing an interlayer or template on the substrate membrane (① and ②). Some new techniques were used to control the reaction process, such as micro-IP and LbL assembly method (③ and ④). Some additives can be incorporated into aqueous phase to regulate the diffusion rate of amine monomers to the organic phase (⑤ and ⑥). In addition, the post-treatment of the pristine membrane, such as solvent treatment and surface grafting (⑦ and ⑧), also can further improve the membrane performance.

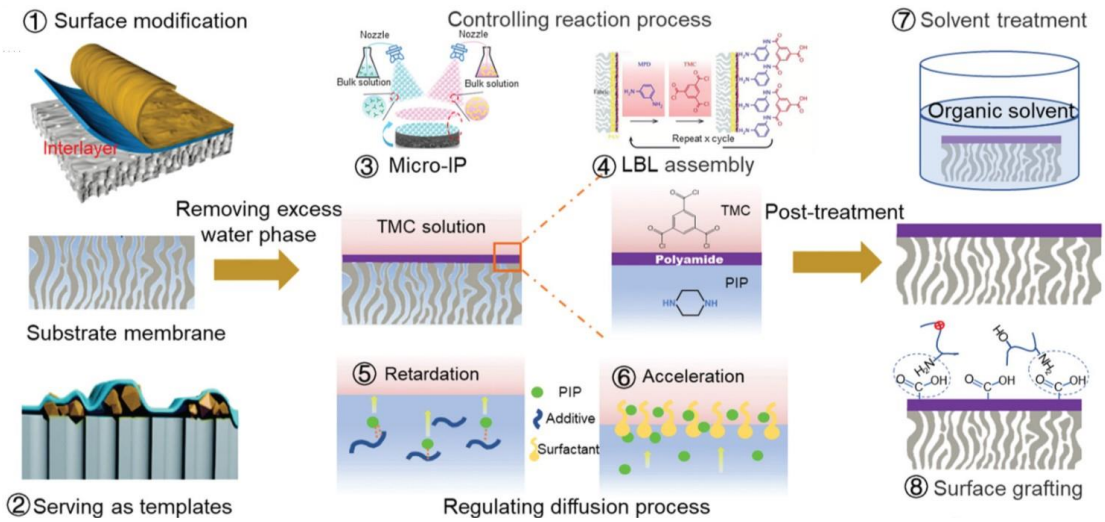

Fig. 1.17 Schematic illustrations of the novel strategies have been developed to optimize the TFC-PA NF membranes [61].

1.4.1 Modification of substrate membrane

The properties of the substrate, involving the wettability, roughness, and chemical composition, can affect the distribution of aqueous monomers on the substrate surface. The uniform distribution of aqueous monomers is beneficial to the formation of uniform and defect-free PA membranes. Interlayer construction [100, 101] and surface modification [102] are two common measures. The interlayer and surface coating can regulate the distribution and release of amine monomers through some interactions.

Jin et al. [100] fabricated a PEI/TMC PA selective layer on the Kevlar hydrogel interlayer surface on PES substrate (**Fig. 1.18a**). Due to the interaction of Kevlar hydrogel and PEI, the ultrathin PA layer was obtained, which greatly reduced the water

transport resistance, leading to twice water permeance of pristine PES-based membranes. Another carboxylated cellulose nanocrystal (CNC-COOH) interlayer was constructed on the PES substrate and a similar ultrathin PA layer was fabricated [101]. The double Janus NF membrane consisted of a negative CNC-COOH interlayer and the positive PEI/TMC PA membrane showed $S_{Mg^{2+}/Li^{+}}$ of 12.15 and 5.84 for the mixed solution with Mg^{2+}/Li^{+} ratio of 30 and 60, respectively. Wang et al. [103] constructed a PEI-Noria polyphenol interlayer and further prepared a positively charged PEI/TMC NF membrane (**Fig. 1.18b**). The PEI-Noria interlayer can regulate the storage and prevent the instruction of PEI monomers, leading to the formation of a defect-free PA membrane. In addition, the Noria can provide extra water channels, which further increases the membrane permeance (1.6 times than initial PA membrane) without sacrificing the Mg^{2+} rejection (95.4%). In summary, substrate membrane modification with introduction of various specific nanomaterials and groups provides an efficient strategy for Mg^{2+}/Li^{+} separation from salt-lake brine.

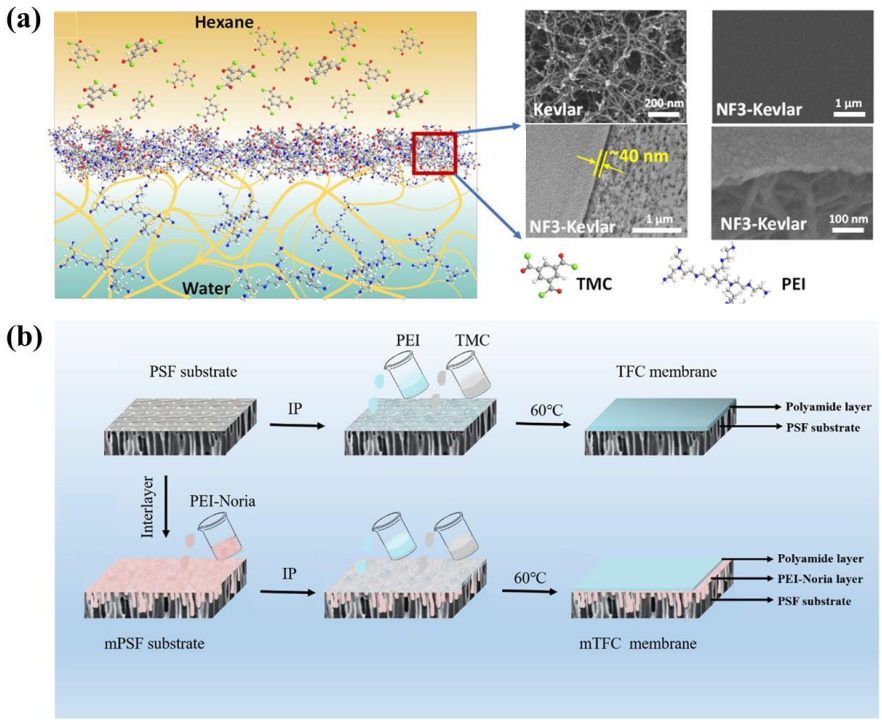

Fig. 1.18 (a) Schematic illustrations and SEM images of PEI/TMC ultrathin PA layer on the Kevlar hydrogel membrane [100]; (b) Schematic illustrations of the fabrication process of PEI-Noria interlayer mediated PEI/TMC NF membrane [103].

1.4.2 Control of IP reaction process

During IP process, besides altering monomer, various additives (such as metal-organic frameworks (MOFs) [104], silica (SiO_2) [105], carbon nanotubes (CNTs) [106, 107], graphene quantum dots (GQD) [108], and γ-cyclodextrins (γ-CDs) [109], etc.) have been added into aqueous phase to regulate the membrane properties (including surface charge density and pore size distribution). Wu et al. [105] developed a novel positively charged thin-film nanocomposite (TFN) NF membrane, via the PEI and 3-diamino-methyl-cyclohexyl triethoxysilane (DTES) mixed aqueous amine monomers reacting with TMC (**Fig. 1.19a**). The SiO_2 nanoparticles, generated due to the DTES hydrolysis, increase the porosity and hydrophilicity of the PA layer, enhancing the membrane water permeance (6.19 L m^{-2} h^{-1} bar^{-1}). Meanwhile, the DTES/PEI/TMC membrane showed a high $S_{Mg^{2+}/Li^{+}}$ of 12.95 with a higher Mg^{2+} rejection (95.2%). In addition, some particular functional materials (crown ethers) have attracted much attention. Because crown ethers can selectively form complexes with many cations, some of them tend to be complex with K^{+}, Na^{+}, and Li^{+} [110]. For example, 12-crown-4 [111], 15-crown-5 (15C5) [112], and 18-crown-6 [113] have been applied as additives in PA membranes for Mg^{2+}/Li^{+} separation (**Fig. 1.19b**). During the fabrication process, the cavities of crown ethers provide the Li^{+} transport channels and contribute to the Li^{+} recovery from salt-lake brines.

In summary, the additives in the PA membrane can provide special transport channels, thus improving the membrane permeability and selectivity. However, the gathering of nanomaterials may influence the density of the PA selective layer. Therefore, the fabricating process of additive-assisted PA membranes needs to be further optimized for efficient Mg^{2+}/Li^{+} separation.

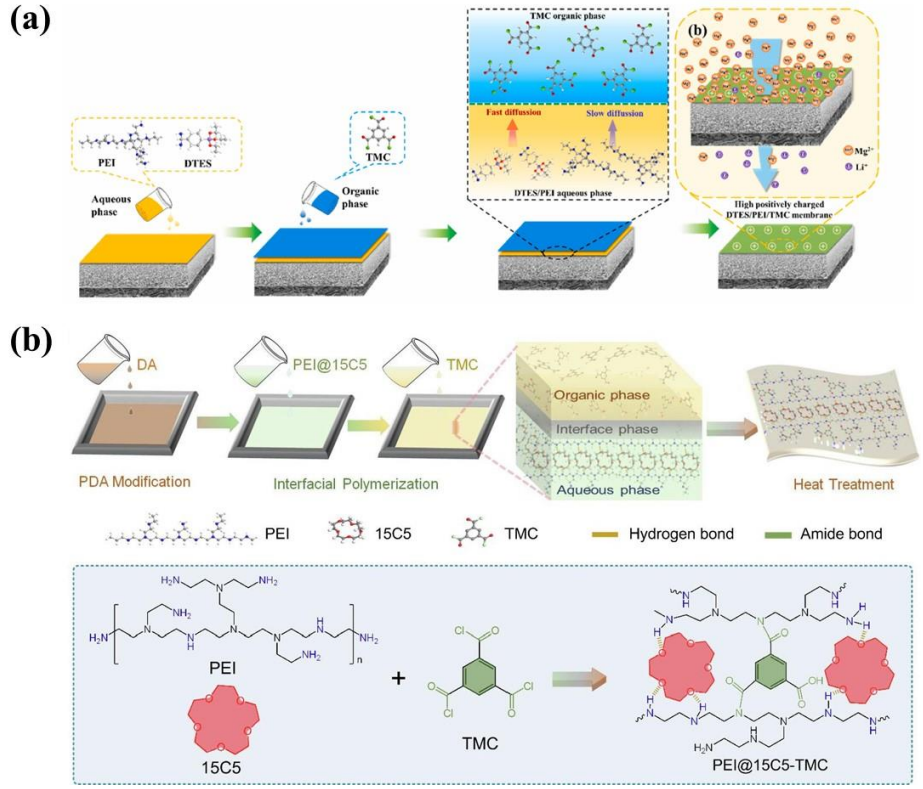

Fig. 1.19 (a) Schematic illustrations of the fabrication process of DTES/PEI/TMC TFN NF membrane [105] and (b) PEI@15C5-TMC membrane for Mg^{2+}/Li^{+} separation [112].

1.4.2 Post-treatment of PA membrane

Post-treatment method, including surface grafting and coating, can significantly adjust the membrane physicochemical properties and improve membrane separation performance [61]. Different materials with special groups can be introduced to the membrane via various physicochemical interactions. Recently, surface modification of PEI-TMC using positively charged electrolytes [114-118] has been proven to enhance their Mg^{2+}/Li^{+} separation performance. After the traditional PEI/TMC IP reaction, the membrane surface processes some residual acyl chloride groups, thus some special groups can easily graft onto the membrane surface. For instance, Xu et al. [117] successfully designed a new monomer (*bis*-quaternary ammonium N, N, N′, N′-tetrakis (2-hydroxypropyl) ethylenediamine, QEDTP) and grafted it onto the PEI/TMC membrane (**Fig. 1.20a**). The QEDTP monomer with bis-quaternary ammonium is

conducive to the increase of membrane positive charge densities, and the fabricated PEI-TMC-QEDTP membrane exhibited excellent Mg^{2+}/Li^{+} separation performance with $S_{Mg^{2+}/Li^{+}}$ of 15.6 for the high Mg^{2+}/Li^{+} ratio (120) mixture. Similarly, Liu et al. [118] designed the quaternized tetrahydroxyethyl imidazolium (QTHIM), containing four imidazoliums and hydroxyl groups for each monomer. Based on the "hydroxyl-acyl" condensation reaction, the QTHIM was successfully grafted onto the PEI/TMC membrane (**Fig. 1.20b**). PEI-TMC-QTHIM membrane displayed a looser structure and enhanced surface charge, and the corresponding water permeance increased to 6 times higher than the pristine PEI/TMC membrane without sacrificing the Mg^{2+} rejection (92.2 %).

Post-treatment of the PA membrane is a simple and efficient strategy for the improvement of the Mg^{2+}/Li^{+} separation performance of the positively charged membrane. Even though the weak stability of these membranes is a nonnegligible problem, with the gradual optimization of post- treatment method, it is expected to be an ideal strategy for lithium extraction from salt-lake brine in the future.

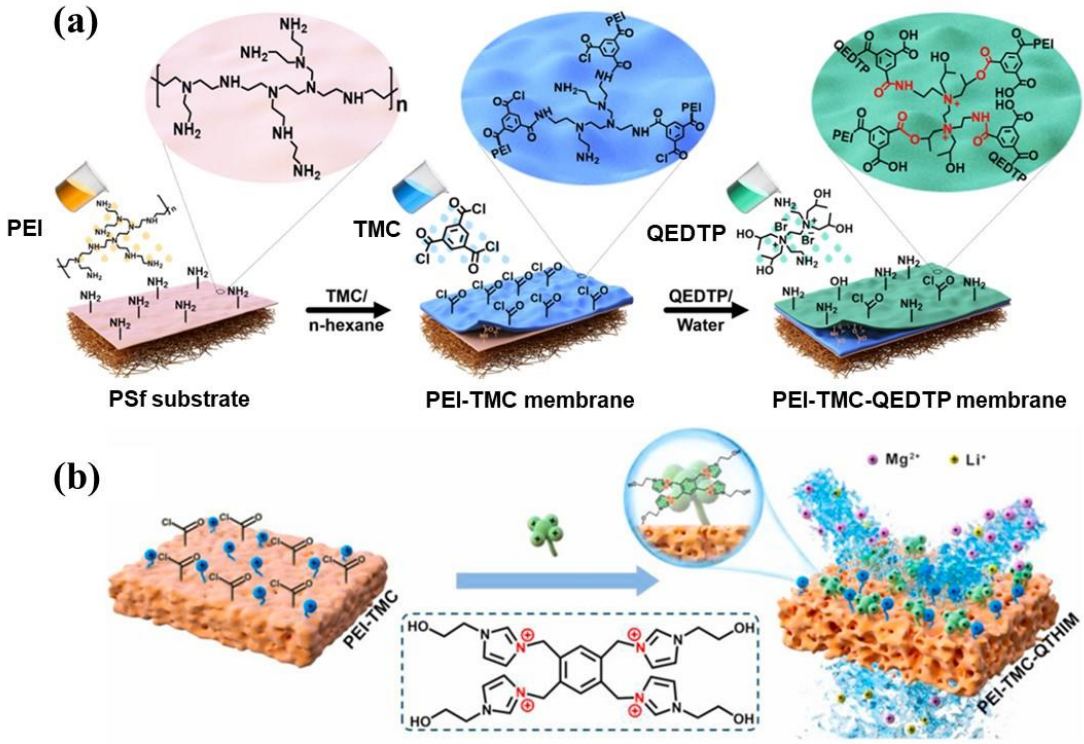

Fig. 1.20 Schematic illustrations of the fabrication process of (a) PEI-TMC-QEDTP [117] and (b) PEI-TMC-QTHIM membrane [118] via surface modification method.

1.5 Current challenges faced by NF membrane for Mg^{2+}/Li^{+} separation

The excessively high Mg^{2+}/Li^{+} mass ratio (ranging from dozens to hundreds) and similar hydrated radius (Mg^{2+}, 4.23 Å VS Li^{+}, 3.82 Å.) are the key factors that hinder the lithium recovery efficiency. Thus, the development of efficient technologies for Mg^{2+}/Li^{+} mixture separation is crucial. Based on the synergistic effect of size sieving and Donnan effect, TFC-PA NF membranes, which consists of a porous substrate and a thin polyamide PA active layer, can retain multivalent ions while allowing monovalent ions to pass through, thus offering significant advantages in Mg^{2+}/Li^{+} separation [82]. Utilizing NF membranes to separate Mg^{2+}/Li^{+} mixed solutions is efficient, simple to operate, and recyclable, making it an important research direction for lithium extraction from salt lakes. The PEI/TMC-based positively charged TFC-PA NF membrane, fabricated via the IP method at PEI aqueous and TMC organic phase interface, was considered a promising choice for Mg^{2+}/Li^{+} separation. Compared to monovalent ions (Li^{+}), positively charged membranes usually exhibit a stronger electrostatic exclusion effect on divalent ions (Mg^{2+}) carrying more charges. The protonation of unreacted –NH_2– and –NH– groups in the PEI branch endow the PEI/TMC-based membrane positive charge [77, 119]. However, due to excessive cross-linking structure, PEI/TMC-based membranes display low permeance.

Various methods have been utilized to improve the permeance and ion selectivity of NF membranes, for instance, an isotropic interlayer contributes to the uniform distribution and diffusion of amine monomers to adjust the IP kinetics and improve monovalent ion selectivity. Adding additives to the aqueous phase can also control the diffusion rate and interface concentration fluctuations of the amine monomers, thereby obtaining a polyamide layer with a uniform pore size distribution [62]. Notably, pre-enrichment of the amine monomers at the interlayer can facilitate the formation of a defect-free PA selective layer. Nevertheless, most literature uses a two-step method,

which involves intermediate layer construction and subsequent amine monomer enrichment. Therefore, appropriate optimization of experimental conditions and operation procedures are necessary to efficiently produce high-performance membranes.

In addition, many types of functional nanomaterials [62]were incorporated into the aqueous phase to fabricate the thin film nanocomposite (TFN) membrane, such as polymers (e.g., tannic acid (TA), polyvinyl alcohol (PVA), chitosan (CS), polydopamine (PDA), etc.), nanomaterials (e.g., halloysite nanotubes (HNTs), graphene oxide (GO), carbon nanotubes (CNT), metal-organic frameworks (MOFs), cellulose nanocrystals (CNC) and covalent organic frameworks (COFs)), and salt additives (such as NaCl, $NaHCO_3$, $CuCl_2$, and ionic surfactants). However, some issues need to be addressed, including the poor dispersion in aqueous solution, weak adhesion between nanomaterials and PA matrix, uncontrolled distribution, and limited loading amount in PA matrix. These challenges hampered the development of high-performance TFN membranes [120].

Notably, even though the positively charged NF membrane improves the rejection of Mg^{2+}, it also increases the retention of Li^+ at the same time, which leads to low Li^+ permeability and further reduces the Mg^{2+} and Li^+ separation efficiency.

All of these issues mentioned above urgently need to be addressed.

1.6 Purpose and overview of this dissertation

TFC membranes are the most widely used nanofiltration membranes and typically consist of a top PA active layer and a bottom porous substrate. The PEI/TMC-based positively charged polyamide NF membrane, fabricated via IP reaction at PEI aqueous and TMC organic phase interface, was considered a promising choice for Mg^{2+}/Li^+ separation. However, the trade-off between the permeability and selectivity of TFC membranes limits further improvement of the separation performance [121]. Producing PA membranes with higher water permeance without compromising their salt rejection ability is still a challenge. Based on the above-mentioned matters, some insights and

considerations were provided for optimizing the Mg^{2+}/Li^{+} separation performance of PEI/TMC-based NF membranes.

This dissertation includes 5 chapters.

Chapter 1: The research background and purpose of this research are generally introduced.

Chapter 2: In this chapter, the complexation of amine monomers with cellulose nanocrystals (CNC) and subsequent deposition on a substrate for the IP reaction was employed to modify the polymerization process and the resulting interlayered-thin film nanocomposite (i-TFN) membrane structure. This method can optimize the amine loading and distribution for the IP reaction, and CNC with favorable functional groups can limit the release and diffusion behavior of the amine monomer, resulting in a crumpled membrane structure with a retained continuous polymer network. The optimized membrane had a three-fold higher water permeance than the pristine membrane without compromising salt rejection performance. This study provides a strategy for regulating the monomer distribution and reaction at the IP interface for improved performance. However, the CNC interlayer increased the transport resistance of substrate and compromised the flux enhancement of the PA layer, limiting the further increase of the water permeance.

Chapter 3: In this chapter, a thin coating on substrate was applied instead of the nanomaterial interlayer expecting a further increase of the water permeance. Specifically, a polyphenol-metal-assisted method was designed to regulate the structure of PEI-based polyamide NF membranes. Tannic acid (TA) was first deposited onto the substrate, followed by the impregnation of the Cu^{2+} ions-incorporated aqueous PEI monomer solution to establish ternary interactions among PEI, TA, and Cu^{2+} ions. Based on the synergistic effect of ternary interactions, the resultant PA-TA-Cu membrane possesses ultrathin thickness (≈11 nm), high positive charge, and relatively loose structure. It exhibited a high $MgCl_2$ rejection (95.9 %) and a low LiCl rejection (17.1%), with a pure water permanence of 4.87 L m^{-2} h^{-1} bar^{-1}. Furthermore, the NF membrane exhibits a high Mg^{2+}/Li^{+} separation factor (26.5) and excellent long-term

stability. This study provides an efficient strategy for fabricating an excellent NF membrane for lithium extraction from salt-lake brines. However, the fabrication process was cumbersome, including two steps, and the TA modification process is time consuming (24 h).

Chapter 4: In order to simplify the process, adjust the IP reaction and improve distribution of aqueous phase on the substrate at the same time, suitable additive need to be used. In this chapter, sodium n-decyl sulfate (SDES) with different critical micelle concentrations (CMC) were incorporated into the PEI aqueous phase to regulate the IP reaction. The incorporation of SDES enhances the wettability of the aqueous solution, improving the loading amount of PEI monomers on the polysulfone (PSf) substrate. The lower aqueous/organic interface tension increases the interfacial instability and makes it easier to deform. In addition, the SEDS facilitates the spatially uniform diffusion of PEI monomers during the IP process. The optimized PA-0.25CMC membrane possesses a crumpled and loose structure, and exhibited a high $MgCl_2$ rejection (92.6 %) and a low LiCl rejection (21.5 %), with a pure water permanence of 5.65 L m^{-2} h^{-1} bar^{-1}. After filtration, the Mg^{2+}/Li^{+} ratio decreased from the initial 40 (feed) to 3.08 (permeate). This study provides an efficient strategy to fabricate the PEI/TMC-based NF membranes with high Mg^{2+}/Li^{+} separation performance.

Chapter 5: A summary of this dissertation is given.

Chapter 2

Complexation of cellulose nanocrystals and amine monomer for improved interfacial polymerization of nanofiltration membrane

2.1. Introduction

Water purification and the extraction of high-value solutes from wastewater have been extensively studied in recent years [122, 123]. Membrane technology is considered an efficient solution for water purification and solute recovery owing to its energy efficiency. Nanofiltration membranes with a molecular weight cut-off (MWCO) between 200 Da and 1000 Da have the potential to separate divalent and monovalent ions, remove heavy metals, and recover high-value solutes [62, 124]. Thin film composite (TFC) membranes are the most widely used nanofiltration membranes and typically consist of a top polyamide (PA) active layer and a bottom porous substrate. PA active layers are mostly fabricated by interfacial polymerization between amine monomers in the aqueous phase and trimesoyl chloride (TMC) in the organic phase [125]. However, the trade-off between the permeability and selectivity of TFC membranes limits further improvement of the separation performance [121]. Producing PA membranes with higher water permeance without compromising their salt rejection ability is still a challenge. Some membrane properties, such as the effective filtration area, membrane thickness, and surface charge density [126, 127], limit the improvement of separation performance. Thus, improving the specific filtration area, decreasing the thickness, and adjusting the surface charge density of polyamide film are effective strategies to improve the permeability and selectivity of the nanofiltration membranes [62].

Over the past few decades, many effective methods have been proposed to construct a PA layer with a homogeneous microstructure, therefore overcoming the trade-off restriction between membrane permeability and selectivity. On the one hand, many types of functional nanomaterials were incorporated into the aqueous phase to fabricate the thin film nanocomposite (TFN) membrane, such as graphene oxide (GO) [128], carbon nanotube (CNT) [107], covalent organic frameworks (COF) [129], metal-organic frameworks (MOF) [130], and cellulose nanocrystals (CNC) [131, 132]. These nanomaterials in PA can construct additional nanochannels and effectively enhance the permeability of nanofiltration membranes. However, some issues need to be addressed, including the poor dispersion in aqueous solution, weak adhesion between nanomaterials and PA matrix, uncontrolled distribution, and limited loading amount in PA matrix. These challenges hampered the development of high-performance TFN membranes [120]. On the other hand, an interlayer can be constructed on the substrate to modify the surface properties (surface porosity and hydrophilicity), regulating the kinetics of the IP reaction. The resulting interlayered-thin film composite (i-TFC) membranes usually exhibit unique nanostructures, such as bubble, tube, spot, and stripe-like structures to increase the effective filtration area [126].

In particular, constructing a dense and continuous PA selective layer is the key to improving ion selectivity. Thus, the distribution and availability of amine monomers at the aqueous–organic solvent interface or the substrate should be optimized in the IP reaction [71, 133, 134]. For the i-TFC membrane, a smooth, hydrophilic, and isotropic interlayer usually can improve the distribution and diffusion uniformity of amine monomers. To enhance the distribution of amine monomers, previous works have tried to construct a substrate or interlayer with some interactions with amine monomers [62]. Pre-enrichment of the amine monomers at the interface can facilitate the formation of a defect-free PA selective layer. Nevertheless, most literature uses a two-step method, which involves intermediate layer construction and subsequent amine monomer enrichment. Therefore, appropriate optimization of experimental conditions and operation procedures are necessary to efficiently produce high-performance

membranes.

In this study, to improve the permeability without sacrificing the salt rejection of nanofiltration membranes, complexed amine monomers (polyethyleneimine, PEI) and CNC were prepared for deposition on a polysulfone (PSf) substrate via a one-step vacuum-assisted procedure and subsequently crosslinked them with TMC to fabricate interlayered-thin film nanocomposite (i-TFN) [35] nanofiltration membranes (**Fig. 2.1**). One-dimensional CNC can tightly contact each other and form a uniform and continuous network more easily [135]. Compared to traditional i-TFC and TFN membranes, the i-TFN membrane can control the loading amount of CNC and maximize its functionality. The co-deposition of nanomaterials and amine monomers can construct an intermediate layer, enriching and improving the distribution of amine monomers for the IP process. Meanwhile, it simplified the operation procedure by combining the interlayer fabrication and amine monomer loading into one step. Meanwhile, a large number of functional groups of CNC endow it with excellent compatibility with the PA matrix and can capture and enrich more PEI monomers during the IP process, resulting in the uniform distribution of amine monomers and the generation of defect-free PA films [136]. Besides, the strong electrostatic interaction between CNC and PEI can restrict the release and diffusion behavior of the amine monomer during IP, resulting in membranes with a crumpled structure and a retained dense polymer network. Thus, this method is expected to optimize amine loading and distribution for the IP reaction and enlarge the effective membrane area for filtration. The hydrophilic CNC interlayer also can accelerate the adsorption and diffusion of water molecules through a “dragging effect” [135, 137]. The role of CNC in controlling the IP conditions and membrane structure formation were investigated to gain insights into the synthesis–structure–performance relationship for the PA film.

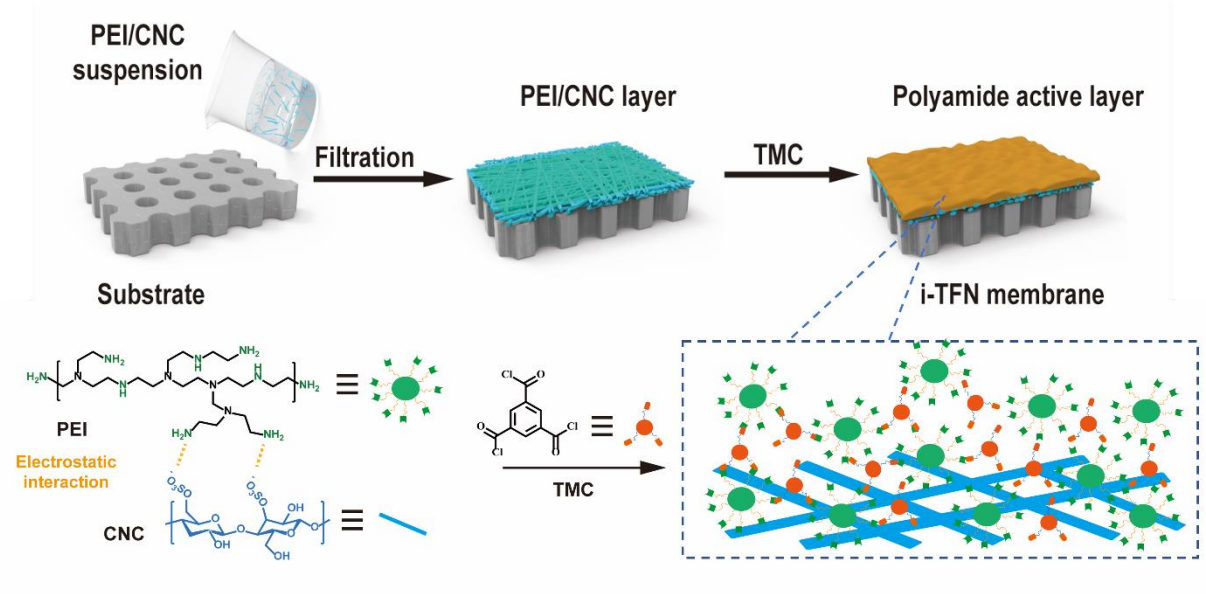

Fig. 2.1 Schematic illustration of the fabrication process for the vacuum-assisted i-TFN nanofiltration membrane.

2.2. Experimental

2.2.1. Materials and chemicals

A commercial PSf ultrafiltration substrate with a MWCO of approximately 30 kDa was provided by the Nitto Denko Corporation (Osaka, Japan). Microcrystalline cellulose powder (MCC) and TMC were purchased from Sigma Aldrich (MO, US). The PEI (MW = 1800 Da), sodium chloride (NaCl, 99.5%), lithium chloride (LiCl, 98%), sodium sulfate (Na_2SO_4, 99%), magnesium chloride hexahydrate ($MgCl_2 \cdot 6H_2O$, 98%), magnesium sulfate ($MgSO_4$, 98%), n-hexane (96%) and ethanol (EtOH, 99.5%) were purchased from Fujifilm Wako Pure Chemical Co., Tokyo, Japan. A Milli-Q water purification system (Milli-Q Integral 3 system; Millipore S.A.S., Molsheim, France) was used to produce deionized (DI) water for the experiments.

2.2.2. Preparation of CNC suspension

MCC was used as the raw material to produce a CNC suspension using the sulfuric acid hydrolysis method [137, 138]; the detailed route is presented in **Fig. 2.2**. In brief, MCC (6.6 g) was added to a preprepared 64% (w/w) H_2SO_4 aqueous solution (100 g),

and the mixture was stirred vigorously in an ice bath. Subsequently, the solution was transferred to an oil bath and warmed to 45 °C for 4 h. After a predefined time, the brown mixture was cooled to room temperature and diluted 10-fold with DI water to terminate the reaction. After overnight incubation, the obtained product was washed three times using centrifugations at 10000 rpm for 15 min to remove the supernatant. Subsequently, the suspension was further dialyzed with DI water until the wash water became neutral (usually after one week) to remove any residual unreacted acid. Finally, the product was sonicated using an ultrasonic device for 1 h to obtain a homogeneously dispersed CNC suspension. The concentration of the prepared CNC suspension, which was calculated using the freeze-drying method, was approximately 10 g L^{-1}.

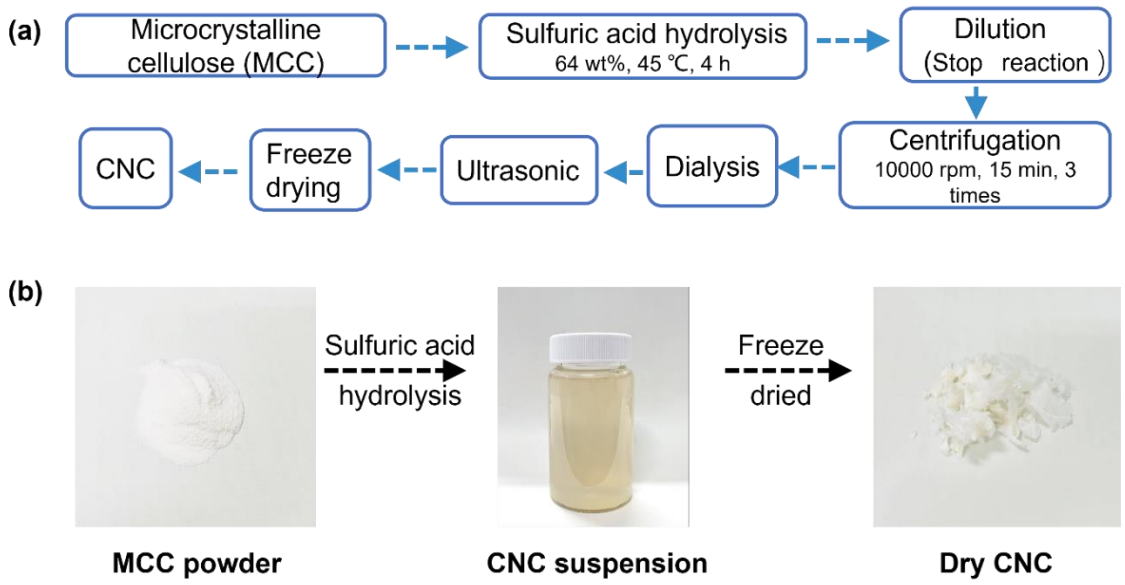

Fig. 2.2 (a) Flow chart of CNC fabrication using the sulfuric acid hydrolysis method; (b) digital images of the MCC powder, CNC suspension (10 g L^{-1}), and dry CNC.

2.2.3. Fabrication of i-TFN membranes

First, a commercial PSf ultrafiltration membrane was cut into a circle with a diameter of 5 cm and immersed in an EtOH/DI water solution (50 wt%) at room temperature overnight to remove glycerin. The membranes were removed and rinsed several times with DI water before use. The prepared CNC suspension (1 g L^{-1}) was

dispersed into the PEI aqueous solution (50 mL, 0.5 wt%) with different volumes (5 μL, 50 μL, 100 μL, and 300 μL), and the mixture suspension was sonicated for 15 min to obtain a homogeneously dispersed PEI/CNC suspension. TMC (0.15 g) was dissolved in n-hexane (100 mL) to obtain the organic phase. The vacuum-assisted IP method, which has been reported to improve the uniform distribution of the amino monomer more than traditional aqueous immersion methods [139], was used in this study. A schematic diagram of the fabrication procedure is shown in **Fig. 2.1 and Fig. 2.3**. In this process, the rinsed PSf ultrafiltration membrane was fixed in a filtration flask, and the corresponding inner filtration area of the filter cup was approximately 12.56 cm^2. The PEI/CNC suspension was then poured onto the membrane and filtered under a pressure of approximately 1 bar. When the solution disappeared from the surface, all membranes were filtered for another 1 min to remove the excess aqueous solution. The PEI/CNC deposited substrates were denoted as PSf-PCX according to different CNC suspension (1 g L^{-1}) volumes (X = 5 μL, 50 μL, 100 μL, and 300 μL) in the PEI/CNC mixture. Subsequently, the pre-prepared TMC/n-hexane solution (10 mL) was poured onto the membrane surface to react with PEI, which was discarded after 3 min. Subsequently, the whole filtering flask with the membrane was transported into an oven and cured for another 10 min at 70 °C. Finally, the fabricated i-TFN membranes were removed and soaked in DI water until use. The i-TFN membranes were denoted as PA-PCX according to the CNC suspension volume (X = 5 μL, 50 μL, 100 μL, and 300 μL). When the CNC was not used, the fabricated TFC membrane was denoted as PA-PEI. In this study, the CNC was deposited on supports by vacuum filtration due to its feasibility. For large-scale use, other methods like spraying are also considered to be effective for this deposition. In addition, a traditional polyamide nanofiltration membrane was prepared for comparison (**Fig. 2.3**). The PEI solution was poured directly onto the substrate surface for 5 min, and the residual solution was removed using an air gun. Subsequent operations were consistent with the vacuum-assisted IP method described above. The prepared membranes were named PA-PEI (T), where T represents the traditional aqueous immersion method. The CNC concentrations in the

labeled membranes are listed in **Table 2.1**.

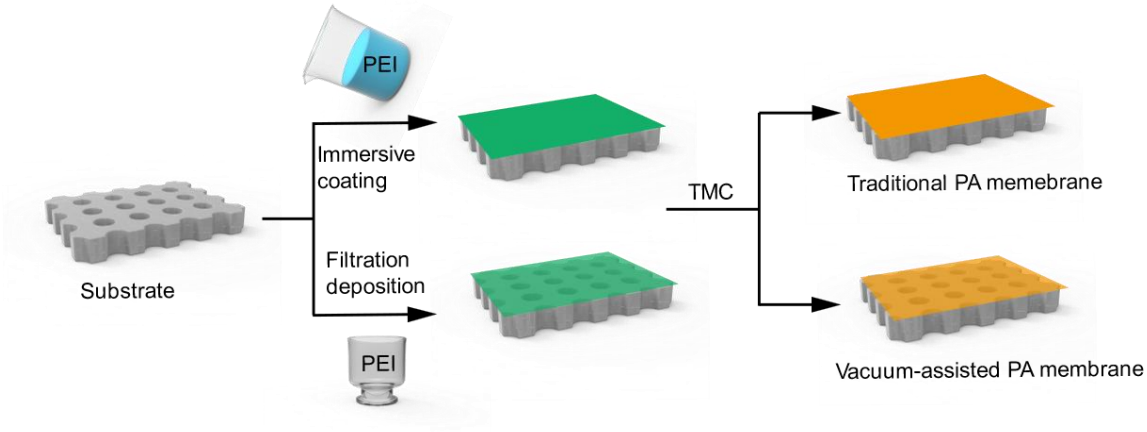

Fig. 2.3 Schematic illustration of the fabrication process for the traditional and vacuum-assisted nanofiltration membrane.

Table 2.1. CNC concentrations correspond to the different membranes.

Types of membrane		1 g L^{-1} CNC (μL)	5 g L^{-1} PEI (mL)	Fabrication methods
Substrate	PSf-PEI	0	50	Vacuum
	PSf-PC5	5	50	Vacuum
	PSf-PC50	50	50	Vacuum
	PSf-PC100	100	50	Vacuum
	PSf-PC300	300	50	Vacuum
PA membrane	PA-PEI(T)	0	50	Traditional
	PA-PEI	0	50	Vacuum
	PA-PC5	5	50	Vacuum
	PA-PC50	50	50	Vacuum
	PA-PC100	100	50	Vacuum
	PA-PC300	300	50	Vacuum

2.2.4. Characterization

The microstructures and roughness of the prepared membranes were observed using field-emission scanning electron microscopy (FESEM; JSF-7500F, JEOL, Ltd.,

Tokyo, Japan) and atomic force microscopy (AFM; SPI3800 N, Hitachi Ltd., Tokyo, Japan). The chemical element composition of the membrane was analyzed using Fourier-transform infrared spectroscopy (FTIR; ALPHA, Bruker, Billerica, MA, USA) and X-ray photoelectron spectroscopy (XPS; JPS-9010 MC, JEOL, Ltd., Tokyo, Japan), using Al Kα radiation. Water contact angles (WCA) were measured using a contact-angle testing system (Drop Master 300; Kyowa Interface Science Co., Ltd., Tokyo, Japan) to evaluate membrane wettability. At least three samples fabricated from different batches were used to measure the WCA and the average value was used. The zeta potential of the membrane was determined using an electrokinetic analyzer (Anton Paar SurPASSTM 3, Austria) to analyze the surface charge properties. The size distributions of the CNC suspension and PEI/CNC mixture solution were determined using dynamic light scattering (DLS; ELSZ-1000 ZA, Otsuka Electronics Co., Ltd., Osaka, Japan).

2.2.5 Evaluation of the diffusion of PEI from aqueous into organic phase

The diffusion experiment was conducted under the same condition as the membrane fabrication process, except no TMC was added to the n-hexane. Firstly, 10 mL PEI aqueous with different concentrations of CNC was poured into a 25 mL glass container. Then, 10 ml n-hexane was gently injected into the aqueous solution. After 3 min, 2 mL n-hexane was taken out using a pipette and put into quartz cuvettes. The ultraviolet-visible (UV–vis) spectroscopy (V-650KE, JASCO Company, Japan) was used to measure the absorbance variation of PEI in n-hexane [140-142]. PEI exhibited the typical absorption peak at 198 nm, and the peak intensity was used to evaluate the PEI concentration in n-hexane.

2.2.6 Evaluation of membrane performance

The separation performance of the prepared membranes was evaluated using a laboratory-scale cross-flow filtration setup with an effective filtration area of approximately 7.06 cm^2 [91]. The flow rate was fixed at 9.9 mL min^{-1}, and all the

fabricated membranes were pre-compacted at 10 bar for 1 h until a stable permeating flux was achieved. DI water was used to test the pure water permeance, and the permeance (J; L m^{-2} h^{-1} bar^{-1}) of the membrane was calculated through the following equation (2.1):

$$J = \frac{\Delta V}{A \, \Delta t \, \Delta P} \tag{2.1}$$

where V (L) is the volume of the permeate solution, A (m^2) is the effective filtration area, Δt (h) is the filtration time difference, and ΔP (bar) is the operating pressure difference. At least three samples fabricated from different batches were used to measure the pure water permeance and the average value was used.

The effective salt rejection (%) was calculated by the following equation (2.2):

$$Rejection = \left(1 - \frac{C_P}{C_f}\right) \times 100\% \tag{2.2}$$

where C_P and C_f represent the salt concentrations in the permeate and feed solutions, respectively. The 2000 ppm of different single inorganic salts ($MgCl_2$, LiCl, NaCl, $MgSO_4$, and Na_2SO_4) in aqueous solutions were used as feed solutions. The concentration was determined using conductivity measurements (Ultrameter II^{TM}4P, Myron L Company, Japan). At least three samples fabricated from different batches were used to measure the salt rejection and the average value was used.

The total transport resistance of the i-TFN membranes (R_0; bar h m^{-1}) [143, 144], which consists of the resistance from the top PA (R_1) selective layer and the PSf or PSf-PCX substrate (R_2), was calculated using the following equation:

$$R_1 = R_0 - R_2 = \frac{1}{J_0} - \frac{1}{J_2} \tag{2.3}$$

where J_0 and J_2 represent the permeances of the i-TFN membrane and PSf or PSf-PCX substrates, respectively.

To test the separation performance of the i-TFN membrane for Mg^{2+} and Li^+, 2000 ppm Mg^{2+}/Li^+ mixture solutions with different Mg^{2+}/Li^+ mass ratios (10:1, 20:1, and 40:1) were used to simulate salt lakes with different concentrations. The corresponding selective separation factor was calculated using the following equation:

$$S_{Mg^{2+}/Li^+} = \frac{C_F(Mg)/C_F(Li)}{C_P(Mg)/C_p(Li)} \tag{2.4}$$

where C_F (Mg) and C_F (Li) and C_P (Mg) and C_P (Li) represent the concentrations of Mg^{2+} and Li^+ in the feed and permeate solutions, respectively. The concentrations of Mg^{2+} and Li^+ in the mixed solutions were determined using an inductively coupled plasma emission spectrometer (ICPOES, Shimadzu, Japan).

The MWCO of the fabricated i-TFN membranes was evaluated using rejection tests with four sugars of different molecular weights (1000 ppm). The sugars used were glycerol (92 Da), D-(+)-glucose (180 Da), sucrose (342 Da), and D-(+)-raffinose pentahydrate (504 Da). The rejections of these sugars were calculated based on concentration data obtained from the total organic carbon analyzer (TOC-VCSN, Shimadzu Co., Japan).

2.2.7 Molecular dynamics (MD) simulations

MD simulations were conducted to characterize the diffusion properties of PEI in the PEI-water system and the PEI/CNC-water system to assess the effect of CNC on PEI during the IP process and verify whether the diffusion behavior of PEI would affect the physicochemical properties of the polyamide layer.

All MD simulations were performed using the Forcite module with the Condensed-phase Optimized Molecular Potential for Atomistic Simulation Studies II (COMPASS II) force field in Materials Studio 2020. A simulation box (dimensions: 39.8 Å × 39.8 Å × 39.8 Å) with periodic boundary conditions applied in all three dimensions was built for each system in this work. For the PEI-water system, the periodic unit was composed of one PEI molecule and 2000 water molecules. For the PEI/CNC-water system, a repeating unit of CNC was added and fixed in the system containing one PEI molecule and 2000 water molecules. For each system, after the model construction, a geometry optimization process was first performed, followed by a dynamic run for 1 ns with NPT (constant number of molecules, pressure, and temperature) ensemble at 298 K. To make sure all systems have reached equilibrium, another run for 5 ns with NVT (constant number of molecules, volume and temperature) ensemble was applied, and the energy as well as temperature of all systems reached the

steady values. The simulation results of the final 4 ns run in NVT were used for data analysis.

The diffusion coefficients (D, $m^2\ s^{-1}$) of PEI molecules in the two systems were analyzed from the slope of mean square displacement (*MSD*) curves by Einstein relationship [103, 109, 145, 146]:

$$\mathrm{MSD}= \frac{1}{\mathrm{N}}\sum_{1}^{\mathrm{N}}\{[\mathrm{r}\ (\mathrm{t})\ \text{-}\mathrm{r}\ (0)]^2\} \tag{2.5}$$

$$\mathrm{D}= \frac{1}{6}\lim_{\mathrm{N}\to\infty}\frac{\mathrm{d}}{\mathrm{dx}}\{[\mathrm{r}\ (\mathrm{t})\text{-}\mathrm{r}\ (0)]^2\} \tag{2.6}$$

where N is the number of PEI molecules, r (0) and r (t) represent the initial position (m) and position at t (m) of the PEI molecule.

2.3 Results and discussion

2.3.1 CNC and PEI/CNC interlayer

The CNC suspension was prepared from MCC powder using the sulfuric acid hydrolysis method (**Fig. 2.3**) [147, 148]. The high concentration of the sulfuric acid solution can remove the amorphous region in the MCC and endow the reserved CNC with a large amount of sulfuric acid ester groups (**Fig. 2.4a**). FTIR spectroscopy of MCC and CNC powders is shown in **Fig. 2.4b**. The wide peaks in the range 3825–3335 cm^{-1} and 1250–1350 cm^{-1} are associated with the O-H and S=O stretching vibrations, respectively, which correspond to the CNC chemical structure and are consistent with previously reported studies [147]. The corresponding AFM profiles (**Fig. 2.4c**) further indicate the successful synthesis of CNC [147]. The rod-like CNC possesses a length and diameter of approximately 200–500 nm and 5–7 nm, respectively.

Because of sulfuric acid ester groups, CNC exhibits a strong negative charge [149, 150]. PEI, conversely, is one of the most common cationic polyelectrolytes, exhibiting a strong positive change, and it has been applied to prepare positively charged membranes via the IP method [90, 92]. Therefore, CNC can adsorb PEI molecules via complexation owing to strong electrostatic interactions [151, 152], which may alter the amine distribution for the subsequent IP with TMC. **Fig. 2.4d** shows images of the PEI/CNC mixture solutions with different mass ratios. With the addition of a small

amount of PEI molecules (the PEI/CNC mass ratio was 5:1), visible flocculation of CNC appeared in the suspension showing the strong electrostatic interactions between PEI and CNC. Moreover, the corresponding size distribution of flocculation particles increased from 116.5 ± 20.6 nm to 7557.2 ± 1241.8 nm (**Fig. 2.4e**). However, when the mass ratio was increased to 50:1, the mean particle size of complexed PEI/CNC decreased to 179.0 ± 34.6 nm, similar to the original CNC suspension, owing to the electrostatic repulsion between excessive PEI molecules and PEI-modified CNC, indicating that the addition of excessive PEI molecules was beneficial to obtain a uniformly dispersed PEI/CNC complex solution (**Fig. 2.4f**).

Subsequently, the mixture was filtered onto PSf membranes to fabricate the modified substrate for the subsequent IP procedure (**Fig. 2.1 and Fig. 2.3**). XPS was used to characterize the changes in the chemical composition of the pristine, PEI-deposited, and PEI/CNC-deposited membranes (**Fig. 2.4g**), namely, the PSf, PSf-PEI, and PSf-PC membranes. Compared to the pristine PSf membrane, new N 1s peaks were observed on the membrane surface after filtration of the PEI solution and mixed PEI/CNC suspension, confirming the presence of PEI on the membrane surface. The O 1s peak intensity enhancement on the PSf-PC surface was primarily derived from the large number of hydroxyl groups of CNC. Notably, although CNC contains some sulfonic acid ester groups, no obvious S peak could be distinguished in the PSf-PC membrane spectra, possibly because of its small quantity and relatively weak intensity. **Fig. 2.4h** shows the changes in the zeta potential of these membranes, which exhibit opposite charges before and after PEI/CNC deposition in the pH range of 5–8. In contrast to the pristine PSf membrane, both PSf-PEI and PSf-PC membranes exhibit a more positive surface charge, which is attributed to the presence of PEI. Although CNC has strong negative charges, the PEI/CNC coating still presents a positive surface charge because the CNC can adsorb and enrich more PEI monomers on the membrane surface through electrostatic interactions, preventing the penetration of PEI into the pores of PSf during the deposition process. These results indicate the successful construction of the PEI/CNC layer on the PSf membrane surface, which may modify

the surface properties.

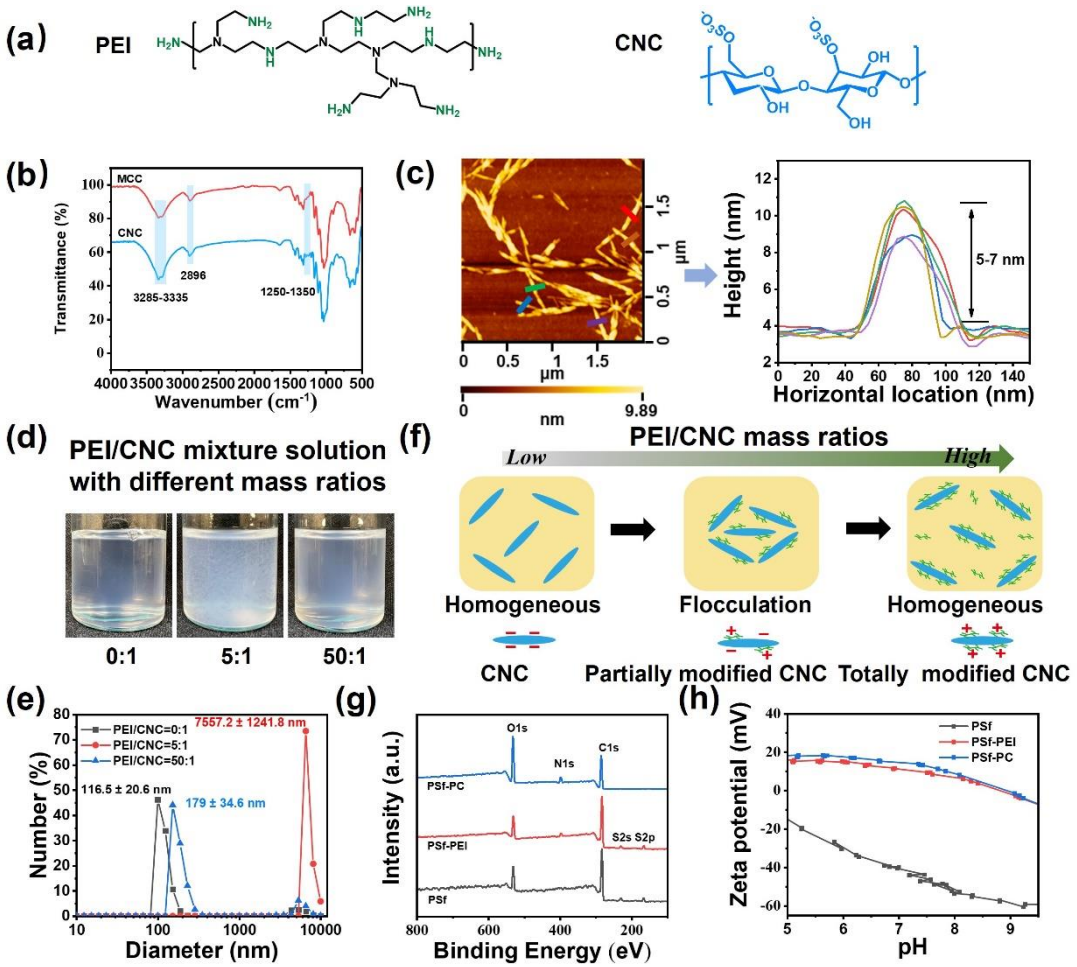

Fig. 2.4 (a) Chemical structures of PEI and CNC; (b) FTIR spectra of MCC and CNC powders; (c) AFM image and high profiles of CNC; (d, e) digital images and corresponding size distribution of PEI/CNC mixture solution with different mass ratios; (f) schematic illustration of the electrostatic interaction between PEI and CNC with a low or high PEI/CNC mass ratio; and (g, h) XPS profiles and zeta potential of the pristine PSf, PSf-PEI, and PSf-PC membranes. The mass ratio of PEI/CNC in the PSf-PC membrane here was 2500 by adding 100 μL CNC suspension (1 g L^{-1}) into the PEI solution (50 mL, 0.5 wt%) for the deposition.

2.3.2 Interfacial polymerization with interlayers

Different volumes (5 μL, 50 μL, 100 μL, and 300 μL) of CNC suspension (1 g L^{-1}) were added into the PEI solution (50 mL, 0.5 wt%), with PEI/CNC mass ratios were

50000, 5000, 2500, and 833, respectively. These mass ratios were sufficiently high to obtain a uniformly dispersed PEI/CNC solution. PEI/CNC layers were then fabricated via vacuum-assisted filtration of the above solutions on a PSf substrate (denoted as PSf-PC5, -PC50, -PC100, and -PC300). The concentration of the CNC in the PEI/CNC deposition procedure was adjusted to determine its effects on the surface properties of the PSf membrane. When only PEI (PSf-PEI) was employed for the deposition without CNC complexation, the morphology was similar to that of the pristine PSf membrane (**Fig. 2.5**). In contrast, with the complex incorporation of CNC, the one-dimensional CNC contributed to the formation of a continuous network and gradually covered the pores of the PSf substrate.

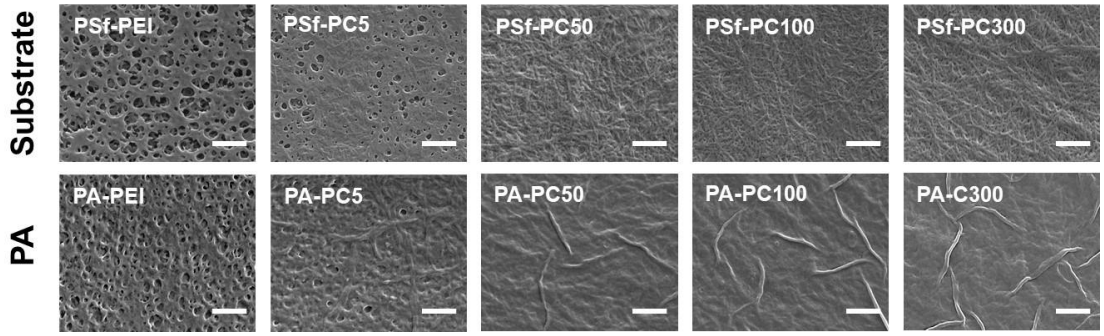

Fig. 2.5 SEM images for substrate TFC and i-TFN membrane surface morphologies (the scale value is 500 nm).

Compared to the pristine PSf membrane, the PEI/CNC layer significantly improved the hydrophilicity of the substrate (**Fig. 2.6a**). This excellent wettability can be attributed to the abundant hydroxyl and amino groups of the CNC and PEI molecules. With the deposition of the PEI solution, the PEI molecules entered and blocked the inner pores of the PSf substrate, resulting in a significant decrease in the permeance from 770 L m^{-2} h^{-1} bar^{-1} to 100 L m^{-2} h^{-1} bar^{-1} (**Fig. 2.6b** and **Table 2.2**; PSf and PSf-PEI). When the CNC was incorporated and deposited on the substrate (PSf-PC5), it adsorbed and enriched many PEI molecules on the top surface of the PSf membrane, avoiding blocking the inner pores of the substrate. With an increase in CNC content, an increasing number of CNC remained on the surface (from PSf-PC5 to PSf-PC300), and

the thickness of the PEI/CNC interlayer increased (**Fig. 2.7**). AAO substrates were used for the deposition of PEI and different PEI/CNC layers for clear observation of the deposited layer thickness. Seen from the surface image of AAO-PC100, the one-dimensional CNC fully covered the pores of the AAO substrate, similar to the PSf-PC100 membrane (**Fig. 2.5**). A thicker layer increases the resistance of the substrate, resulting in a decrease in water permeance.

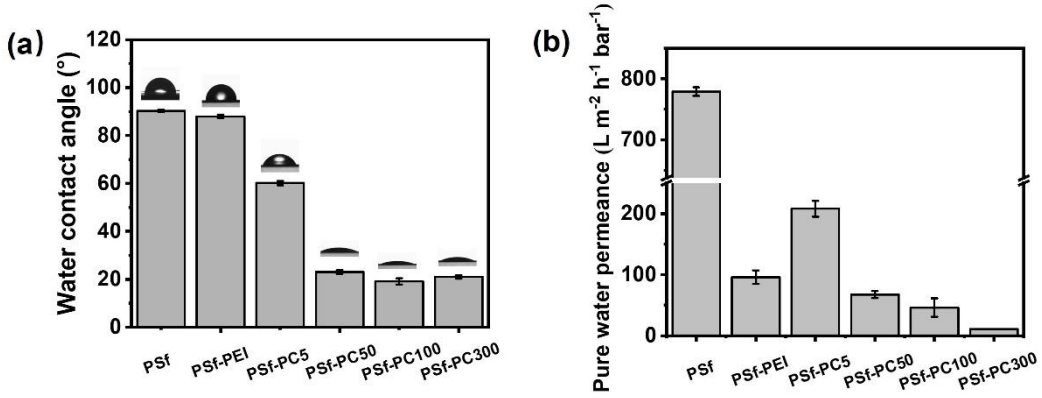

Fig. 2.6 (a) Water contact angles and (b) pure water permeance of pristine and modified substrates.

Table 2.2 Pure water permeance of substrates and PA membranes.

Substrate	Permeance of substrate (L m^{-2} h^{-1} bar^{-1})	**PA/substrate**	Permeance of PA/substrate (L m^{-2} h^{-1} bar^{-1})
PSf	779.35	PA-PEI(T)	0.41
PSf-PEI	96.21	PA-PEI	0.74
PSf-PC5	208.65	PA-PC5	1.62
PSf-PC50	67.60	PA-PC50	2.40
PSf-PC100	45.15	PA-PC100	2.62
PSf-PC300	10.85	PA-PC300	2.94

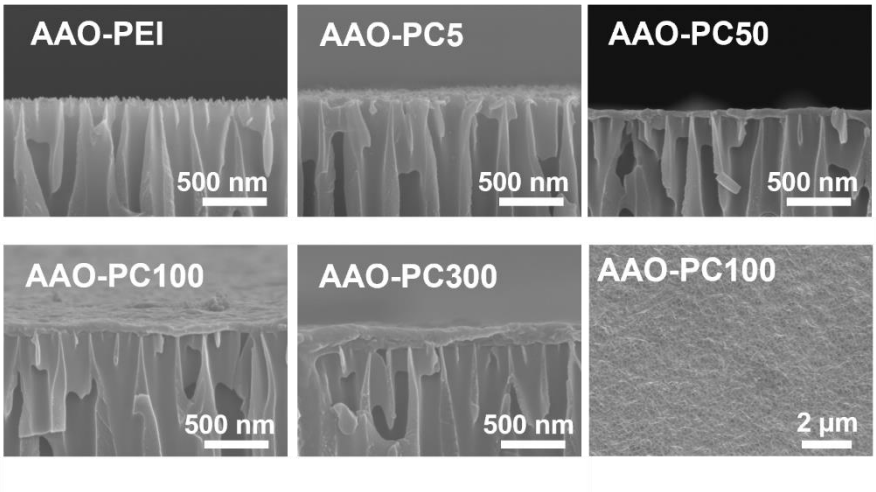

Fig. 2.7 Cross-sectional SEM images of Anodic aluminum oxide (AAO)-PCX substrate and the top surface image of AAO-PC100 substrate.

Subsequently, IP was conducted by directly pouring the TMC-in-hexane solution onto these substrates to determine whether the morphology of the formed PA membranes changed accordingly. For the PA membrane formed on the PSf-PEI substrate (denoted as PA-PEI), in which CNC was not used, the surface morphology resembled that of the original PSf with the shape of the surface pores on the PSf substrate (**Fig. 2.5 and Fig. 2.8**). However, a crumpled PA surface morphology gradually appears with the incorporation of CNC deposited on the substrate. The different morphologies of the PA membranes formed are believed to be related to the altered surface properties of the PEI/CNC complex. The interactions between PEI and CNC considerably limit the diffusion rate of PEI toward the organic phase, as validated by both experimental and simulation results (**Fig. 2.9**), and the effect significantly increased with the increased CNC concentration. The unstable aqueous/organic interface for IP results in the generation of the crumpled structure [62]. In addition, due to the high hydrophilicity of the substrate with PEI/CNC layer (**Fig. 2.6a**), water template could be formed on the substrate surface, which also possibly contributes to the formation of the crumpled structure [98, 117, 153].

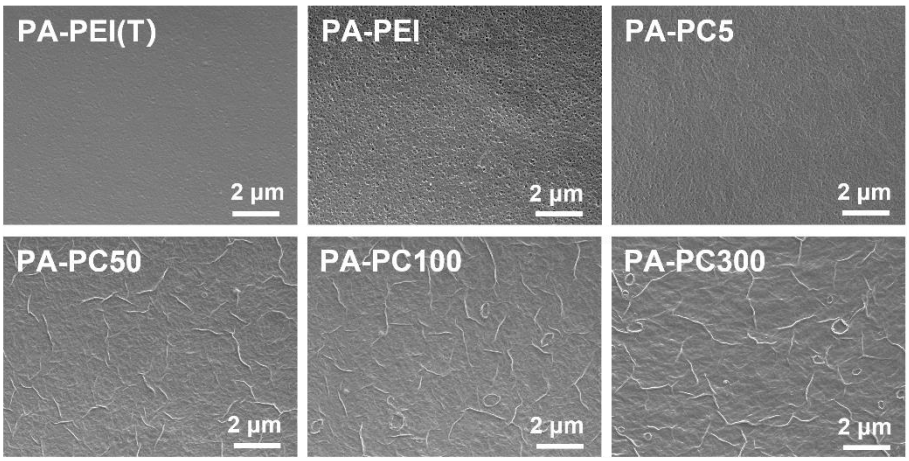

Fig. 2.8 SEM images of PA membranes.

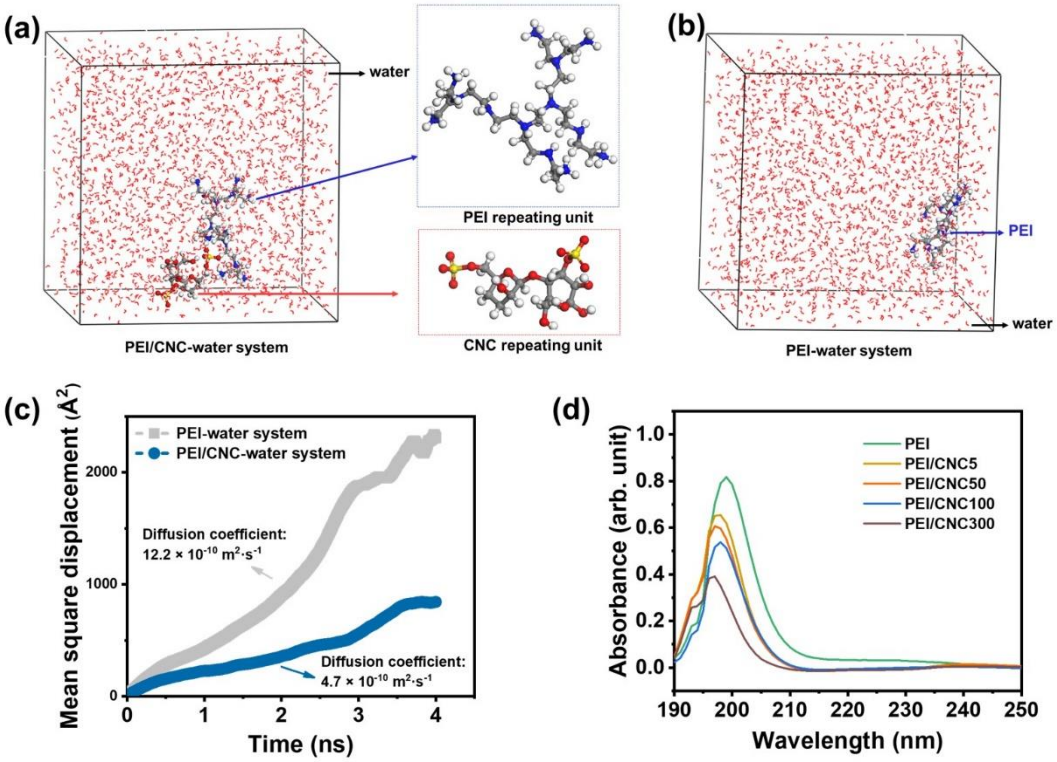

Fig. 2.9 Diffusion properties of PEI in aqueous systems by MD simulations. (a) Snapshot of the PEI/CNC-water system (dimensions: 39.8 Å × 39.8 Å × 39.8 Å); (b) Snapshot of the PEI-water system (dimensions: 39.8 Å × 39.8 Å × 39.8 Å); (c) Diffusive properties of PEI in the PEI-water and the PEI/CNC-water systems; (d) UV-vis spectra of PEI in organic phase after 3 mins diffusion.

The construction of the CNC layer and the crumpled structure on the membrane

surface also contributed to the surface hydrophilicity of PA (**Fig. 2.10a)**. Moreover, the pure water permeance increases approximately three times more than that of the pristine PA membranes, from 0.74 L m^{-2} h^{-1} bar^{-1} to 2.62 L m^{-2} h^{-1} bar^{-1} (**Fig. 2.10b** and **Table 2.2**), owing to the "dragging effect" of the interlayer and the increased contact area from the crumpled structure. In addition, the thinner thickness of the PA-selective layer also plays a role in improving membrane permeability (**Fig. 2.10c**). Briefly, to observe the active layer on the substrate, an anodic aluminum oxide (AAO) substrate was also used for the i-TFN membrane fabrication. The total layer thickness of the PA for AAO-PA-PEI and PA and PEI/CNC for AAO-PA-PC membrane was similar. Although the boundary between the CNC intermediate layer and the top PA film is difficult to distinguish, considering the thicker layer of PEI/CNC than bare PEI (**Fig. 2.7**), the actual PA layer thickness in AAO-PA-PC should be thinner than the one in AAO-PA-PEI. From the surface image of AAO-PA-PC100, a similar crumpled structure also can be observed, showing the PA film fabricated by the vacuum-assisted IP method is independent of the substrate. Therefore, this method in this work is a general method applicable to different substrates.

A 2000 ppm $MgCl_2$ solution was used to determine the salt rejection performance of the TFC and i-TFN membranes. The PA-PEI membrane exhibited relatively high $MgCl_2$ rejection (**Fig. 2.10b**). With the incorporation of a small amount of CNC, the $MgCl_2$ rejection of the PA-PC5 membrane exhibited a slight decrease. This phenomenon should be ascribed to the presence of the loose regions in the PA film owing to the unevenly distributed CNC on the PSf membrane (**Fig. 2.5).** When the CNC partially covered the PSf substrate, the strong electrostatic interaction between CNC and PEI might cause the uneven local distribution of PEI, especially at the edge of CNC layer, leading to certain loose regions in the generated PA layer. With increased CNC incorporation, the CNC layer fully covered the PSf substrate surface, and many PEI molecules were anchored on the surface to react with more TMC monomers, resulting in the formation of a dense and continuous PA-selective layer (PA-PC50 and PA-PC100), thus maintaining a high rejection of the $MgCl_2$ solution (>96.5%). In particular,

the PA-PC100 membrane had a three-fold higher water permeance than the pristine membrane without compromising salt rejection performance, thus surpassing the trade-off of this membrane. Further increasing the loading amount of CNC resulted in a slight decrease in $MgCl_2$ rejection, which was attributed to the low cross-linking of PA film resulting from the low amount of PEI molecules on the surface. Meanwhile, the performance of pristine PA membranes fabricated by traditional aqueous immersion and vacuum filtration methods was compared in **Table 2.2**. The PA membrane fabricated by the vacuum filtration method exhibits higher permeance and salt rejection performance, which is consistent with the sequence-reported literature [139], confirming the advantage of the vacuum filtration method.

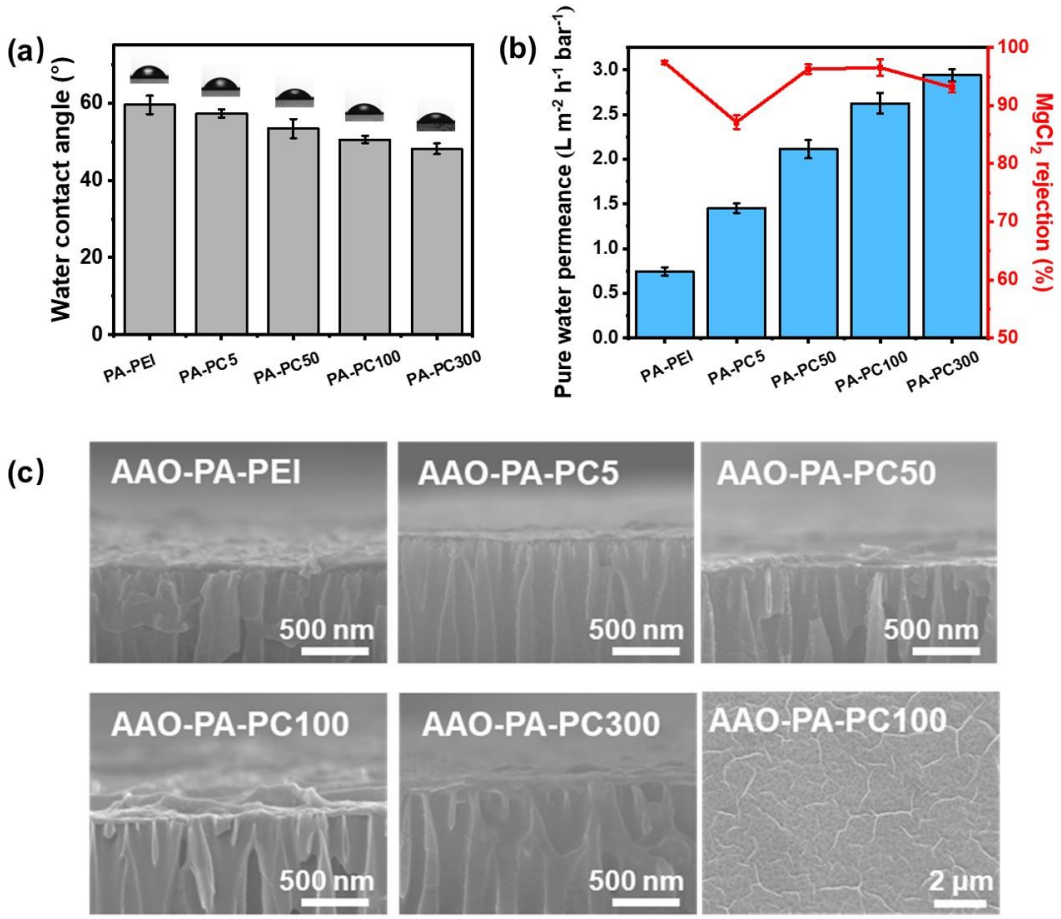

Fig. 2.10 (a) Water contact angles of i-TFN membranes; (b) pure water permeance and $MgCl_2$ salt rejection of TFC and i-TFN membranes; (c) cross-sectional SEM images of AAO-PA-PCX i-TFN membranes and the top surface image of AAO-PA-PC100 substrate.

2.3.3 Effect of roughness and transport resistances of the membranes

The surface root mean square roughness (RMS) of both the substrate and PA membranes was examined to determine the role of the complexed PEI/CNC in the permeance contribution of the resulting PA membrane (**Fig. 2.11a**). The results demonstrated that the roughness of the PSf-PCX substrate and PA-PCX membranes increased with the incorporation of CNC and that their relationship was linear. Rougher substrates were conducive to the formation of a higher-roughness PA-selective layer. Notably, the corresponding slope value is 4.25, which is significantly greater than 1, indicating that, compared to the influence of the substrate, the formation of a crumpled morphology plays a more crucial role in improving the roughness of the PA film. A rougher surface is expected to increase the effective water contact area during filtration, thus increasing membrane permeance. The quadratic relationship between roughness and pure water permeance of the PA-PCX membranes is shown in **Fig. 2.11b.** The results show an approximately linear relationship at the beginning of CNC incorporation. However, when the CNC suspension volume is further increased (PA-PC300), the rate of increase in water permeance is significantly reduced, indicating a certain limitation exists for PA-PC300.

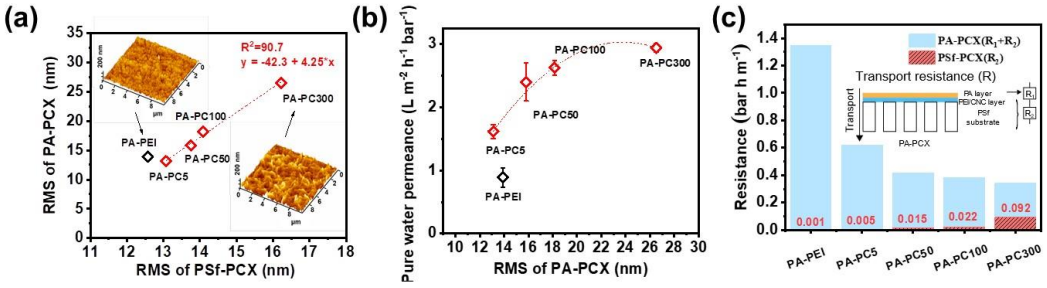

Fig. 2.11 (a) Linear relationship of the roughness between PSf-PCX and PA-PCX membranes; (b) quadratic relationship between the roughness and pure water permeance of PA-PCX membranes; and (c) schematic illustration and transport resistances value of PSf-PCX and PA-PCX membranes.

Therefore, changes in the corresponding transport resistances (reciprocal of the

permeance [143]) of different membranes were further explored. The transport resistances of the PA-PCX i-TFN membranes (R_0) consisted of the resistance from the PA layer (R_1) and the PSf or PSf-PCX (PSf substrate + PEI/CNC layer) substrate (R_2). The resistance of the PA film typically accounts for most of the total i-TFN membrane resistance (**Fig. 2.11c**). With an increase in the CNC content, the total resistance of the i-TFN membrane ($R_1 + R_2$) decreased significantly because of the higher permeability of the corresponding PA. When the CNC incorporation amount was further increased (PSf-PC300), a thicker intermediate layer was obtained (**Fig. 2.7**), resulting in a significant increase in the transport resistance of PSf-PC300 substrate (R_2) and a slower decrease in the resistance of the i-TFN membrane. Hence, the high resistance of the substrate in PSf-PC300 compromised the flux enhancement of the PA layer.

2.3.4 Chemical characteristics for substrate and i-TFN membranes

The salt rejection of nanofiltration membranes typically relies on the steric hindrance effect and Donnan exclusion theory [124]. The chemistry of both substrates and PA membranes was analyzed to determine the contribution of PEI/CNC to the selectivity of the resulting PA membrane. As shown in **Fig. 2.12a-b**, the surface chemical components are different for the different substrates and PA membranes, indicating that different substrate surfaces may affect the formation of PA membranes. With an increase in CNC incorporation, the PSf membrane surface is gradually covered by CNC, as evidenced by the increased O percentage and decreased S percentage (**Fig. 2.12b**, top) with a continuously increasing O/S ratio (**Fig. 2.12c**, top), where O and S are primarily attributed to CNC and PSf, respectively.

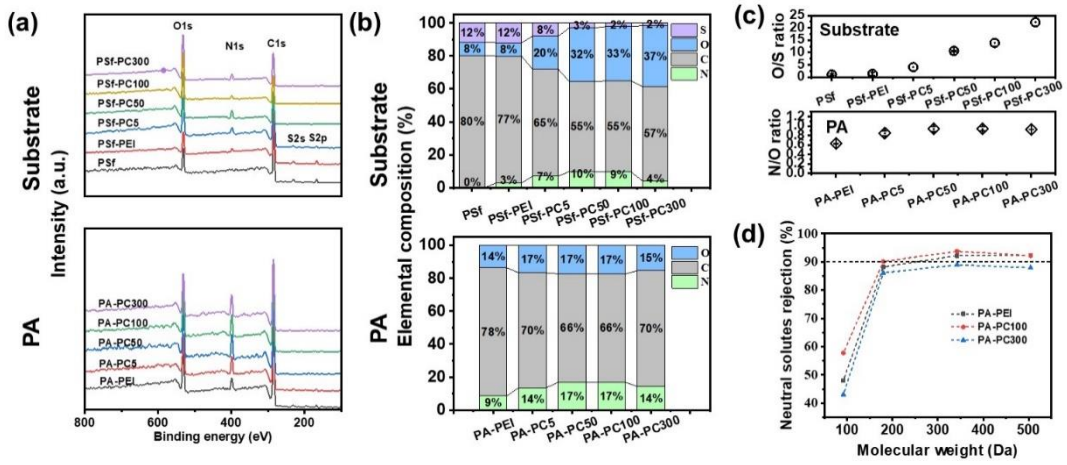

Fig. 2.12 (a) XPS profile and (b) element content of PSf-PCX and PA-PCX membranes; (c) O/S ratio to the PSf-PCX membrane and N/O ratio to the PA-PCX membranes; (d) MWCO of PA-PEI and PA-PCX membranes.

The uniform distribution of amine monomers at the aqueous–organic solvent interface promotes the formation of a dense PA film. The corresponding N content of PA initially increased and then decreased (**Fig. 2.12b**, bottom). When CNC was not used, a small amount of PEI molecules remained on the surface during filtration owing to the pore-penetration effect. The incorporation of CNC facilitated the formation of complex PEI molecules on the surface owing to their favorable attraction. For the elemental content changes of the PA layer, in addition to the O element from TMC hydrolysis, the presence of CNC might also contribute to the increase of the O element content. However, a gradually increased N/O ratio (**Fig. 2.12c**, bottom) of the PA layer was still observed after the introduction of CNC, indicating that the N element content increased. Considering that the N element was only derived from PEI, it further confirms that more amine monomers are enriched on the membrane surface. The improved PEI distribution by CNC complexation was favorable for crosslinking with TMC during the subsequent IP. However, if the CNC content is excessive, the exposure of PEI on the surface will be limited, resulting in a decrease in the amount of PEI accumulated on the top surface; thus, the N/O ratio of PA-PC membranes became relatively constant when the CNC content further increased. It is noted that the N

content for the PSf-PC300 membrane decreased to 4% and the N content of the PA-PC300 membrane also decreased (**Fig. 2.12b**), which could have led to the formation of loose regions in PA layer; thus, the membrane exhibited a slight decrease in $MgCl_2$ rejection (**Fig. 2.10b**). **Fig. 2.12d** shows the MWCO results of the PA-PEI, PA-PC100, and PA-PC300 membranes. The MWCO value of the PA-PC100 membrane was smaller than the pristine PA-PEI membrane, showing that a retained dense polymer network was formed for PA-PC100 membrane, which was caused by the more amine monomers enriched on the membrane surface. On the contrary, with excessive CNC incorporation, the resultant PA-PC300 membrane showed a relatively large MWCO value, which indicated the larger pore size of the membrane. Therefore, excessive CNC additives tended to form some loose regions in PA layer. The results further confirmed the change of the polymerized membrane network via the regulated amine monomer amount on the support surface by the CNC.

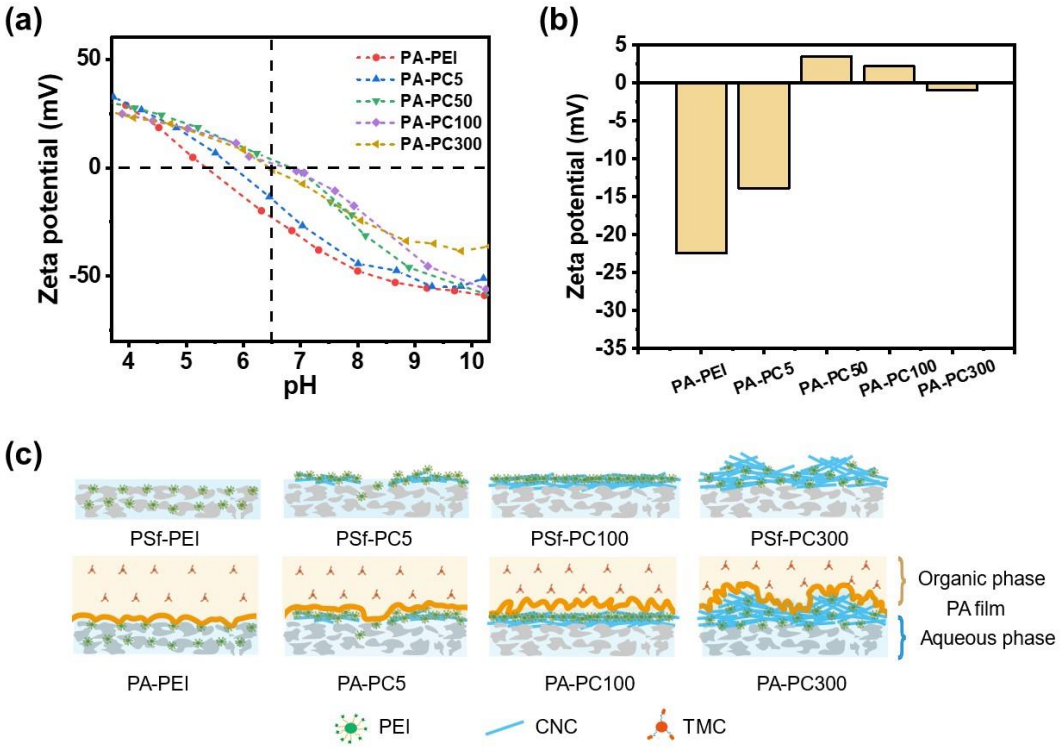

Fig. 2.13 Zeta potential of PA-PCX membranes at (a) different pH and (b) pH = 6.5; (c) schematic illustration of the IP of the PA membrane.

The zeta potential of the PA-PCX membranes (**Fig. 2.13a-b**) changed with the

incorporation of CNC. The enriched PEI distribution resulted in a more positive charge on the formed PA layer (from PA-PEI, PA-PC5, to PA-PC50), which might contribute to the Donnan repulsion of the cations. However, further increased CNC content on the top surface of the PA-PC300 membrane caused a slight decline in its zeta potential. The distribution change of PEI rendered by CNC for IP was illustrated in **Fig. 2.13c**. Different concentrations of CNC intermediate layers can affect the distribution of amine monomers, thereby affecting the formation of a dense PA layer. When the CNC partially covered the PSf substrate, the strong electrostatic interaction between CNC and PEI might cause the uneven local distribution of PEI monomer, resulting in certain loose regions in the generated PA layer. With more CNC incorporation, the CNC layer would fully cover the PSf substrate surface, and more PEI could be anchored on the surface to react with more TMC monomers, resulting in the formation of a dense PA layer. Further increasing the loading amount of CNC resulted in a slight decrease in the amount of PEI molecules on the surface to react with TMC, thus affecting the rejection effect of the membrane, which is consistent with the $MgCl_2$ rejection results in **Fig. 2.10b**. The above results indicate that the high salt rejection of the retentate can be attributed to the improved PEI distribution by complexation with CNC; thus, the formed PA membrane could have a well-crosslinked polymer network and a positive surface charge.

2.3.5 Salt rejection performance of optimal i-TFN membranes

The different salt rejections ($MgCl_2$, $MgSO_4$, NaCl, LiCl, and Na_2SO_4) were further investigated (**Fig. 2.14a** and **Table 2.3**), showing the order of $MgCl_2$ > $MgSO_4$ > NaCl > LiCl > Na_2SO_4, which is a result of combined effects of Donnan exclusion and steric hindrance. This result is also consistent with the typical positively charged membrane reported in other literature [98, 117, 153, 154]. For Donnan exclusion, Co-ions with high valence are preferentially rejected by the membrane. For instance, the valence ratio (Z^+/Z^-) of cation to anion for $MgCl_2$ is 2 ($Z^+ = 2$ for Mg^{2+} and $Z^- = 1$ for Cl^-), which is larger than other salts ($Z^+/Z^- = 1$ for $MgSO_4$, NaCl, and LiCl; $Z^+/Z^- = 0.5$ for Na_2SO_4). Therefore, $MgCl_2$ exhibited the highest rejection mainly due to the

Donnan exclusion effect. However, although $MgSO_4$, NaCl, and LiCl have the same Z^+/Z^- value of 1, their rejections are not similar. This should be attributed to the additional effect of steric hindrance, where the size of SO_4^{2-} is larger than Cl^- [114]. It is worth noting that though the zeta potential PA-PEI and PA-PC5 is negative at pH=6.5, they possessed the highest rejection for $MgCl_2$ rather than Na_2SO_4. This is because the negative charge density is likely not sufficient to completely change the order of salt rejections. Such phenomenon of the PEI-based PA membranes was also observed in other literature reports [155, 156]. Significantly, most i-TFN nanofiltration membranes had a relatively high rejection of more than 60% for these salts including LiCl and NaCl, indicating the existence of a steric hindrance effect.

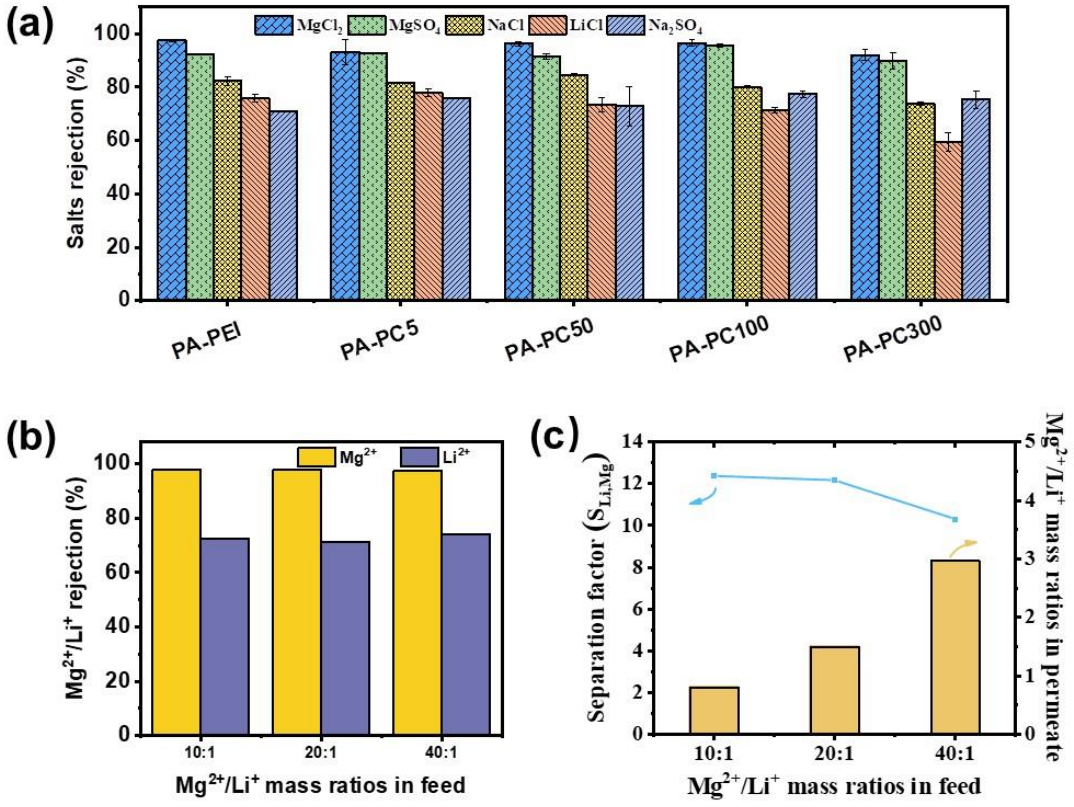

Fig. 2.14 Nanofiltration performance. (a) Separation performance of the PA-PCX membranes for different inorganic salts and (b) separation performance of the PA-PC100 membrane for a $MgCl_2$/LiCl mixture with different mass ratios; (c) Mg^{2+}/Li^+ mass ratio changes before and after filtration and separation factor of PA-PC100 membrane (salt concentration: 2000 ppm).

Table 2.3. Permeability and rejection of various inorganic salt solutions by PA-PC100 membranes.

Feed solution		Permeance ($L\ m^{-2}\ h^{-1}\ bar^{-1}$)	Rejection
Single salt	$MgCl_2$	1.93	97.3%
	$MgSO_4$	2.22	94.9%
	LiCl	1.90	69.9%
	NaCl	1.97	80.1%
	Na_2SO_4	2.40	76.1%
Multi salts ($MgCl_2$/ LiCl)	(Mg^{2+}/Li^+ mass ratio=10:1)	1.82	Mg^{2+}/Li^+ 97.8%/72.3%
	(Mg^{2+}/Li^+ mass ratio=20:1)	1.85	Mg^{2+}/Li^+ 97.6%/71.3%
	(Mg^{2+}/Li^+ mass ratio=40:1)	1.86	Mg^{2+}/Li^+ 97.5%/73.9%

Test conditions: Applied pressure: 10 bar; Concentration of single or multi salts feed solution: 2000 ppm.

Lithium metal has been widely applied in commercial fields and lithium resources are usually found in brines. However, salt-lake brines always have high Mg^{2+} content, which has a similar ionic hydration radius to Li^+ and makes it more difficult to separate them. Considering the high rejection of the $MgCl_2$ solution because of the Donnan exclusion effect between the membrane and Mg^{2+}, the positively charged nanofiltration membranes can be used to separate Mg^{2+}/Li^+ mixture solutions [17, 157]. Therefore, a PEI-based nanofiltration membrane with abundant positively charged amine groups is a preferred choice. The 2000 ppm Mg^{2+}/Li^+ mixture solution with different Mg^{2+}/Li^+ mass ratios (10:1, 20:1, and 40:1) was used to simulate salt-lake brine in different places (**Table 2.4**) to explore the Mg^{2+}/Li^+ separation performance of the PA-PC100 membranes. Mg^{2+} and Li^+ rejection was found almost independent of the Mg^{2+}/Li^+ ratio

(**Fig. 2.14b** and **Table 2.3**). After filtration, the mass ratio of Mg^{2+}/Li^{+} decreased from 10, 20, and 40 in the feed to 0.8, 1.5, and 3 in the permeate, respectively, and the corresponding selective separation factors were 12.36, 12.15, and 10.29, respectively (**Fig. 2.14c**). The separation factor decreases with an increase in the feed concentration because the concentration of the feed solution significantly influences the separation factor. Mg^{2+}/Li^{+} separation performance of some reported PEI-based and commercial nanofiltration membranes has been summarized in **Table 2.5**. Our PA-PC100 membrane exhibits competitive Mg^{2+}/Li^{+} separation performance among them.

Table 2.4. Mg^{2+} and Li^{+} concentrations (g/L) in main salt-lake brine globally.

Salt-lake brine	Country	Mg^{2+}	Li^{+}	Mg^{2+}/Li^{+} ratio	References
Maricunga	Chile	9.65	1.57	6.15	[158]
Atacama Salar					[159]
Brine	Chile	17.6	3.02	5.8	
Fox Greek	Canada	1	0.1	10	[160]
Smackover	USA	7.5	0.38	20	[160]
Bonneville	USA	4	0.057	70.17	[158]
Great Salt Lake	USA	8	0.06	133.33	[160]
West Taijinar	China	12.8	0.21	61	[29]
East Taijinar	China	29.9	0.85	35.02	[29]
Longmucuo	China	89.5	1.21	74	[161]
Uyuni	Bolivia	20	0.96	20.83	[29]

Table S5. Summary of Mg^{2+}/Li^{+} separation performance of polyamide membranes

Membrane type	Feed concentration (ppm)	Mg^{2+}/Li^{+} mass ratio	Separation factor	Permeance (L m^{-2} h^{-1} bar^{-1})	Pure water permeance (L m^{-2} h^{-1} bar^{-1})	Operation pressure (bar)	Ref
PA-PC100	2000	20	12.15		2.62	10	This work
PEI-TMC-EDTA			11.38		2.87	6	[162]
NF-90	2000	20	2.1			3	[89]
DAPP-TMC	2000	20	2.6		2.53	3	[89]
PEI-TMC	2000	20	20		5.02	8	[90]
BPEI-TMC-EDTA	2500	24	9.2	0.6		10	[163]
PEI/γ-CDs-TMC			10.80		4.86	4	[109]
PA-TG	2000	20	83	1.4		4	[164]
CNC-COOH/PEI-TMC	2000	30	12.15	4.17		8	[101]
CNC-COOH/PEI-TMC	2000	60	5.84	3.4		8	[101]
PEI-TMC/DAIB	25500	76.5	5.71	3.9		6	[116]

(Cross-flow nanofiltration mode)

2.4 Conclusions

In this study, amine monomers (PEI) and CNC were complexed via a one-step vacuum-assisted procedure, followed by IP with TMC, and i-TFN nanofiltration membranes were successfully fabricated. The strong electrostatic interaction between the CNC and PEI can limit the release and diffusion of the amine monomer during the IP process, resulting in the formation of a thinner PA film with a crumpled structure. The optimized membrane possessed a more effective permeable area of a continuous polymer network, substantially increasing water permeability without compromising salt rejection performance. This study provides a strategy to regulate the distribution of amine monomers at the interface of the interlayer for the design and fabrication of membranes with high separation performance.

Chapter 3

Ternary-coordination-regulated polyamide nanofiltration membranes for Mg^{2+}/Li^{+} separation

3.1. Introduction

With the widespread application of lithium-ion batteries in various fields, lithium has become a strategic resource. It is mainly stored in salt-lake brines, which account for over 70% of the total lithium reserves worldwide [116, 165]. To alleviate the shortage of lithium resources, lithium extraction from salt-lake brines has become the primary method of lithium production. Nevertheless, the presence of coexisting ions, particularly Mg^{2+}, significantly increases the difficulty of lithium extraction and restricts the development of the lithium industry. The similar hydration radius (Mg^{2+}(4.3 Å) vs. Li^{+} (3.8 Å)) and the high mass ratio are the two main challenges. Efficient Mg^{2+}/Li^{+} separation strategies are essential for Li recovery. Over the past decade, many methods have been employed for lithium extraction from salt-lake brines, including solvent extraction, evaporation, precipitation, adsorption, and nanofiltration (NF) membrane separation [1, 4]. Among them, owing to the low energy consumption and relatively high mono-divalent ion separation efficiency, the NF membranes exhibit enormous potential in Mg^{2+}/Li^{+} separation [4, 157].

In general, NF membranes composed of a polyamide selective layer, a microporous substrate, and nonwoven fabrics can segregate monovalent and divalent ions through Donnan exclusion and the size sieving effect [62]. Monovalent ions can pass through the NF membrane, while multivalent ions are captured. Thus, the NF membranes showed considerable advantages for Mg^{2+}/Li^{+} separation, particularly for positive NF membranes. Compared to Li^{+}, positive membranes usually show a stronger

exclusion effect on Mg^{2+} because they possess more charges [17]. However, commercial polyamide membranes are mainly fabricated by interfacial polymerization (IP) at the interface between an aqueous phase containing piperazine (PIP) and an organic phase containing trimesoyl chloride (TMC), but show unsatisfactory Mg^{2+}/Li^{+} selectivity because of the negative charges derived from the hydrolysis of acyl chloride groups [166]. Polyethyleneimine (PEI), which contains a large number of amino groups, is an excellent monomer for the fabrication of highly positively charged polyamide membranes owing to its large amount of unreacted amino groups [167]. However, pristine PEI-TMC membranes exhibit low water permeance and high Li^{+} rejection owing to their excessive crosslinking degree [118].

Various methods have been utilized to improve the permeance and ion selectivity of NF membranes, such as synthesizing new monomers, modifying or constructing an interlayer on the substrate, and incorporating various additives into the polyamide selective layer [168, 169]. Interactions (such as electrostatic interactions, hydrogen bonding, covalent bonding, and coordination interactions) between additives/interlayers and amino monomers play an important role in the IP process [170, 171]. For instance, an isotropic interlayer contributes to the uniform distribution and diffusion of amine monomers to adjust the IP kinetics and improve monovalent ion selectivity. Adding additives to the aqueous phase can also control the diffusion rate and interface concentration fluctuations of the amine monomers, thereby obtaining a polyamide film with a uniform pore size distribution [62]. Many materials [62] can be used, such as polymers (e.g., tannic acid (TA), polyvinyl alcohol (PVA), chitosan (CS), polydopamine (PDA), etc.), nanomaterials (e.g., halloysite nanotubes (HNTs), graphene oxide (GO), carbon nanotubes (CNT), metal–organic frameworks (MOFs), and covalent organic frameworks (COFs)), and salt additives (such as NaCl, $NaHCO_3$, $CuCl_2$, and ionic surfactants). Among these, salt additives have significant advantages such as low cost, environmental friendliness, and easy solubility [169]. Various transition metal ions (Co^{2+}, Cu^{2+}, Zn^{2+}, Ni^{2+}, Mn^{2+}, and Fe^{3+}) were incorporated into the aqueous phase, and the $-NH_2-M^{n+}$ coordination bonds formed between the transition

metal ions and amino groups (–NH_2) slowed the diffusion rate of the PEI monomer and influenced the IP process [127]. A much thinner polyamide layer (33 nm vs. 200 nm) was obtained. In addition, the strong coordination bonds severely reduce the activity of the amino groups, resulting in a less cross-linked polyamide membrane with a higher permeance. Meanwhile, a larger pore size can reduce the rejection of smaller, less-charged solutes. Therefore, the additive-assisted IP method is expected to provide Li^+ transport channels for Mg^{2+}/Li^+ efficient separation [172].

Natural polyphenolic materials with large amounts of pyrogallol and catechol groups are widely used for membrane modification [173]. These functional groups contribute to the formation of polyphenol-based coating and make it easily deposited onto different membranes via various physical and chemical interactions, including hydrophobic interaction, hydrogen bonds, electrostatic interaction, π–π stacking, polyphenol-metal coordination, and Michael addition/Schiff base reactions [174]. These interactions have also been widely used in the preparation of polyamide NF membranes, particularly in coordination interactions with metal ions [175, 176] and covalent/noncovalent effects with amino monomers [177-179]. Therefore, the introduction of natural polyphenolic materials can further enhance coordination interactions and optimize the IP process.

In this study, a polyphenol-metal-assisted method was employed, involving ternary coordination interactions among the monomers and additives of polyphenols and metal ions. Ternary interactions are expected to regulate the interfacial polymerization of the PEI monomer-based polyamide membranes, thereby improving their separation performance. Tannic acid (TA) was first deposited onto the substrate, followed by the impregnation of the Cu^{2+} ions-incorporated aqueous PEI monomer solution to establish ternary interactions among PEI, TA, and Cu^{2+} ions (**Fig. 3.1a**). The "anchor-capture" effect of TA caused more PEI to accumulate and uniformly distribute on the substrate surface, and this effect was further strengthened after the Cu^{2+} ions incorporation, which was expected to optimize the IP process and obtain a more positive charge on the formed polyamide layer. Based on the synergistic effect of the TA and

Cu^{2+} ions, a thinner, looser, and more positively charged PA-TA-Cu membrane was fabricated (**Fig. 3.1b**). It exhibits high water permeance, high Mg^{2+} rejection, and low Li^{+} rejection.

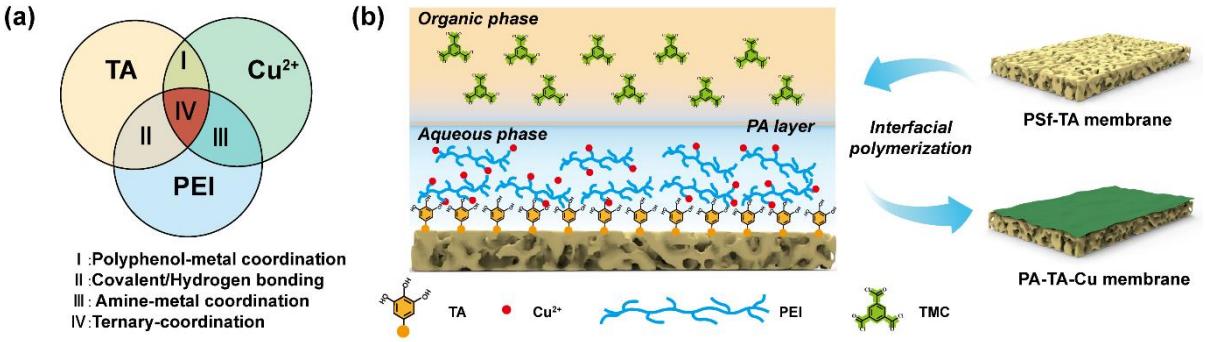

Fig. 3.1 (a) Ternary coordination between TA, PEI, and Cu^{2+} ions; (b) Schematic of the interfacial polymerization on TA-modified substrate (PSf-TA membrane) based on the polyphenol-metal-assisted method.

3.2. Experimental

3.2.1. Materials and chemicals

TA and PEI (molecular weights: 600, 1800, and 10000 Da), were purchased from Sigma-Aldrich (St. Louis, MO, US). The copper chloride dihydrate ($CuCl_2$ $2H_2O$). Other chemicals used in this chapter were the same as that in Chapter 2.

3.2.2. Pretreatment of substrate membranes

The commercial PSf ultrafiltration membrane was immersed in a TA solution (2 g/L) for 24 h to adsorb enough TA molecules on the membrane surface. The fabricated membranes were then transferred to DI water to remove unstable TA molecules from the membrane surface. The TA-modified PSf membrane was denoted as PSf-TA.

3.2.3. Fabrication of different NF membranes

The polyamide selective film was fabricated by an IP reaction on PSf and PSf-TA substrates. In brief, 0.5 g of PEI was dissolved in 100 mL water to obtain an aqueous solution, and 0.15 g TMC was dissolved in 100 g n-hexane to obtain an organic solution.

The substrate (diameter: 50 mm) was fixed in a polytetrafluoroethylene frame and immersed in the prepared aqueous solution for 5 min, after which the excess aqueous solution was removed using an air knife. Subsequently, the membrane was immersed into the organic phase solution for another 3 minutes, and heated in an oven at 70 ℃ for 10 minutes after removing the organic solution. Finally, all the resulting membrane was stored in DI water at 4 ℃ until the test. The prepared NF membranes were named PA and PA-TA according to the substrates (PSf or PSf-TA).

In addition, 0.02 g $CuCl_2 \cdot 6H_2O$ was added into 100 mL PEI aqueous solution, and the polyamide films were also fabricated on the PSf and PSf-TA substrates, according to the same IP procedure. The resulting membranes were named PA-Cu and PA-TA-Cu. The molecular weight of the PEI used during the IP process was 1800 Da unless otherwise specified, even though other PEIs of different molecular weights were also used in this experiment. The specific fabrication processes for different NF membranes are shown in **Fig. 3.2.**

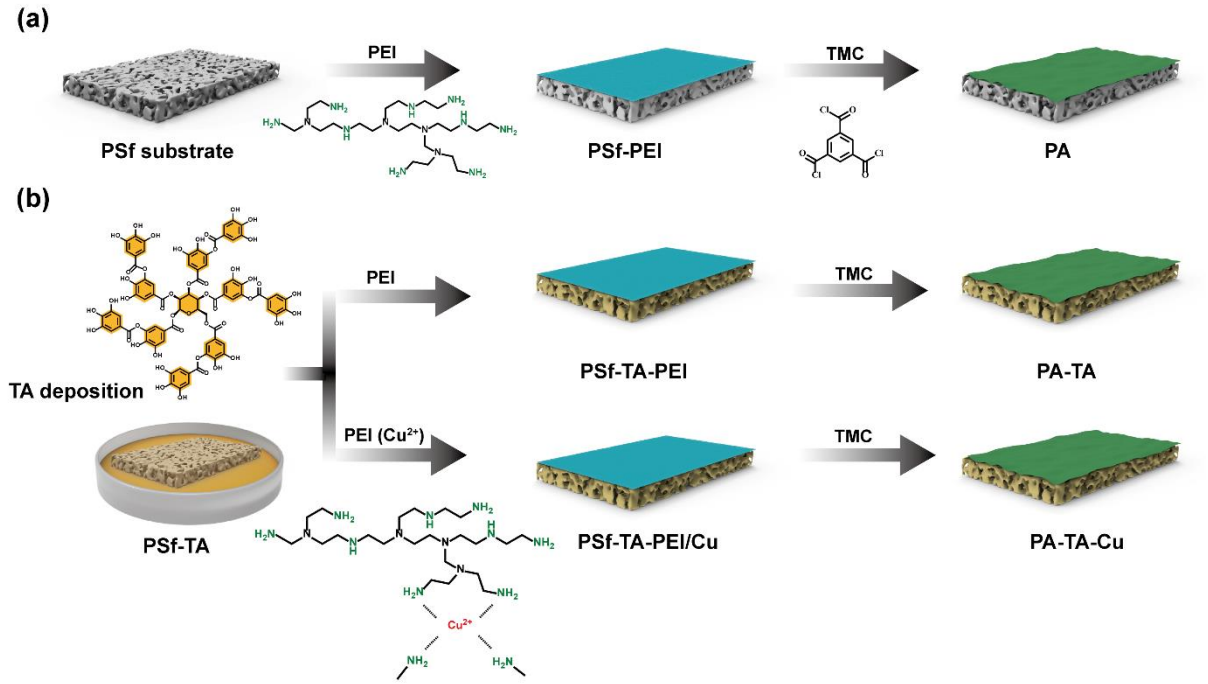

Fig. 3.2 Schematic of the fabrication process for the (a) PA; (b) PA–TA; and (c)PA-TA-Cu NF membranes.

3.2.4. Characterization

Transmission electron microscopy (TEM; Ultramicrotome, Leica EM UC7, Germany) was used to obtain cross-sectional images and determine the thickness of the polyamide membrane. Before the TEM measurements, all membranes were fixed in resin and cut into thin slices with a thickness of 100 nm using a microtome (Ultramicrotome, Leica EM UC7, Germany). Other characterization methods were the same as in Chapter 2.

3.2.5. Performance evaluation of NF membrane

The separation performance of the fabricated NF membrane was tested using a cross-flow filtration setup (effective filtration area: 7.02 cm^2, flow rate: 9.9 mL min^{-1}). The calculation methods of water permanence, salt rejection, and Mg^{2+}/Li^{+} mixture separation performance were stated in Chapter 2.

3.2.5. Evaluation of molecular weight cut-off (MWCO)

Glycerol (92 Da), D-(+)-glucose (180 Da), sucrose (342 Da), and D-(+)-raffinose pentahydrate (504 Da) (1000 ppm) were used as feed solutions to evaluate the MWCO of the fabricated NF membranes. A total organic carbon analyzer (TOC-VCSN, Shimadzu Co., Japan) was used to determine the concentrations of the feed and permeate solutions, which were then used to calculate the rejection of these sugars.

The corresponding pore size distribution can be expressed by a probability density function based on the premise that there are no steric or hydrodynamic interactions between these neutral solutes and the membrane pores. It is calculated as follows [180]:

$$\frac{\mathrm{d}R(d_p)}{\mathrm{d}d_p} = \frac{1}{r_p \ln\sigma_p \sqrt{2\pi}} exp\left[-\frac{\left(\ln d_p - \ln\mu_p\right)^2}{2\left(\ln\sigma_p\right)^2}\right], \tag{3.4}$$

where d_p represents the Stokes diameter of the neutral molecules, σ_p represents the geometric standard deviation of the probability density function curve, and μ_p represents the mean pore size, which is equal to the d_p of the neutral solute with a

rejection of 50%. σ_p represents the distribution of the membrane pore size, which is the ratio of d_p of the neutral molecule with a rejection of 84.13% to that of 50%. The d_p values of neutral solutes were calculated as follows:

$$\log\frac{d_p}{2} = -1.4962 + 0.4654\text{logM}. \tag{3.5}$$

3.3. Results and discussion

3.3.1. PEI monomer loading using ternary interactions

The interactions and stabilities of mixed solutions among each two of the TA, PEI, and Cu^{2+} ions were observed. As shown in **Fig. 3.3a**, all the single solutions were transparent. When the TA and PEI solutions were mixed, white flocculation occurred immediately and the solution turned dark brown after 24 h. This phenomenon reveals strong electrostatic or hydrogen-bonding interactions between TA and PEI. The TA/$CuCl_2$ mixed solution was light yellow, and a precipitate emerged at the bottom after 24 h, confirming the coordination interaction and formation of the TA–Cu^{2+} complex. Unlike the TA/PEI and TA/$CuCl_2$ solutions, the PEI/$CuCl_2$ solution was stable and no precipitation occurred, which is consistent with the phenomenon reported in the literature [127, 181]. **Fig. 3.1a and Fig. 3.3b** illustrate the ternary interactions involving PEI, TA, and Cu^{2+} ions. These interactions encompass polyphenol-metal coordination, amine-metal coordination, covalent/hydrogen bonding, and electrostatic interaction. Particularly noteworthy is that TA can undergo reactions with PEI via Michael addition and Schiff base reaction (covalent reactions), resulting in a color change in the mixed solution over time (**Fig. 3.3a**). The strong interaction between TA and PEI also indicates that, unlike other common aqueous monomers (such as piperazine, PIP [177, 178] and M-phenylenediamine, MPD [182]), TA cannot be used as an additive in the PEI aqueous solution. Thus, TA was pre-deposited onto the PSf substrate, and Cu^{2+} ions were added to the PEI solution as an aqueous phase during the IP process to establish ternary interactions among these species.

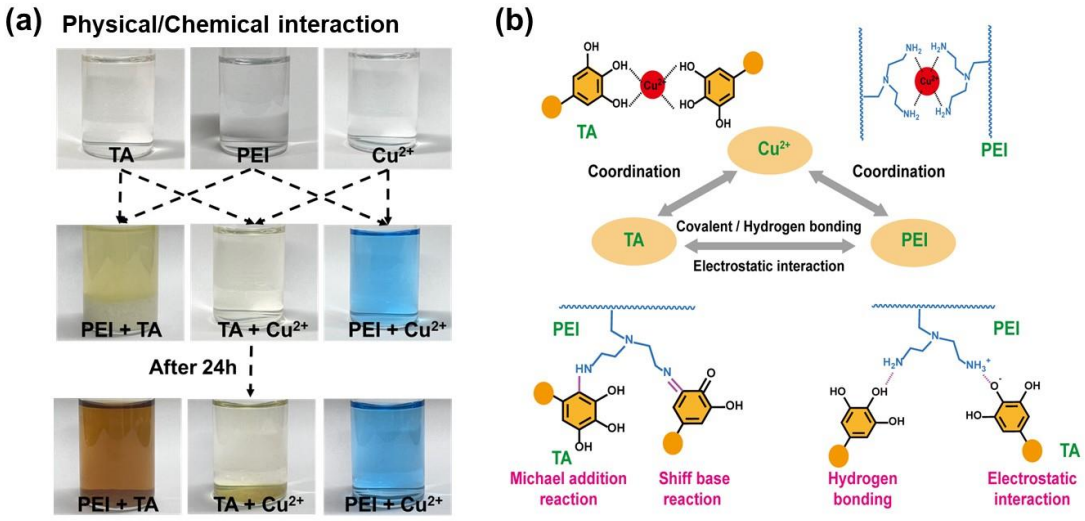

Fig. 3.3 (a) Signal and mixed solution images of TA, PEI, and $CuCl_2$ (the concentrations are consistent with those in the subsequent IP process); (b) Schematic of interactions between TA, PEI, and Cu^{2+} ions.

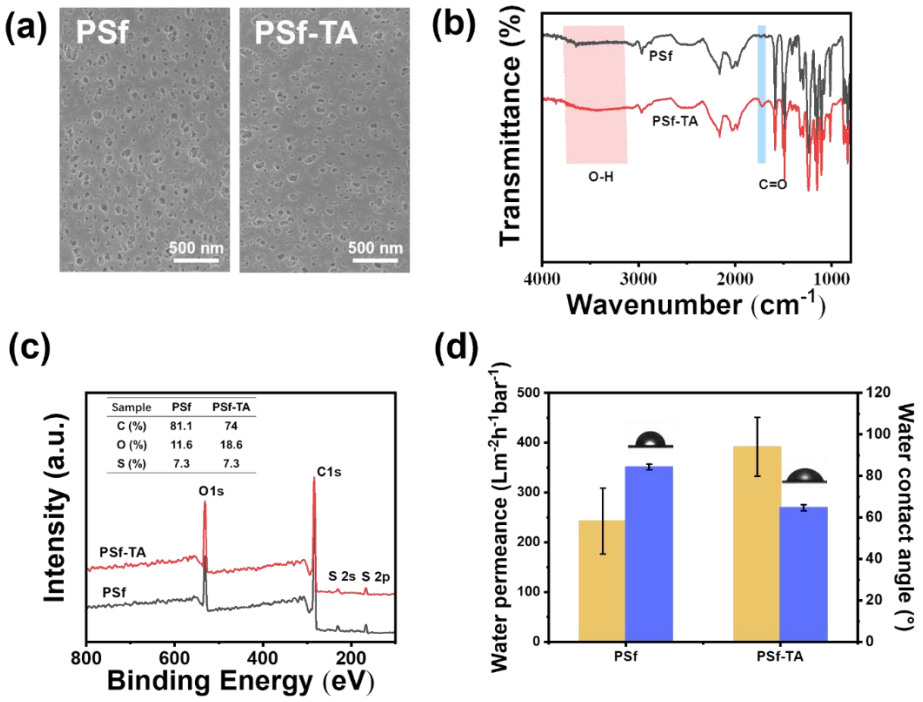

Fig. 3.4 (a) SEM images, (b) ATR-FTIR, (c) XPS spectra, and (d) water permeance and contact angle of PSf and PSf-TA membranes.

TA can be easily deposited on different membranes via various physical and chemical interactions. The microscopic morphologies of the membranes were

examined using SEM, and the images are presented in **Fig. 3.4a**. No notable changes were observed before or after TA modification. Therefore, the surface chemical structures of the pristine and modified membranes were further analyzed using ATR-FTIR and XPS. The wide peak in the range of 3825–3335 cm^{-1} is associated with the O–H stretching vibration, which originates from TA (**Fig. 3.4b**). As shown in **Fig. 3.4c**, the O1s absorption peak of the PSf–TA membrane increased, and the corresponding composition increased from 11.6% to 18.6%. After TA modification, the water permeance of the PSf-TA membranes increased, whereas the water contact angles decreased (**Fig. 3.4d**). All the results indicated that TA successfully coated the surface of the PSf membranes.

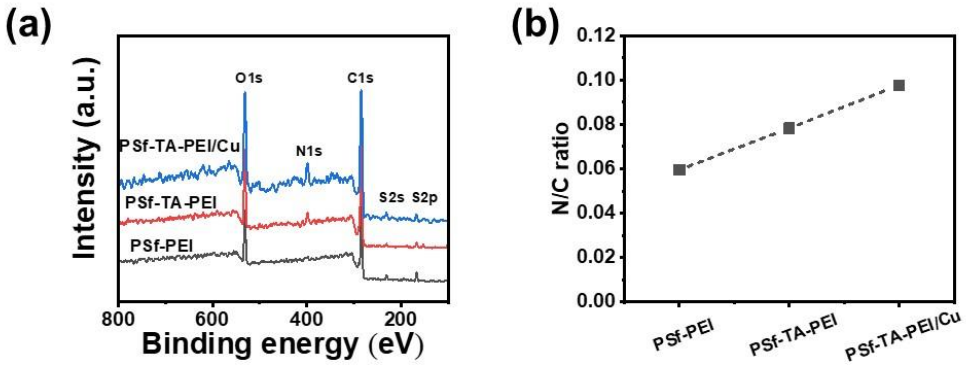

Fig. 3.5 (a) XPS spectra and (b) N/C ratio of the PSf–PEI, PSf–TA–PEI, and PSf–TA–PEI/Cu membranes.

Table 3.1 Elemental contents of PSf-PEI, PSf-TA-PEI, and PSf-TA-PEI/Cu membranes.

Membrane type	C	N	O	S	Cu	N/C
PSf-PEI	78.9	4.7	12.6	3.8		0.060
PSf-TA-PEI	74.1	5.8	16.8	3.3		0.078
PSf-TA-Cu-PEI	75.6	7.1	14.0	3	0.33	0.094

PEI loading on the substrate is important for the subsequent IP processes. Successful TA deposition on the PSf substrate (**Fig. 3.4**) was expected to anchor more

PEI on the surface to participate in the IP reaction. To further explore the "anchor-capture" effect of TA, after the aqueous phase solutions were poured onto the different substrates (**Fig. 3.2**), XPS was used to investigate the changes in the elemental compositions of the PSf–PEI, PSf–TA–PEI, and PSf–TA–PEI/Cu membranes (**Fig. 3.5** and **Table 3.1**). The results indicate that the S element content generated by the PSf substrate significantly decreased after aqueous phase covering on the substrate surface, compared to both the PSf and PSf-TA substrate (**Fig. 3.4c**). Meanwhile, compared to the initial PSf-PEI membrane, the elemental ratio of nitrogen to carbon (N/C) increased significantly with TA pre-deposition, which demonstrated that more PEI was anchored on the modified PSf substrate, owing to the N being only derived from PEI. In addition, after the Cu^{2+} ions were incorporated into the PEI aqueous solution, the "anchor–capture" effect of TA was further strengthened as a higher N/C ratio was observed from the surface of PSf–TA–PEI/Cu.

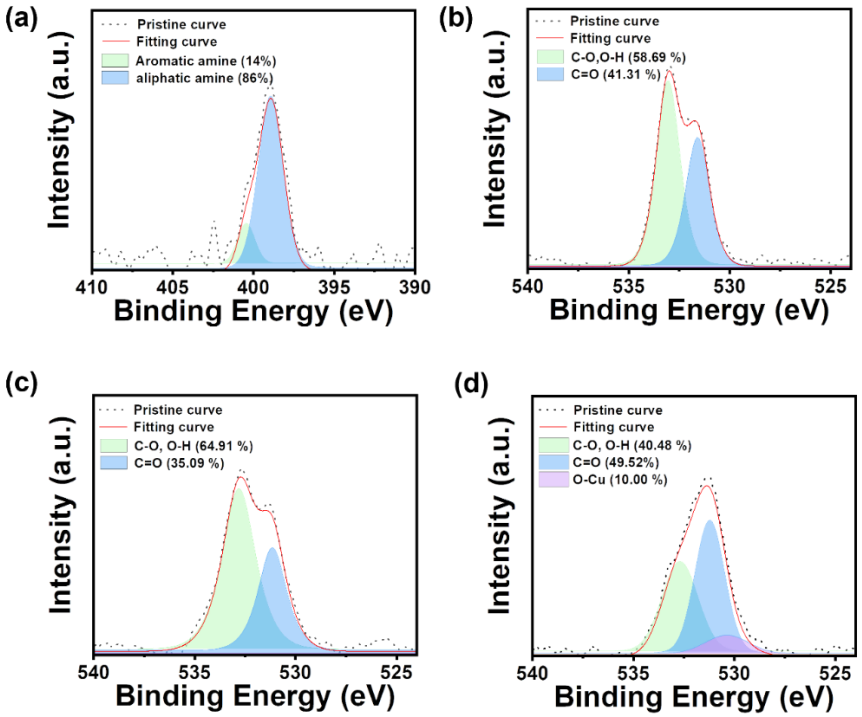

Fig. 3.6 (a) N 1s spectra of PSf-TA-PEI membrane; O 1s XPS spectra of (b) PSf-TA, (c) PSf-TA-PEI, and (d) PSf-TA-PEI/Cu membranes.

The deconvolution analysis of XPS spectra of PSf-TA, PSf-TA-PEI, and PSf-TA-PEI/Cu membranes further confirms the ternary coordination interactions among TA, PEI, and Cu^{2+} (**Fig. 3.6**). The N 1s spectrum analysis is presented in the **Fig. 3.6a**. It can be found that the N 1s spectrum is composed of two peaks at 400.4 eV and 398.9 eV, corresponding to the aromatic amine-type nitrogen and the aliphatic amine-type nitrogen [183, 184]. The peak attributed to aromatic amine-type nitrogen originates from the C-N bond on the benzyl ring of TA, indicating the successful cross-linking (Michael addition reaction) between TA and PEI. The chemical bonds associated with the O atoms in PSf-TA and PSf-TA-PEI membranes exhibited two peaks (**Fig. 3.6b-c**), representing typical C–O and C=O, which originating from the phenolic hydroxyl and carboxyl groups of TA. The coordination interaction between the oxygen atoms and Cu^{2+} can be confirmed by the new peak at 531.04 eV in the spectrum of the PSf-TA-PEI/Cu (**Fig. 3.6d**) [185, 186]. All these results confirm the ternary coordination interactions among TA, PEI, and Cu^{2+}. The $–NH_2–Cu^{2+}$ coordination bonds promoted the formation of PEI–Cu complexes, which caused more PEI to accumulate on the membrane surface. **Fig. 3.7** shows a schematic of the TA capture behavior of PEI and Cu^{2+} ions, contributing to the uniform PEI deposition, which is beneficial for the preparation of defect-free and highly positively charged NF membranes.

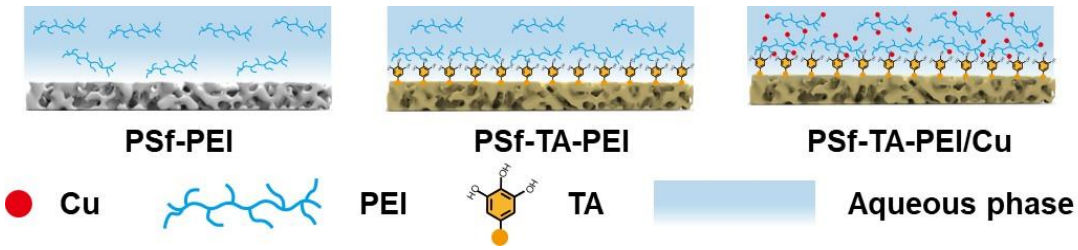

Fig. 3.7 Schematic of the "anchor–capture" effect of the polyphenol-metal assisted method.

3.3.2. Membrane characterization and performance

Fig. 3.8a shows the SEM and AFM images of the PA, PA–TA, and PA–TA–Cu membranes. All PEI–TMC polyamide films showed smooth and dense surface

morphologies with very low root-mean-square roughness (RMS). Notably, the surface roughness of the PA–TA membrane (10.66 nm) was slightly higher than those of the PA (6.33 nm) and PA–TA–Cu (7.87 nm) membranes, which aligns with the fewer ring-like groove structures observed in SEM image. The strong electrostatic and hydrogen-bonding interactions led to PEI enrichment around the TA molecules, creating an unstable reaction interface and resulting in rough volcano structure structures [105]. The incorporation of Cu^{2+} ions resulted in a smoother surface due to the slowed diffusion speed of PEI into the organic phase, caused by the stronger "anchor–capture" effect of ternary interactions [117, 187].

The elemental compositions of the NF membranes are shown in **Fig. 3.8b-c**, the increased N elemental content and N/C ratio were still observed, which further confirmed the strong "anchor–capture" effect for PEI monomer loading on the substrate using the polyphenol–metal-assisted method.

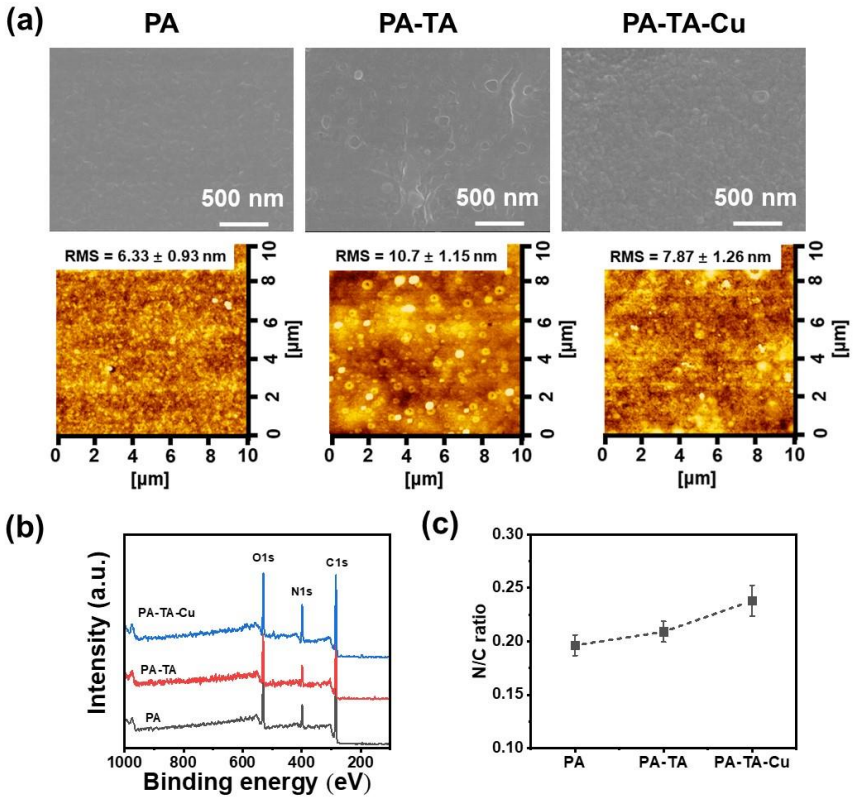

Fig. 3.8 (a) SEM and AFM images; (b) XPS profiles; and (c) N/C ratios of the PA, PA–TA, and PA–TA–Cu membranes.

The pure water permeance (**Fig. 3.9a**) along with the $MgCl_2$ and LiCl salt rejection (**Fig. 3.9b**) were tested to evaluate the filtration performance of PA, PA–TA, and PA–TA–Cu membranes, and the corresponding pure water permeance is 0.41, 3.40, and 4.87 L m^{-2} h^{-1} bar^{-1}, respectively. Furthermore, the rejection rates of $MgCl_2$ increased from 92.2% to 95.0% and 95.9%, respectively, whereas those of LiCl decreased from 73.0% to 30.3% and 17.1%, respectively. Moreover, the rejection difference between $MgCl_2$ and LiCl increased from 19.2% to 64.7% and 78.8%, respectively. Because the purpose of Mg^{2+}/Li^+ separation is to extract Li^+ from a Mg^{2+}/Li^+ mixture, higher Mg^{2+} rejection and lower Li^+ rejection are desirable. These results demonstrate that the PA–TA–Cu membrane could show significant potential for Mg^{2+}/Li^+ separation.

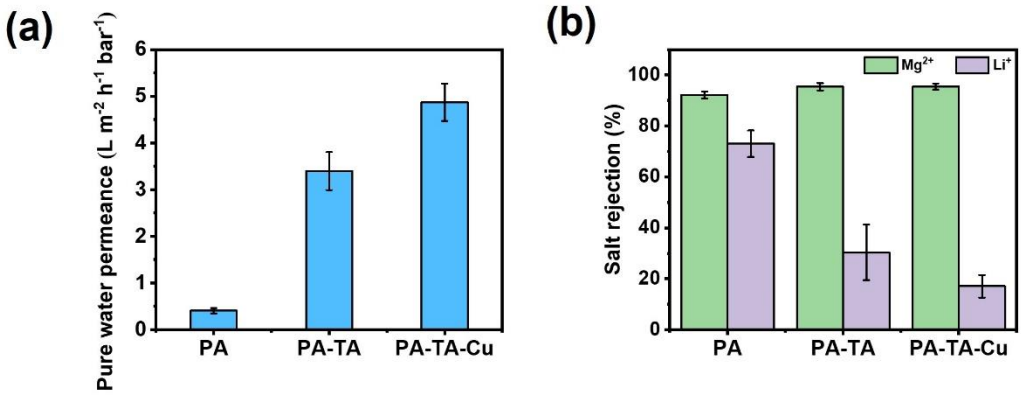

Fig. 3.9 (a) Pure water permeance; (b) $MgCl_2$ and LiCl salt rejection performance of the PA, PA–TA, and PA–TA–Cu membranes. The salt concentrations used are 2000 ppm.

NF membranes fabricated using different $CuCl_2$ concentrations were also tested. As shown in **Fig. 3.10**, the pure water permeance significantly increased with higher $CuCl_2$ concentration, while maintaining high rejection of $MgCl_2$ salt. Unless specified otherwise, the membrane referred to as PA-TA-Cu in this paper is the PA-TA-Cu0.02% membrane. The PEI monomers with different molecular weights (MW=600, 1800, and 10000 Da) were also adjusted (**Fig. 3.11**), and the performance similarly improved after TA deposition and Cu^{2+} incorporation, further confirming the benefits of the polyphenol-metal-assisted method.

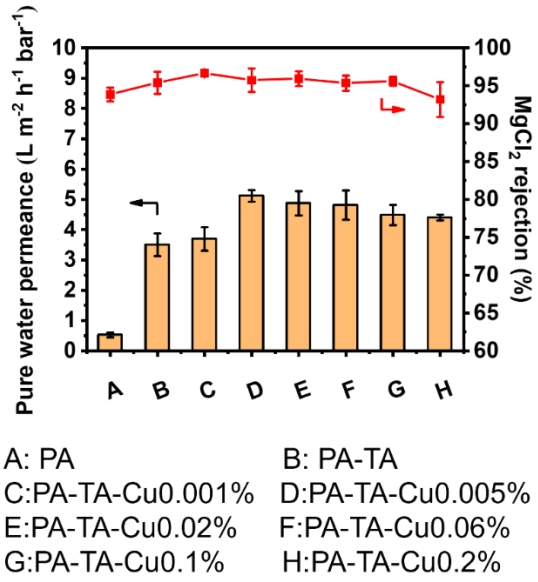

Fig. 3.10 Pure water permeance and $MgCl_2$ salt rejection performance of the PA, PA–TA, and PA–TA–CuX membranes. X represents the concentration (w/w %) of $CuCl_2$ in aqueous solution.

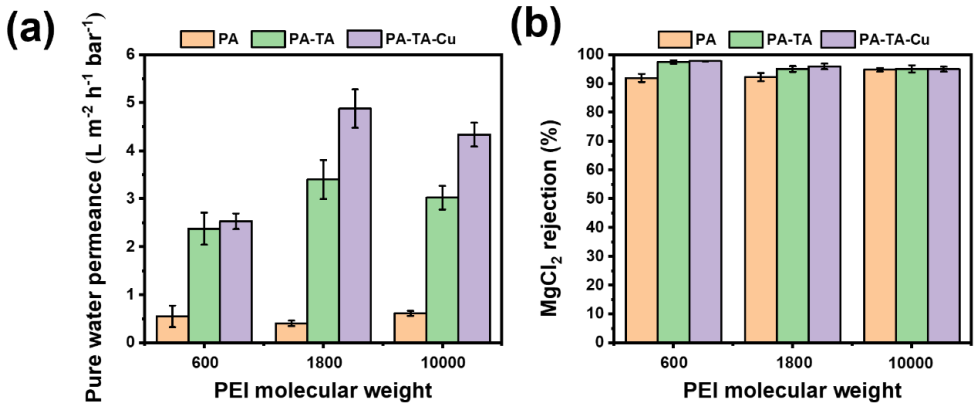

Fig. 3.11 (a) Pure water permeance and (b) $MgCl_2$ rejection of NF membranes fabricated using PEI monomers with different molecular weights (MW=600, 1800, and 10000 Da).

The enhanced permeance of polyamide membranes is generally ascribed to their enlarged surface area, thickness, and looser membrane structures. Although the surfaces of these membranes exhibited similar morphologies and roughness (**Fig. 3.8a**), the

differences in the thickness and pore size of the polyamide layer were further explored. As shown in **Fig. 3.12a-c**, TEM was used to determine the thicknesses of the PA, PA–TA, and PA–TA–Cu membranes. The PA–TA–Cu membrane displayed a much thinner polyamide selective layer (~11 nm) than the pristine PA (~37 nm) and PA–TA membranes (~17 nm). The formation of an ultrathin polyamide active layer on the PSf–TA substrates was attributed to the enrichment of PEI on the PSf–TA substrates, which accelerated the self-termination of the IP process [77, 142]. Furthermore, the various interactions between TA, PEI, and Cu^{2+} ions inhibited the diffusion of PEI into the organic phase, which also facilitated the formation of a thinner selective layer. Notably, the PA–TA–Cu membrane possesses almost the thinnest positively charged selective layer [77], which significantly reduces the transport resistance, thus resulting in a significant enhancement in water permeance (**Fig. 3.9a**). The results further confirmed that the synergistic effect of TA and Cu^{2+} ions was beneficial for the preparation of ultrathin polyamide films.

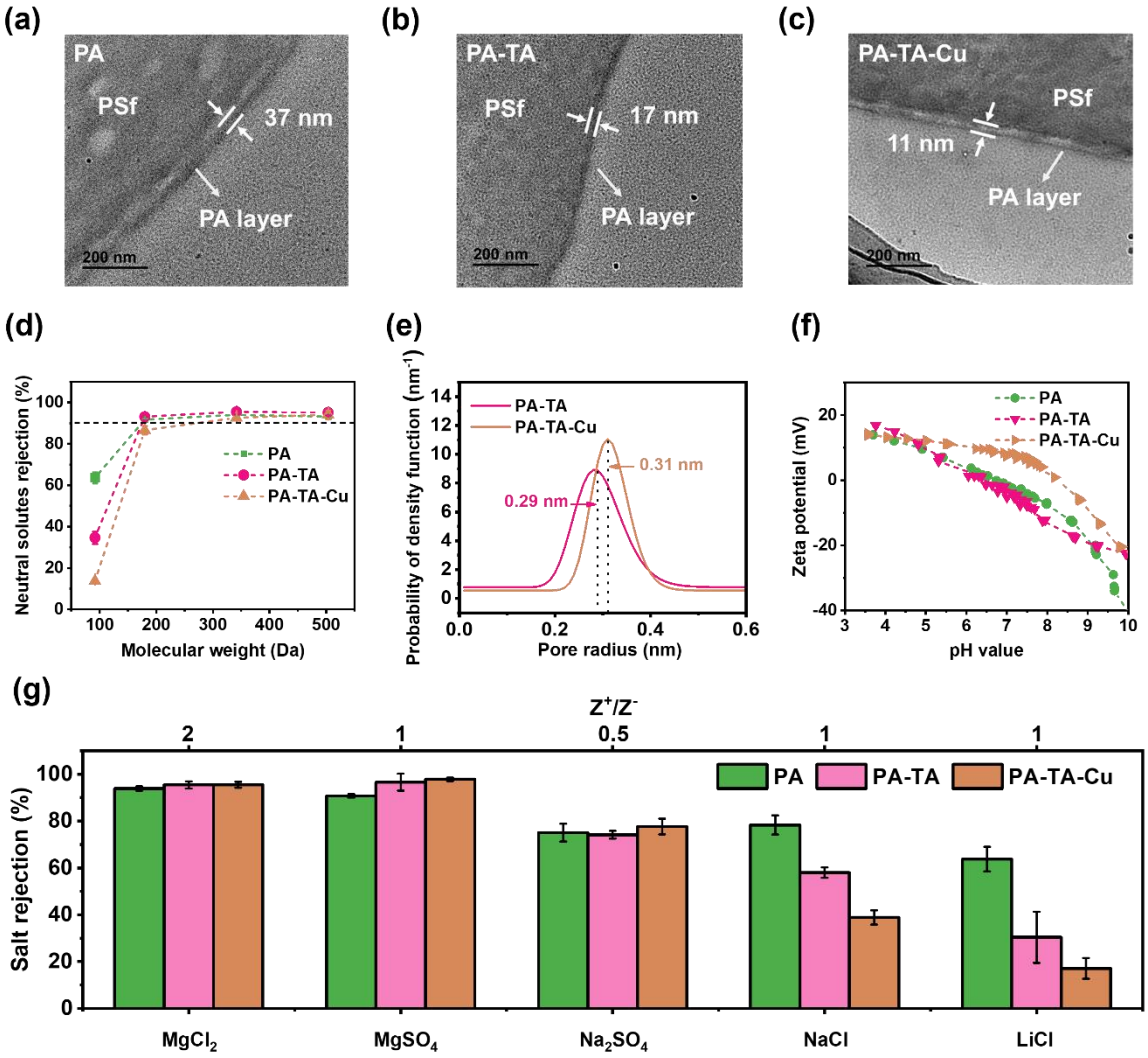

Fig. 3.12 (a–c) Cross-sectional TEM images, (d) MWCO, (e) pore size distribution, and (f) Zeta potential of PA, PA–TA, and PA–TA–Cu membranes; (g) separation performance of the PA-TA–Cu membrane for different inorganic salts. The salt concentrations used are 2000 ppm.

The MWCO test using four neutral carbohydrates (glycerol, glucose, sucrose, and raffinose) of various molecular weights (92, 180, 342, and 504 Da) was used to investigate the effect of the polyphenol–metal-assisted method on the pore size of the resultant polyamide membrane (**Fig. 3.12d**). Compared to the initial PA membrane, the PA–TA membranes showed a loose structure, with a sharper MWCO between the molecular weights of 92 Da (glycerol) and 180 Da (glucose). This may be attributed to

the uniform distribution and retarded diffusion of PEI on the substrate for the IP to form a more uniform pore structure. The TA layer on the PSf substrate enhances the capture and enrichment of amine monomers, promoting uniform stacking of PEI monomers on the membrane surface [136]. The even distribution of PEI benefits its diffusion into the organic phase during the IP process, leading to a polyamide active layer with more uniform pores [71]. In addition, the hindrance of PEI diffusion to the organic phase (caused by the "anchor–capture" effect of TA) limited the amount of PEI that could diffuse to the organic and react with TMC during the IP process [188], leading to a looser polymer network [189-191]. Furthermore, the highly hydrophilic PSf–TA substrate (**Fig. 3.4d**) can adsorb many water molecules, leading to the partial hydrolysis of acyl chloride and interrupting the IP process [142]. Therefore, a looser but more homogeneous polyamide selective layer (with more uniform pores) is formed in the case of PA–TA. When the Cu^{2+} ions were incorporated into the aqueous, the $–NH_2–Cu^{2+}$ coordination bonds severely reduced the activity of the amino groups, resulting in the reduced crosslinked polyamide film in their vicinity [127], thereby the resultant PA–TA–Cu exhibited enlarged mean pore radius (0.31 nm) and narrow pore size distribution (σ_p = 1.13) than that of PA–TA membranes (mean pore radius = 0.29 nm and σ_p =1.19) (**Fig. 3.12e**). The loose structure endows the PA–TA–Cu membranes with exclusive Li^+ transport channels, which explains the lower rejection of the LiCl solution (**Fig. 3.9b**). In addition, the formation of a loose polyamide network via the regulated IP process is another factor contributing to the higher permeance.

The surface charge of the polyamide NF membranes is important to render rejection towards high-valence ions. The Zeta potentials of pristine PA, PA–TA, and PA–TA–Cu membrane surfaces were determined at different pH values. As shown in **Fig. 3.12f**, all the membranes were positively charged under the test conditions (pH 6.5), which might be due to the protonation of the unreacted amino groups from PEI. The "anchor–capture" effect of TA caused more PEI to accumulate on the substrate surface, which might result in a more positive charge on the formed polyamide layer. However, the Zeta potential of the PA–TA membrane is similar to that of the initial PA

membrane. A key reason for this is that the Michael addition/Schiff base reactions between TA and PEI consume a certain number of amino groups. With the incorporation of Cu^{2+} ions, Cu^{2+} can serve as a positively charged center [192], which further improves the positive charge of the PA–TA–Cu membrane. The amount of Cu^{2+} ions loaded onto the resulting PA–TA–Cu membrane was further explored. Briefly, the PA–TA–Cu membrane was immersed in 1% HNO_3 (30 min) solution to elute the bound Cu^{2+} ions, and the Cu^{2+} concentration of the solution, measured by ICP, was used to calculate the Cu^{2+} loading amount of the membrane (1.62 μg/cm^2**)**. According to the Donnan exclusion theory [124], highly positively charged membranes usually exhibit stronger repulsion towards cations (Mg^{2+}), which is why even though the PA–TA–Cu membrane has a relatively loose structure, it still has a high rejection of Mg^{2+} ions (**Fig. 3.9b**).

Fig. 3.12g shows the rejection performances of the PA–TA–Cu membrane for different salts ($MgCl_2$, $MgSO_4$, Na_2SO_4, NaCl, and LiCl). The rejection order ($MgCl_2$ ≈ $MgSO_4$ > Na_2SO_4 > NaCl > LiCl) follows the law of a typical positively charged NF membrane [108], which is based on the combined effects of Donnan exclusion and steric hindrance. The positively charged PA–TA–Cu membrane exhibited strong electrostatic repulsion with positive cations, thus showing a high rejection of salts with a larger valence ratio (Z^+/Z^-). Among these salts, $MgCl_2$ has the highest valence ratio (Z^+/Z^- = 2 for $MgCl_2$; Z^+/Z^- = 1 for $MgSO_4$, NaCl, and LiCl; Z^+/Z^- = 0.5 for Na_2SO_4), and $MgCl_2$ exhibited the higher rejection in the experimental results, indicating that the Donnon exclusion effect plays the most important role. Notably, although the Z^+/Z^- values of $MgSO_4$, NaCl, and LiCl are the same (Z^+/Z^- = 1), their rejections are different. Thus, steric hindrance effects must be considered (Mg^{2+}(8.6 Å) > SO_4^{2-} (7.6 Å) > Na^+ (7.2 Å) > Cl^- (6.6 Å), and the size of SO_4^{2-} is larger than Cl^-, which can explain why the $MgSO_4$ exhibits the higher rejection. The highly uniform pore size distribution also contributes to the extremely high rejection of larger divalent salts (**Fig. 3.12e**). The moderate rejection of Na_2SO_4 (with the lowest Z^+/Z^- value, Z^+/Z^- = 0.5) further confirms that the salt rejection is the cooperative result of the Donnan exclusion and size sieving

effect.

3.3.3. Mg^{2+}/Li^{+} separation performance

The Mg^{2+}/Li^{+} separation performance of the fabricated NF membranes was further investigated using $MgCl_2$/LiCl mixture solutions (total salt concentration of 2000 ppm) with different Mg^{2+}/Li^{+} ratios (10:1, 20:1, and 40:1) as simulated brine-lake solutions. As shown in **Fig. 3.13a–b**, for the same NF membrane, the Mg^{2+}/Li^{+} separation performance was nearly independent of the Mg^{2+}/Li^{+} ratio. Among the different NF membranes, the PA–TA–Cu membrane exhibited the highest permeance and rejection difference between Mg^{2+} and Li^{+} ions, which showed a similar trend when using a single salt solution as the feed solution (**Fig. 3.9**), further confirming the benefits of the polyphenol–metal-assisted method to fabricate desirable Mg^{2+}/Li^{+} separation NF membranes (**Fig. 3.13c**). Notably, due to the high osmotic pressure in the $MgCl_2$/LiCl mixture solution, the effective driving force is reduced, leading to lower water permeance compared to pure water (**Fig. 3.9a)**.

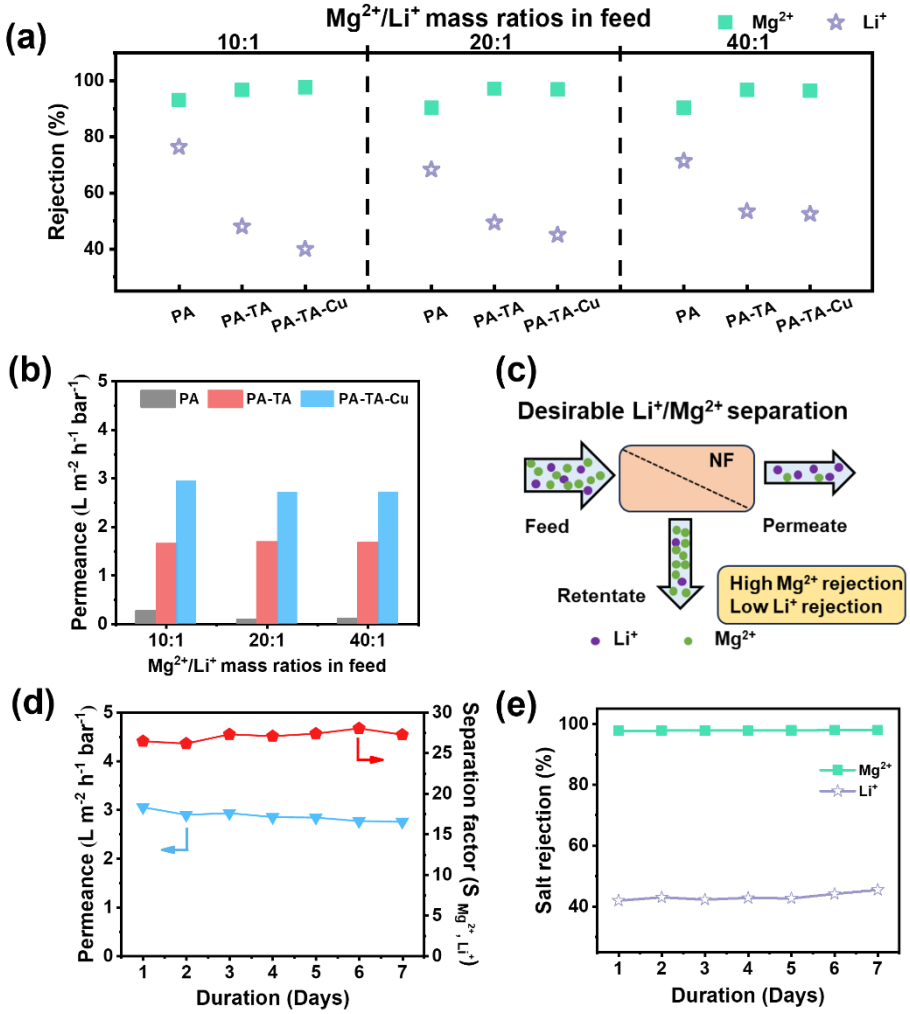

Fig. 3.13 (a) The rejection and (b) permeance of the PA, PA–TA, and PA–TA–Cu membranes for a $MgCl_2$/LiCl mixture with different mass ratios (salt concentration: 2000 ppm); (c) desirable Mg^{2+}/Li^+ separation behavior; (d,e) long-term stability and Mg^{2+}/Li^+ selectivity of PA–TA–Cu membrane for $MgCl_2$/LiCl mixture (salt concentration: 2000 ppm, Mg^{2+}/Li^+ mass ratio = 20:1)

The durability of the PA–TA–Cu membrane was evaluated using a long-term continuous separation test lasting 7 days. As shown in **Fig. 3.13d–e**, the PA–TA–Cu membrane maintained a higher Mg^{2+} rejection (above 97.6%) with a corresponding separation factor (above 26.5) during the 7-day test. No significant fluctuations were observed in the rejection or permeance results. To explore the stability of Cu^{2+} ions in the PA-TA-Cu membrane, after different filtration times (feed solution: pure water), a certain amount of permeate was taken out and determined using an ICP. All

concentrations were below the detection limit (**Fig. 3.14**), indicating that Cu^{2+} ions remained stable in the PA–TA–Cu membrane without leaching during filtration. These results indicated the excellent stability of the PA–TA–Cu membrane. A comparison of the Mg^{2+}/Li^{+} separation performance of the PA–TA–Cu membranes and some reported polyamide NF membranes is summarized in **Table 3.2** The results show that our PA–TA–Cu membrane exhibits competitive Mg^{2+}/Li^{+} separation performance and has significant potential for lithium recovery from salt-lake brines.

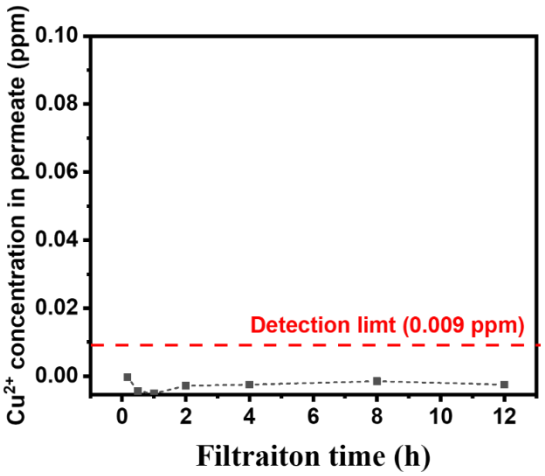

Fig. 3.14 Cu^{2+} concentration in the permeate after different filtration times (the permeate was diluted 10 times).

Table 3.2 Summary of the Mg^{2+}/Li^{+} separation performance of polyamide membranes (cross-flow nanofiltration mode).

Membrane type	Feed concentration (ppm)	Mg^{2+}/Li^{+} mass ratio	Separation factor ($S_{Mg^{2+}/Li^{+}}$)	Permeance for the feed solution (L m^{-2} h^{-1} bar^{-1})	Pure water permeance (L m^{-2} h^{-1} bar^{-1})	Ref.
PA–TA–Cu	2000	20	26.5	2.9	4.87	This work
PEI-Am-CDs-TMC	2000	20	15	3.1		[193]
PEI-70000/PA/PES	2000	50	150	2		[194]
PEI–TMC–EDTA			11.38		2.87	[162]
NF-90	2000	20	2.1			[89]
DAPP–TMC	2000	20	2.6		2.53	[89]
PEI–TMC	2000	20	20		5.02	[90]
BPEI–TMC–EDTA	2500	24	9.2	0.6		[163]
PEI/γ–CDs–TMC			10.80		4.86	[109]
PA–TG	2000	20	83	1.4		[164]

CNC-COOH/PEI–TMC	2000	30	12.15	4.17		[101]
CNC-COOH/PEI-TMC	2000	60	5.84	3.4		[101]
PEI-TMC/DAIB	25500	76.5	5.71	3.9		[116]

3.4 Conclusions

In this study, a polyphenol–metal–assisted method was designed to regulate the structure of PEI-based polyamide NF membranes. The coordination interactions between TA, PEI, and Cu^{2+} ions efficiently improved the distribution and loading of PEI monomers on the substrate and inhibited the diffusion of PEI into the organic phase. In addition, the Cu^{2+} ions severely reduced the activity of the amino groups and served as positive charge centers. The resultant PA–TA–Cu membrane possessed ultrathin thickness (≈11 nm), high positive charge, and relatively loose structure. Based on the synergetic effect of Donnan exclusion and size sieving, the PA–TA–Cu membrane exhibited a large rejection difference between $MgCl_2$ and LiCl. Furthermore, the NF membrane exhibited a high Mg^{2+}/Li^{+} separation factor and excellent long-term stability. This study provides a strategy for fabricating an excellent NF membrane for lithium extraction from salt-lake brines.

Chapter 4

Multifunctional role of surfactant-controlled polyamide membranes for highly efficient Mg^{2+}/Li^{+} separation

4.1. Introduction

With the rapid development of the new energy industry and the increasing popularity of electronic devices, there has been a sharp and unprecedented growth in the demand for lithium resources. Salt-lake brines account for approximately 64 % of the world's total lithium resources [3]. The salt-lake brine contains a higher concentration of Li^{+}, ranging from hundreds to thousands of parts per million [4]. The high concentration of the coexisting ions (e.g. Ca^{2+}, Mg^{2+}, K^{+}, and Na^{+}) enhances the difficulty of lithium extraction, especially Mg^{2+} ions. The excessively high Mg^{2+}/Li^{+} mass ratio (ranging from dozens to hundreds) and similar hydrated radius (Mg^{2+}, 4.23 Å VS Li^{+}, 3.82 Å [71].) are the key factors that hinder the lithium recovery efficiency. Thus, the development of efficient technologies for Mg^{2+}/Li^{+} mixture separation is crucial. To date, various technologies have been developed for extracting lithium from salt-lake brines, including precipitation [5, 6], adsorption, solvent extraction [7, 8], and membrane technology [9, 10]. The membrane technology stands up among them, due to the high separation efficiency and low energy consumption. Utilizing membranes to separate lithium-magnesium mixed solutions is efficient, simple to operate, and recyclable, making it an important research direction for lithium extraction from salt-lake brines.

Thin-film composite (TFC) nanofiltration (NF) membrane which consists of a porous substrate and a thin polyamide active layer, has attracted much attention due to its high selectivity and permeability. Based on the Donnan exclusion and size sieving

effect, NF membranes can retain multivalent ions while allowing monovalent ions to pass through, thus offering significant advantages in Mg^{2+}/Li^{+} separation. The PEI/TMC-based positively charged polyamide NF membrane, fabricated via interfacial polymerization (IP) at polyethyleneimine (PEI) aqueous and trimesoyl chloride (TMC) organic phase interface, was considered a promising choice for Mg^{2+}/Li^{+} separation. Compared to monovalent ions (Li^{+}), positive membranes usually exhibit a stronger electrostatic exclusion effect on divalent ions (Mg^{2+}) carrying more charges. The protonation of unreacted –NH_2– and –NH– groups in the PEI branch endow the PEI/TMC membrane positive charge [77, 119]. However, due to excessive cross-linking structure, PEI/TMC membranes display low permeance and high Li^{+} rejection.

In the typical IP process, the substrate was impregnated into a PEI aqueous phase, and after removal of the excess water, the TMC organic phase was applied onto the substrate. The IP reaction quickly occurred at the interface of the two immiscible phases. The PEI monomers diffuse from the aqueous phase to the organic phase and react with TMC. Therefore, the membrane performance can be optimized by regulating the IP reaction factors, such as the distribution of PEI monomers on the substrate and the PEI diffusion rate to the organic phase.

Various novel strategies have been developed to optimize the PEI/TMC-based NF membranes, by reducing the cross-linking degree and enhancing the positive charge [118]. The properties of the substrate, involving the wettability, roughness, and chemical composition, can affect the distribution of aqueous monomers on the substrate surface. The uniform distribution of aqueous monomers is beneficial to the formation of uniform and defect-free PA membranes. Interlayer construction [100, 101] and surface modification [102] are two common measures. The interlayer and surface coating can regulate the distribution and release of amine monomers through some interactions. Jin et al. [100] fabricated a PEI/TMC polyamide selective layer on the Kevlar hydrogel surface. Due to the interaction between Kevlar hydrogel and PEI, the ultrathin polyamide layer was obtained, which greatly reduced the water transport resistance, leading to twice water permeance of initial PES-based membranes.

In addition, some additives have been incorporated to adjust the structure of the polyamide layer, including metal-organic frameworks (MOFs) [104], silica (SiO_2) [105], carbon nanotubes (CNTs) [106, 107], graphene quantum dots (GQD) [108], γ-cyclodextrins (γ-CDs) [109], salt additives [127] and surfactant [195], etc. Among them, surfactant additives with excellent dispersibility have been proven an effective strategy to tailor the membrane structure, especially the anionic surfactants [169]. Surfactants commonly consist of groups with different hydrophilicity at each end, involving a long hydrophobic alkyl chain and a hydrophilic group. The incorporation of anionic surfactants in the aqueous phase is conductive to the uniform distribution and retention of aqueous monomers on the substrate surface, due to the improved wettability of substrate caused by various interactions with substrate and amino monomers [196]. Meanwhile, the concentration of amino monomers in the IP reaction zone also can be increased [10]. Moreover, the surfactant incorporation can significantly reduce the aqueous/organic interface tension, decrease the amino monomer diffusion hindrance, and further facilitate the spatially uniform diffusion process of amino monomer, thereby improving the separation performance of the fabricated polyamide membranes [197, 198]. The surfactant-assisted IP (SAIP) method can precisely regulate the pore size distribution [71], which is crucial for Mg^{2+}/Li^{+} separation, because the Li^{+} ions dehydrate more readily than Mg^{2+} ions under pressure-driven separation process [68-70], even though the hydrated radius difference between Mg^{2+} and Li^{+} is less than 0.1nm. Therefore, the SAIP method is expected to achieve an improvement of Mg^{2+}/Li^{+} separation performance of PEI/TMC-based NF membranes.

To our knowledge, there are few reports on using the SAIP strategy to fabricate PEI/TMC-based NF membranes with high Mg^{2+}/Li^{+} separation performance. Therefore, in this study, sodium n-decyl sulfate (SDES) was incorporated into the PEI aqueous phase to adjust the IP process (**Fig. 4.1**). The influences of varying SEDS concentration on the IP reaction process, membrane morphology, pore size distribution, and Mg^{2+}/Li^{+} separation performance was systemically studied. This work demonstrated the great potential of the SAIP strategy to fabricate PEI/TMC-based NF membranes with high

Mg^{2+}/Li^{+} separation performance.

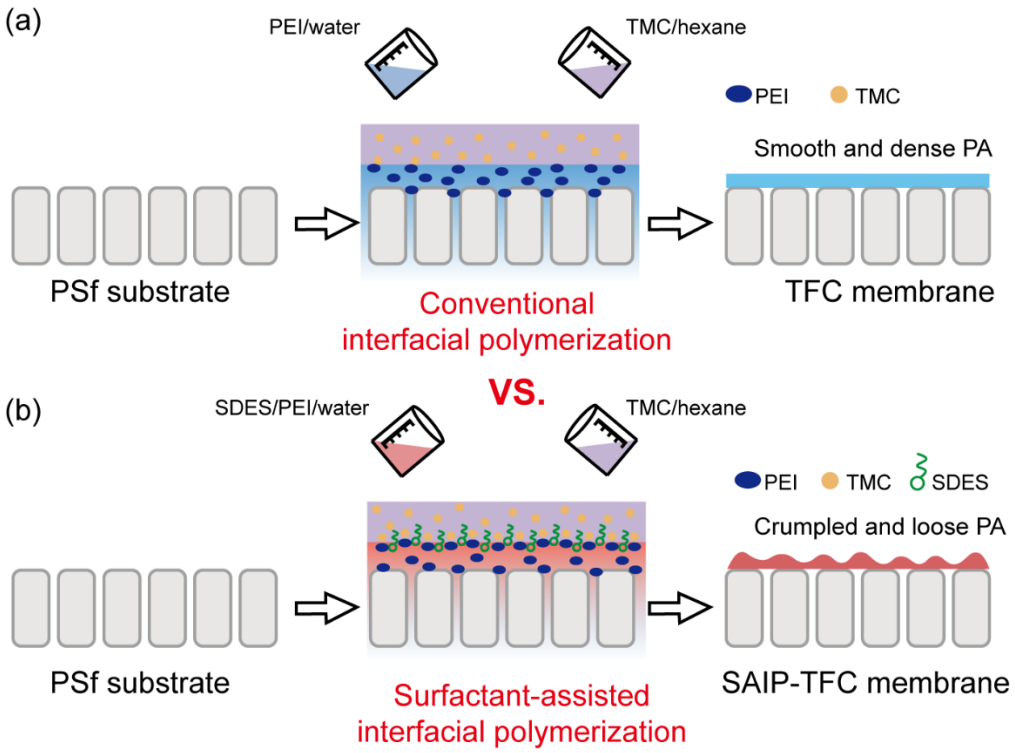

Fig. 4.1 Schematic diagrams of the fabrication process of (a) conventional IP and (b) SAIP method on the surface of PSf membrane.

4.2. Experimental section

4.2.1. Materials

Sodium n-decyl sulfate (SDES) was obtained from Sigma-Aldrich (St. Louis, MO, US). Other chemicals used in this chapter were the same as that in Chapter 2.

4.2.2. Fabrication of different NF membranes

0.5 g PEI and surfactant with different critical micelle concentrations (CMC) were dissolved in 100 ml water to obtain the aqueous phase solution. 0.15 g TMC was dissolved in 100 g n-hexane to obtain the organic phase solution. Then, the PEI aqueous solution was poured onto the PSf membrane and removed after 5 mins by an air knife. Subsequently, the pre-prepared TMC solution was poured onto the membrane to react with PEI, which was discarded after 3 min. Then, the freshly prepared TFC membrane

was transported into an oven and cured for another 10 min at 70 °C. Finally, the fabricated TFC membranes were taken out and soaked in Milli-Q water at 4℃ until the experiment. During the preparation of the TFC membrane, the concentrations of SDES used in PEI solution were 3.2 mM (0.1CMC), 8 mM (0.25CMC), , 16mM (0.5CMC), 24mM (0.75CMC), and 32 mM (1CMC).

4.2.3. Characterization

All the characterization methods were stated in previous chapters.

4.2.4. Interfacial tension measurement

The interfacial tension between n-hexane and deionized water or PEI aqueous solution with different SDES concentrations was evaluated using Sigma tensiometer system (Sigma 700, Biolin Scientific, Sweden) through Du Noüy ring method. Firstly, 15 mL deionized water or PEI aqueous solution was added into a disposable container, and then n-hexane was slightly poured onto the top of the aqueous solution. The Du Noüy ring was cauterized by flame (~1300 °C) to completely remove the contaminants on its surface. The ring was brought close to the interface but still kept into the aqueous phase, and then slightly elevated by Sigma tensiometer across the interface and into the n-hexane solution.

4.2.5. Quartz Crystal Microbalance (QCM) measure

In this study, the QCM system was used to monitor the SDES/water deposition process on the PEI-modified gold sensor, studying the interaction between PEI and SDES molecular. Before the QCM analysis, 40 μL PEI aqueous was drip-coated onto a gold-coated sensor with an effective area of 0.196 cm^{-2} and dried in an oven at 80 ℃ for 6 h. The PEI-modified gold sensor was installed into the flow module, and different solutions were introduced sequentially (following the order of water, 0.4 CMC SDES solution, and water) using a peristaltic pump. For comparison, the initial gold sensor was also tested in the same condition. Based on the values of frequency of the

oscillating crystal, the mass change of the sample can be calculated by the Sauerbrey equation [199]:

$$\Delta f = -\frac{2f_0^2}{A\sqrt{\rho_q \mu_q}}\Delta m \quad (4.1)$$

where Δf and Δm represent the frequency shift and mass change of the sensor after stabilization in a water environment, respectively. f_0 is the fundamental frequency (19.3 MHz). ρ_q is the density of the quartz crystal (2.648 g/cm^2). A is the effective area of the gold sensor (0.196 cm^2). μ_q is the shear stress of the quartz crystal (2.947 × 10^{11} g/cm s^{-2}).

4.2.6. Evaluation of the diffusion of PEI from aqueous into organic phase

The ultraviolet-visible (UV–vis) spectroscopy (V-650KE, JASCO Company, Japan) was used to measure the diffusion behavior of PEI from the aqueous phase into n-hexane, due to the UV peak intensity can present the PEI concentration in n-hexane [31-33]. Briefly, 10 mL PEI aqueous with different concentrations of SDES was injected into a glass container. Then, 10 ml n-hexane was lightly poured onto the aqueous solution. After 3 min, 2 mL n-hexane solution was taken out (maintain consistent position during the operation process), and the absorbance variation of PEI in n-hexane was measured via UV–vis method. The concentrations of PEI and SDES were the same as those in the IP process for PEI/SDES NF membrane fabrication.

4.2.7. Performance evaluation of PEI/SDES NF membrane

The separation performance of the fabricated NF membrane was tested using a cross-flow filtration setup (effective filtration area: 7.02 cm^2, flow rate: 9.9 mL min^{-1}). The calculation methods of water permanence, salt rejection, and Mg^{2+}/Li^+ mixture separation performance were stated in Chapter 2.

4.2.8. Evaluation of molecular weight cut-off (MWCO)

The MWCO of the fabricated TFC membranes was evaluated using 1000 ppm of different neutral sugars (Glycerol (92 Da), xylose (120 Da), D-(+)-glucose (180 Da),

sucrose (342 Da), and D-(+)-raffinose pentahydrate (504 Da)). The sugar concentrations of the feed and permeate solutions were determined using a total organic carbon analyzer (TOC-VCSN, Shimadzu Co., Japan).

The corresponding pore size distribution can be expressed by a probability density function. All the details are stated in Chapter 3.

4.3. Results and discussion

4.3.1. Characteristics of the surfactants

Fig. 4.2a shows the chemical structures of SDES and PEI. SDES is an anionic surfactant consisting of a hydrophilic sulfate group and a long hydrophobic alkyl (C10) chain. The contact angles of water droplets with different SDES concentrations are shown in **Fig. 4.2b**. With the increase of SDES concentration, the corresponding contact angles decrease a lot, because the addition of SDES into the water may enhance the wettability of water on the substrate, caused by the different hydrophilicity at each head of SDES. The hydrophobic segments can contact the hydrophobic part of PSf, through hydrophobic interaction, and the hydrophilic head was exposed to the aqueous solution, resulting better spread of water droplets on the PSf substrate. When the PEI was further added into the aqueous, the corresponding contact angles exhibited the same decreasing trend (**Fig. 4.2c**). The incorporation of SDES would promote the formation of a thicker water layer and adjust the retention of aqueous PEI monomers on the PSf substrate surface, which will influence the subsequent IP process [198]. In addition to the membrane surface, the SDES can also permeate into membrane pores, further increasing the PEI retention on the relative hydrophobic PSf substrate.

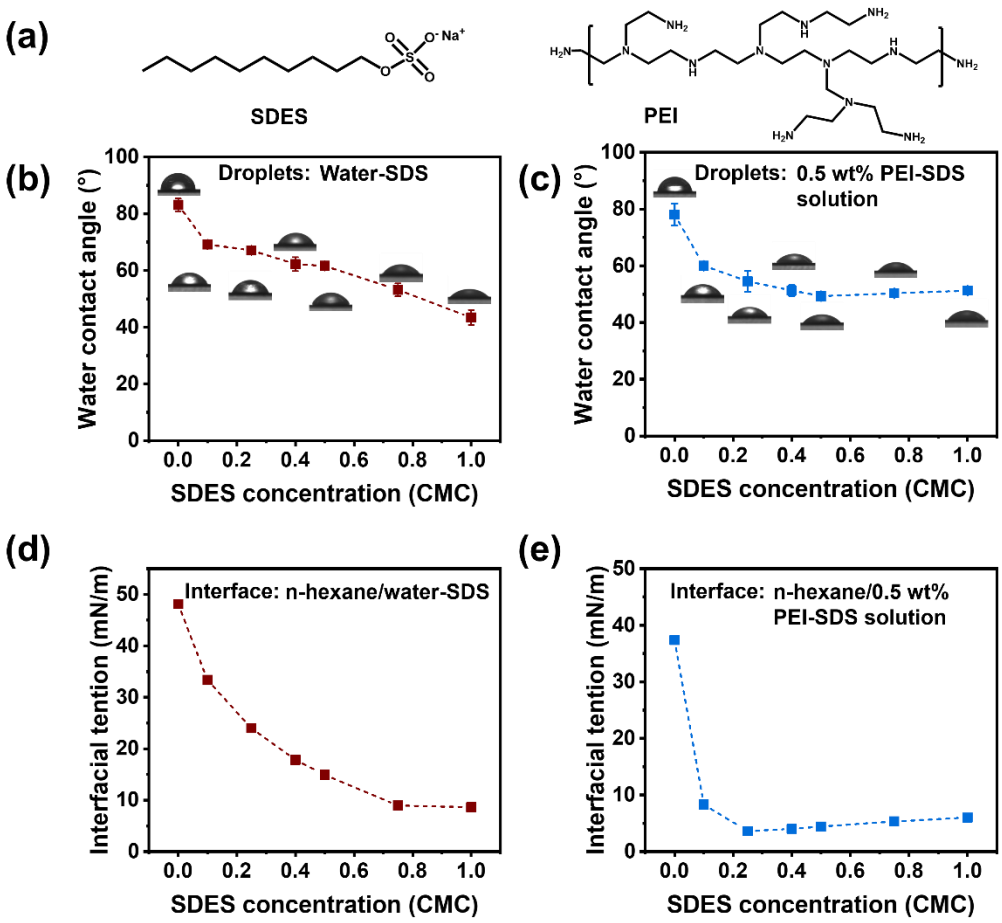

Fig. 4.2 (a) Chemical structures of SDES and PEI; (b) solution contact angles on PSf substrate (droplets containing different concentrations of SDES); (c) aqueous phase solution contact angles on PSf substrate (droplets containing 0.5 wt % PEI and different concentrations of SDES); (d) interfacial tension between n-hexane and water with different concentrations of SDES; (e) interfacial tension between n-hexane and 0.5 wt% PEI aqueous solution with different concentrations of SDES.

In addition to the wetting of aqueous solution on the substrate, the existence of the SDES would also influence the distribution and diffusion of PEI monomers at the water/n-hexane interface. The organic (n-hexane)–aqueous interfacial tension was determined using different concentrations of SDES aqueous solution without or with PEI (0.5 wt%), as shown in **Fig. 4.2d-e**. With the SDES concentration increases in an aqueous solution, the organic-aqueous interfacial tension decreases, consistent with the conclusion proposed by other researchers [200, 201]. It is worth noting that the

interfacial tension of the aqueous solution with PEI was lower than that without PEI. When the aqueous didn't contain SDES, the interfacial tension decreased from 48.1 to 37.4 mN/m with the addition of 0.5 wt% PEI monomers, which may be attributed to the counter-ion effect [202]. The interactions between SDES and PEI (**Fig. 4.3a**), especially the electrostatic binding, promote the formation of Gemini-like surfactants, and weaken the electrostatic repulsion between the negative-charge SDES molecules, reducing the interfacial tension [203].

To further characterize the strong interaction between the SDES and PEI molecule, a QCM system was used to analyze the microscopic variations of two sensors (initial gold sensor and PEI-modified sensor) in different environments, verifying their capturing capacity of water/SDES [196]. Different operation solutions were injected into the system sequentially (following the order of water, 0.4 CMC SDES solution, and water). When the baseline was stable, the operation solution (water) was substituted with the SDES solution (**Fig. 4.3b**). It can be observed that the frequency shift of the PEI-modified gold sensor is much lower and the corresponding deposition mass is much higher than that of the initial sensor (**Fig. 4.3c-d**), suggesting the PEI coating exhibited strong adsorption ability to SDES molecules. Subsequently, the water solution was injected into the system again. For the initial gold sensor, after water rinsing, the frequency shift increased and the deposition mass declined, showing its unstable adsorption to SDES molecules. In contrast, the frequency shift of the PEI-modified gold sensor further decreased and the mass increased (**Fig. 4.3c-d**), which can be attributed to the surface properties change (**Fig. 4.3b**). More water molecules can be captured by the SDES layer on the PEI coating. The QCM results successfully confirmed the presence of strong interactions between PEI and SDES molecules. Hence, the reduced interfacial tension, enhanced wettability of aqueous solution on the substrate, and the interaction between PEI and SDES molecules together improved the PEI storage ability of the PSf substrate when the PEI-SDES aqueous solution was poured onto it during the IP operation process, which is beneficial for the formation of a continuous and defect free PA film.

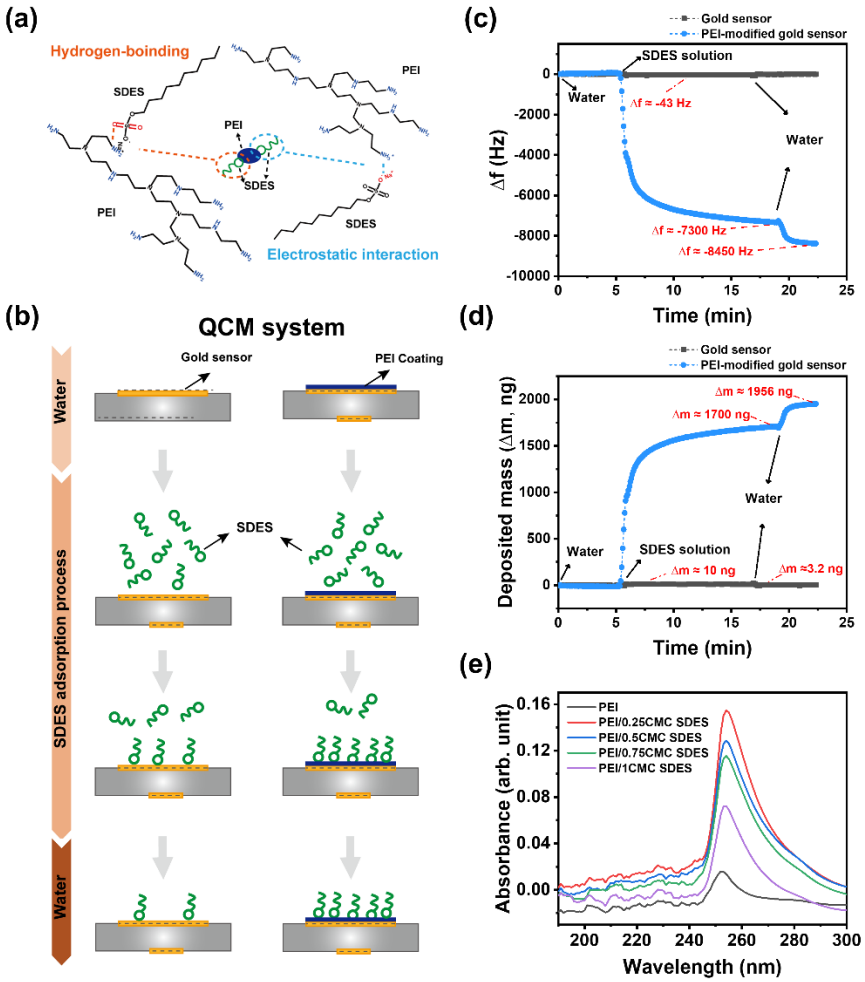

Fig. 4.3 (a) Schematic of possible interactions between PEI and SDES; (b) schematic of the adsorption process of different sensors to SDES molecular in QCM system; (c) frequency shift (*Δf*) and (d) deposited mass change (*Δm*) of the initial and PEI modified sensor in different environments (following the order of water, 0.4 CMC SDES solution, and water); (e) UV-vis spectra of PEI in organic phase (n-hexane) after 3 mins diffusion.

Researchers commonly assert that surfactant additives can adjust the diffusion behavior of amine monomers, thus promoting the IP reaction and improving the membrane performance [204]. To verify this phenomenon, the absorbance variation of PEI in n-hexane after 3 min diffusion was determined via a UV-vis spectrometer. As shown in **Fig. 4.3e**, the PEI diffusion rates first significantly increase and then slightly decrease as the concentration of the incorporated SDES increases. Because the SDES tended to form a monolayer at the interface and decrease the interfacial tension (**Fig.**

4.2 d-e), many PEI molecules can be adsorbed to the interface and form the SDES-PEI complex due to the strong interactions [10], leading to the increased PEI concentration near the water/hexane interface, which further promotes the uniform diffusion of PEI into the organic phase [169]. With the concentration SDES increase (>0.25 CMC), more and more SDES-PEI complexes will be arranged at the aqueous/organic interface, which can increase the spatial hindrance, leading to the increase of interfacial tension and the decrease of the PEI diffusion rate (**Fig. 4.2e** and **Fig. 4.3e**). The effect becomes more obvious when the SDES concentrations were overtopped (from 0.5 CMC to 1 CMC).

4.3.2. Membrane characterization and performance

The incorporation of SDES improves the wettability of aqueous solution on the substrate, increases the PEI loading amount, and adjusts the diffusion rate of PEI molecules, all of them can further influence the subsequent formation of the polyamide membranes. As shown in **Fig. 4.4**, the morphology of the SDES/PEI NF membranes prepared with different SDES concentrations was characterized. The surface morphology differences were caused by the alteration of interfacial tension and PEI diffusion rate that differed by varying the SDES concentration in the aqueous [195]. Specifically, the initial PA membrane displayed a relatively smooth surface with some small nodules, which is similar to some reported PEI/TMC membranes [113, 195]. With the incorporation of SDES, the surface exhibits a ring-like or nanowire-like crumpled structure, leading to a significant increase in the corresponding surface root-mean-square roughness (RMS). The appearance of these crumpled structures may be attributed to the following two main reasons. Firstly, the incorporation of SDES improves the wettability of the aqueous solution on the substrate surface. When the thick water layer contact with the organic phase, it tends to shrink due to the imbalance of the interfacial tension. The reduced interfacial tension increases the interfacial instability and makes the interface easier to deform [198]. The IP reaction that occurs on the water template can result in the generation of a rough polyamide film [205].

Secondly, the increased PEI concentration near the aqueous/organic interface and the lower interfacial tension can promote rapid cross-interface diffusion of PEI into the organic phase and accelerate the IP reaction. The more violent IP reaction commonly results in more rougher polyamide membrane [206]. When the SDES concentration exceeded 0.5 CMC, the surface morphology transformed from a ring-like crumpled structure to a nanowire-like crumpled structure, leading to a decrease in the corresponding surface roughness, which may be attributed to the increase in interfacial tension and the decrease in the PEI diffusion rate. The formation of the crumpled structure may increase the effective contact area during membrane separation process and can be expected to increase the water permeance of membrane.

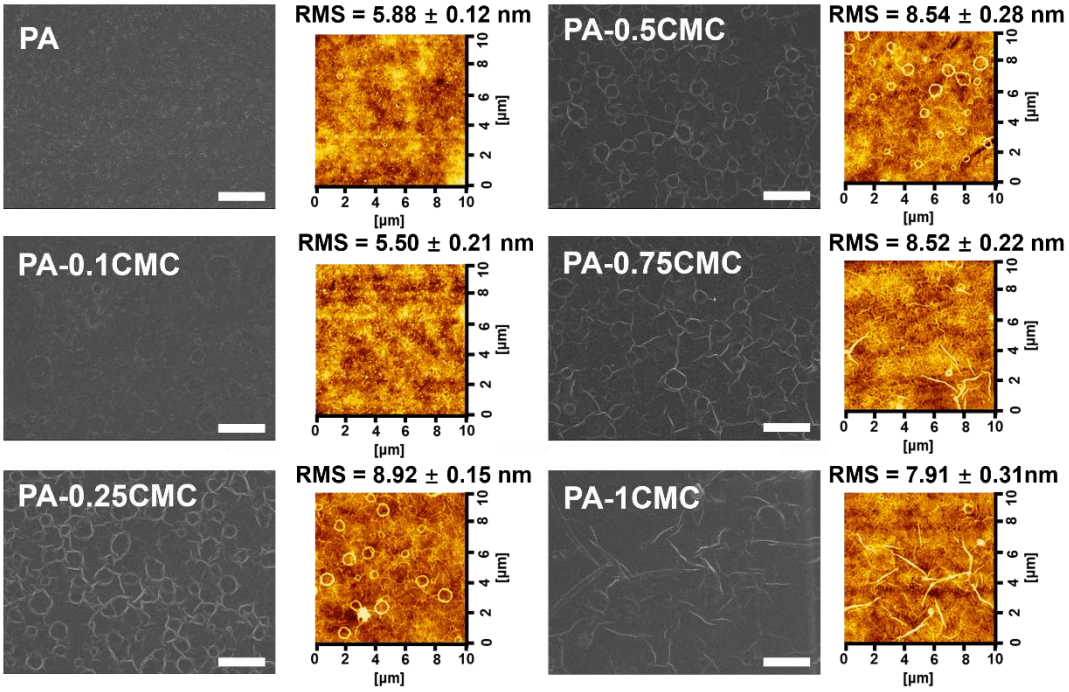

Fig. 4.4 SEM and AFM images of the PEI/SDES NF membranes prepared with different SDES concentrations (the scale value is 2 μm).

The chemical structures of the fabricated PEI/SDES NF membranes were characterized through ATR-FTIR and XPS. Compared to the PSf substrate, the PEI/SDES NF membranes exhibited a new peak at 1630 cm^{-1}, which was associated with the stretch vibration of -C=O- in the amide bond, and the peak in the range of 3310-3350 cm^{-1} was related to the -NH- bond (**Fig. 4.5a**) [118, 207]. Moreover, the N1s

peaks can be observed in the XPS spectrum (**Fig. 4.5b**), verifying the successful formation of polyamide film on the PSf substrate. With the incorporation of SDES, the N/C ratio increased a lot (**Fig. 4.5c**), which enhanced the membrane positive charge (**Fig. 4.5d**) and further confirmed that the SDES could improve the PEI monomer storage of the PSf substrate when the PEI/SDES aqueous solution was poured onto the substrate surface and more PEI monomers can diffuse from the aqueous phase to the organic phase and react with TMC.

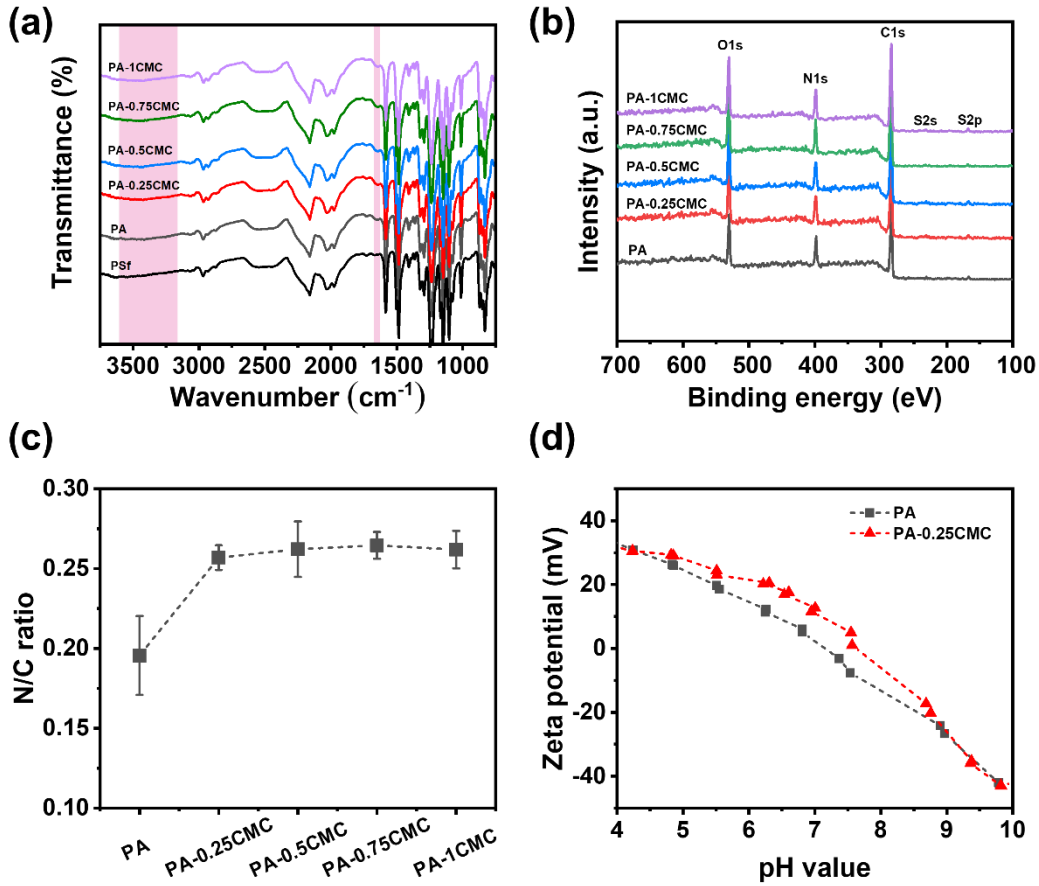

Fig. 4.5 ATR-FTIR spectra; (b) XPS spectra; and (c) N/C ratio of PEI/SDES NF membranes prepared with different SDES concentrations; (d) Zeta potential of initial PA and PA-0.25CMC membranes.

The pure water permeance of different fabricated PEI/SDES NF membranes is shown in **Fig. 4.6a**. The results displayed that the pure water permeance of the PEI/SDES NF membranes significantly increased with the incorporation of SEDS and an increase in the concentration. The generation of the crumpled polyamide surface

(**Fig. 4.4**) can increase the effective contact area during the separation process thus improving the permeance of the PEI/SDES NF membranes. **Fig. 4.6b** displays the rejection results of these PEI/SDES NF membranes for $MgCl_2$ and LiCl solution (2000 ppm). With the incorporation of a certain concentration of SDES (<0.5 CMC), there was no obvious decrease in the $MgCl_2$ rejection of PEI/SDES NF membranes (PA-0.1 CMC and PA-0.25 CMC), even though the corresponding water permeance significantly increased. The corresponding LiCl rejections are much lower than the initial PA membrane, especially the PA-0.25CMC membrane, exhibiting a Li^+ rejection of 21.5. Considering that the purpose of Mg^{2+}/Li^+ separation is to extract Li^+ from the mixture, the high Mg^{2+} rejection and low Li^+ rejection of PA-0.25CMC can be expected to endow it with great separation performance for Mg^{2+}/Li^+ separation. Further increasing incorporation concentrations of SDES (⩾0.5 CMC), the $MgCl_2$ rejection sharply declined. Due to the strong interaction between PEI and SDES, the SDES molecules can integrate with the polyamide matrix. The mutual repulsion between the long hydrophilic alkyl chain in SDES may increase the free volume of the PEI/SDES NF membranes, thereby improving the looseness of the PEI/TMC-based membrane [206, 208]. However, if the concentration of SDES is too high, it may lead to the generation of additional defects. In addition, I speculated that when the concentration of SDES is unduly high, many SDES-PEI complexes will be arranged at the aqueous/organic interface, and the big volume of the SDES-PEI complex may increase the spatial hindrance. The large spatial hindrance results in that little PEI monomers could diffuse from the aqueous phase to the organic phase and react with TMC, thus generating the polyamide membrane with some defects (large pores).

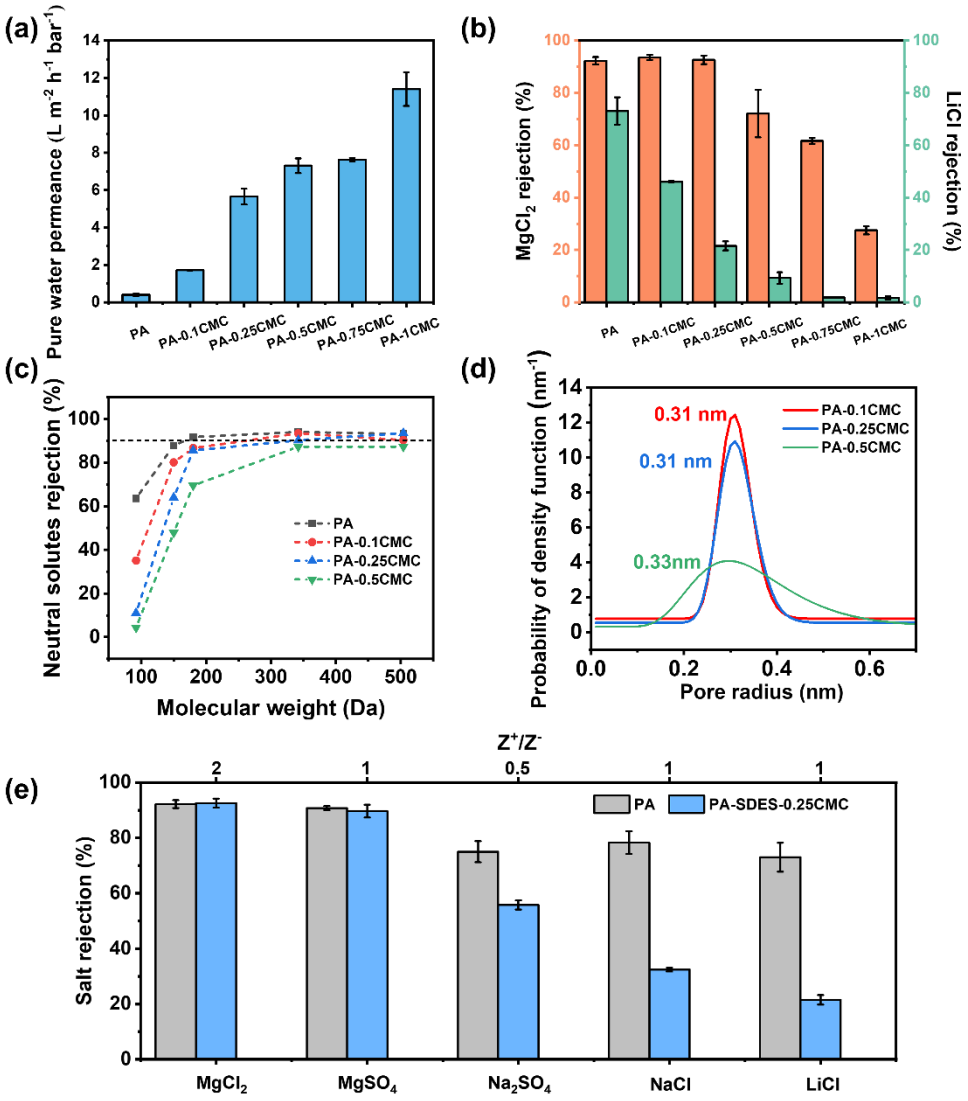

Fig. 4.6 (a) Pure water permeance, (b) $MgCl_2$ and LiCl rejection, (c) MWCO, and (d) pore size distribution of the PEI/SDES NF membrane prepared with different SDES concentrations;(e) the rejection of PA and PA-0.25CMC membrane for separating different inorganic salts (All the salt concentrations were 2000 ppm).

Five neutral carbohydrates (glycerol, 92Da; xylose, 120 Da; glucose, 180 Da; sucrose, 342 Da; and raffinose, 504 Da) were used to determine the molecular weight cut-off (MWCO) values of patrial PEI/SDES NF membranes (**Fig. 4.6c**). Compared with the initial PA membrane, all the PEI/SDES NF membranes exhibited relatively loose structure. Notably, the sharper MWCO value change of the PA-0.25CMC membrane between the molecular weights of 92 Da (glycerol) and 180 Da (glucose),

resulting in the PA-0.25CMC maintaining high Mg^{2+} retention while allowing more Li^{+} to pass through [209]. The PA-0.5CMC membrane shows low rejection for glucose, which corresponds to the low rejection of $MgCl_2$, indicating the existence of some large pores. Based on the MWCO values, the corresponding pore size distribution can be expressed and the results are shown in **Fig. 4.6d**. The PA-0.1CMC and PA-0.25CMC membranes exhibited small mean pore radius (0.31nm) and narrow pore size distribution (σ_p = 1.12 and σ_p = 1.13) than that of PA-0.5CMC membranes (mean pore radius = 0.33 nm and σ_p =1.40). The reason is that the appropriate amount of SDES molecules can promote the uniform diffusion of PEI into the organic phase to react with TMC, thereby generating a polyamide film with uniform pore size distribution. Combined with the loose structure, the uniform pore size distribution endows the PA-0.25CMC with a high Mg^{2+} rejection (92.6 %) and low Li^{+} rejection (21.5 %) (**Fig. 4.6a)**. The separation properties of the initial PA and PA-0.25CMC membranes were further determined using different inorganic salt solutions ($MgCl_2$, $MgSO_4$, Na_2SO_4, NaCl, and LiCl). The rejection order ($MgCl_2 \approx MgSO_4 > Na_2SO_4 > NaCl > LiCl$) was consistent with the trend of typical positively charged NF membranes reported in other literature [108, 156, 209], which was mainly ascribed to the combined effects of steric hindrance and Donnan exclusion. Furthermore, $MgCl_2$ and LiCl solutions with different concentrations (from 1g L^{-1} to 5 g L^{-1}) were used to investigate the influence of feed solution concentration on the PA-0.25CMC membrane performance (**Fig. 4.7**). As the concentration of the feed solution increases, the permeance decreases, which was ascribed to the reduced driving force caused by the increase of the osmotic pressure [113, 210]. Notably, the salt rejection is independent of the concentration of the feed solution, illustrating that the steric hindrance effect plays the main role in the separation process.

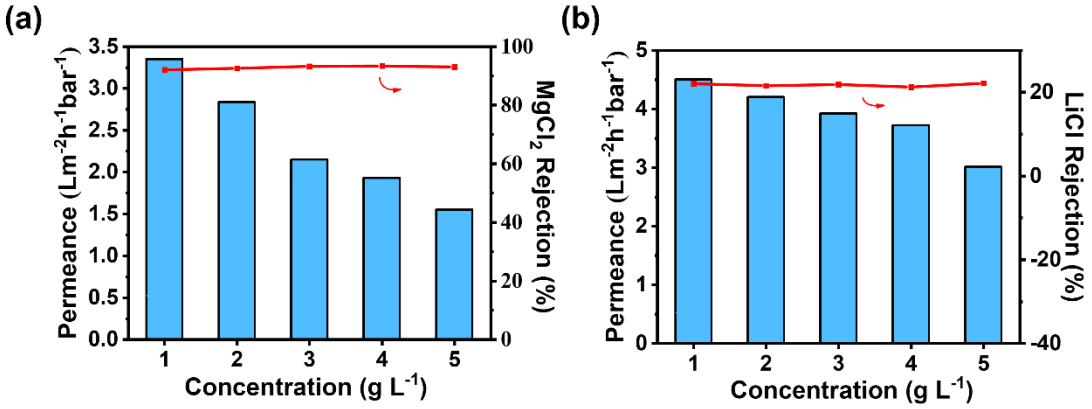

Fig. 4.7 The salt rejection and water permeance of PA-0.25CMC membrane in (a) $MgCl_2$ and (b) LiCl solution with different salt concentrations, respectively.

4.3.3. Mg^{2+}/Li^{+} separation performance

The $MgCl_2$/LiCl mixed solution with different Mg^{2+}/Li^{+} mass ratios (5:1, 10:1, 20:1, and 40:1) served as the feed solution to investigate the Mg^{2+}/Li^{+} separation performance of PA and PA-0.25CMC membranes. Compared to the initial PA membrane (**Fig. 4.8a**), the PA-0.25CMC membrane exhibited lower Li^{+} rejection, higher rejection difference between Mg^{2+} and Li^{+} (**Fig. 4.8b**), lower Mg^{2+}/Li^{+} ratio in permeate (**Fig. 4.8c**), and higher separation factor ($S_{Mg^{2+}/Li^{+}}$) (**Fig. 4.8d**), these are beneficial for the Li^{+} recovery from the feed solution. Especially, the Mg^{2+}/Li^{+} ratio decreased from the initial 5, 10, 20, and 40 (feed) to 0.36, 0.76, 1.6, and 3.08 (permeate) respectively after filtrating the feed solution through the PA-0.25CMC membrane. The corresponding Mg^{2+}/Li^{+} mass ratio in the permeate of the PA membrane is 0.65, 1.22, 2.29, and 4.28 respectively. All the results mentioned above indicate the acceptable Mg^{2+}/Li^{+} selectivity of the PA-0.25CMC membrane.

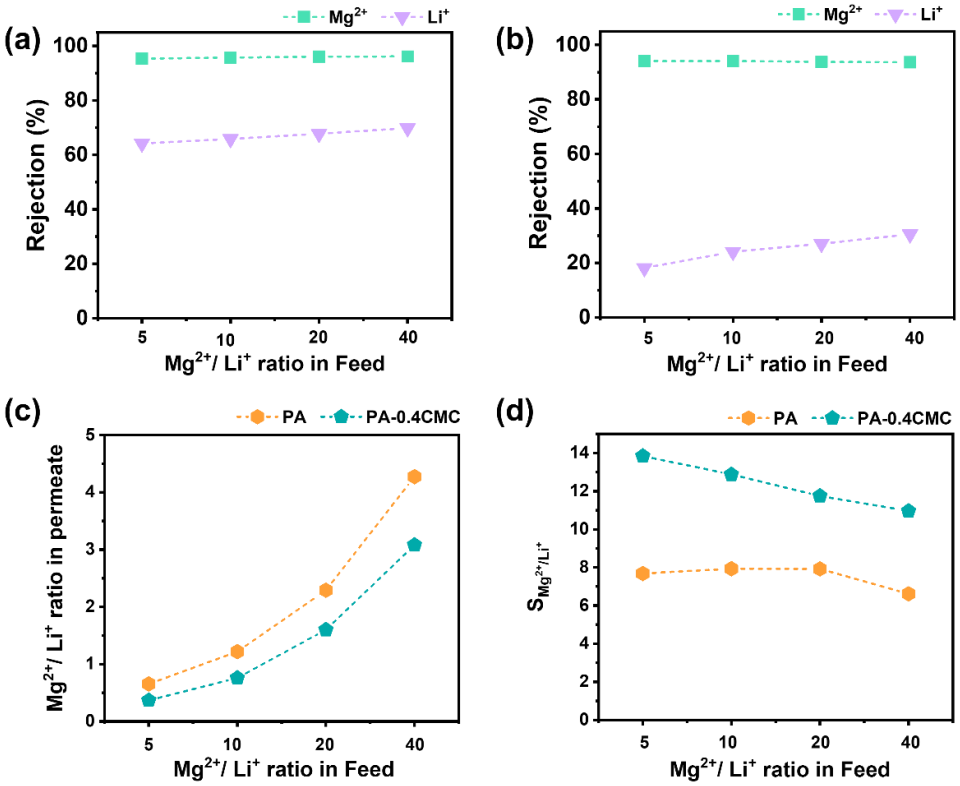

Fig. 4.8 The rejection performance of the (a) PA and (b) PA-0.25CMC membranes; (c) Mg^{2+}/Li^{+} mass ratio in permeate and (d) separation factor of PA and PA-0.25CMC membranes for mixed $MgCl_2$/LiCl solutions with different mass ratios (total salt concentration = 2000 ppm).

4.4. Conclusion

In this study, different concentrations of sodium n-decyl sulfate (SDES) were incorporated into the PEI aqueous phase to regulate the IP reaction. The incorporation of SDES decreases the aqueous/organic interface tension and increases the interfacial instability, resulting in the formation of a crumpled and loose PA selective layer. More effective contact area during the membrane separation process and significantly enhance the water permeance. The optimized PA-0.25CMC membrane exhibited a high $MgCl_2$ rejection (92.6 %) and a low LiCl rejection (21.5 %), with a pure water permanence of 5.65 L m^{-2} h^{-1} bar^{-1}. This study provides an efficient strategy to fabricate the PEI/TMC-based NF membranes with high Mg^{2+}/Li^{+} separation performance.

Chapter 5

Conclusions

With the rapid development of the new energy industry and the increasing popularity of electronic devices, there has been a sharp and unprecedented growth in the demand for lithium resources. Salt-lake brines account for approximately 64 % of the world's total lithium resources. The salt-lake brine contains a higher concentration of Li^+, ranging from hundreds to thousands of parts per million. The high concentration of the coexisting ions (e.g. Ca^{2+}, Mg^{2+}, K^+, and Na^+) enhances the difficulty of lithium extraction, especially Mg^{2+} ions. Thin film composite (TFC) membranes are the most widely used nanofiltration membranes and typically consist of a top polyamide (PA) active layer and a bottom porous substrate. The PEI/TMC-based positively charged polyamide NF membrane, fabricated via interfacial polymerization (IP) at polyethyleneimine (PEI) aqueous and trimesoyl chloride (TMC) organic phase interface, was considered a promising choice for Li^+/Mg^{2+} separation. However, the trade-off between the permeability and selectivity of TFC membranes limits further improvement of the separation performance. Producing PA membranes with higher water permeance without compromising their salt rejection ability is still a challenge. Therefore, the IP reaction conditions between PEI and TMC have been adjust in this dissertation to optimize the membrane structure and separation performance. All the results were described in Chapters 2-4, as follows:

5.1. Complexation of cellulose nanocrystals and amine monomer for improved interfacial polymerization of nanofiltration membrane

In this chapter, amine monomers (PEI) and CNC were complexed via a one-step

vacuum-assisted procedure, followed by IP with TMC, and i-TFN nanofiltration membranes were successfully fabricated. The strong electrostatic interaction between the CNC and PEI can limit the release and diffusion of the amine monomer during the IP process, resulting in the formation of a thinner PA film with a crumpled structure. The optimized membrane possessed a more effective permeable area of continuous polymer network, substantially increasing water permeability without compromising salt rejection performance. This study provides a strategy to regulate the distribution of amine monomers at the interface of the interlayer for the design and fabrication of membranes with high separation performance.

5.2. Ternary-coordination-regulated polyamide nanofiltration membranes for Mg^{2+}/Li^{+} separation

In this chapter, a polyphenol–metal–assisted method was designed to regulate the structure of PEI-based polyamide NF membranes. The coordination interactions between TA, PEI, and Cu^{2+} ions efficiently improved the distribution and loading of PEI monomers on the substrate and inhibited the diffusion of PEI into the organic phase. In addition, the Cu^{2+} ions severely reduced the activity of the amino groups and served as positive charge centers. The resultant PA–TA–Cu membrane possessed ultrathin thickness (≈11 nm), high positive charge, and relatively loose structure. Based on the synergetic effect of Donnan exclusion and size sieving, the PA–TA–Cu membrane exhibited a large rejection difference between $MgCl_2$ and LiCl. Furthermore, the NF membrane exhibited a high Li^{+}/Mg^{2+} separation factor and excellent long-term stability. This study provides a strategy for fabricating an excellent NF membrane for lithium extraction from salt-lake brines.

5.3 Multifunctional role of surfactant-controlled polyamide membranes for highly efficient Mg^{2+}/Li^{+} separation

In this chapter, different concentrations of sodium n-decyl sulfate (SDES) were incorporated into the PEI aqueous phase to regulate the IP reaction. The incorporation

of SDES decreases the aqueous/organic interface tension and increases the interfacial instability, resulting in the formation of a crumpled and loose PA selective layer. More effective contact area during the membrane separation process and significantly enhance the water permeance. The optimized PA-0.25CMC membrane exhibited a high $MgCl_2$ rejection (92.6 %) and a low LiCl rejection (21.5 %), with a pure water permanence of 5.65 L m^{-2} h^{-1} bar^{-1}. This study provides an efficient strategy to fabricate the PEI/TMC-based NF membranes with high Li^+/Mg^{2+} separation performance.

References

[1] J. Zhang, Z. Cheng, X. Qin, X. Gao, M. Wang, X. Xiang, Recent advances in lithium extraction from salt lake brine using coupled and tandem technologies, Desalination, 547 (2023).

[2] Y. Sun, Q. Wang, Y. Wang, R. Yun, X. Xiang, Recent advances in magnesium/lithium separation and lithium extraction technologies from salt lake brine, Separation and Purification Technology, 256 (2021).

[3] Mineral commodity summaries 2020, in: Mineral Commodity Summaries, Reston, VA, 2020, pp. 204.

[4] X.H. Li, Y.H. Mo, W.H. Qing, S.L. Shao, C.Y.Y. Tang, J.X. Li, Membrane-based technologies for lithium recovery from water lithium resources: A review, J Membrane Sci, 591 (2019).

[5] C. Xiao, L. Zeng, Thermodynamic study on recovery of lithium using phosphate precipitation method, Hydrometallurgy, 178 (2018) 283-286.

[6] S.-g. Zhu, W.-Z. He, G.-M. Li, Z. Xu, X.-j. ZHANG, J.-W. Huang, Recovery of Co and Li from spent lithium-ion batteries by combination method of acid leaching and chemical precipitation, Transactions of Nonferrous Metals Society of China, 22 (2012) 2274-2281.

[7] C. Shi, Y. Jing, Y. Jia, Solvent extraction of lithium ions by tri-n-butyl phosphate using a room temperature ionic liquid, Journal of Molecular Liquids, 215 (2016) 640-646.

[8] H. Su, Z. Li, J. Zhang, W. Liu, Z. Zhu, L. Wang, T. Qi, Combining selective extraction and easy stripping of lithium using a ternary synergistic solvent extraction system through regulation of Fe^{3+} coordination, ACS sustainable chemistry & engineering, 8 (2020) 1971-1979.

[9] P.-Y. Ji, Z.-Y. Ji, Q.-B. Chen, J. Liu, Y.-Y. Zhao, S.-Z. Wang, F. Li, J.-S. Yuan, Effect of coexisting ions on recovering lithium from high Mg^{2+}/Li^{+} ratio brines by selective-electrodialysis, Separation and Purification technology, 207 (2018) 1-11.

[10] Q. Peng, R. Wang, Z. Zhao, S. Lin, Y. Liu, D. Dong, Z. Wang, Y. He, Y. Zhu, J. Jin,

L. Jiang, Extreme Li-Mg selectivity via precise ion size differentiation of polyamide membrane, Nat Commun, 15 (2024) 2505.

[11] Y. Zhang, Y. Hu, N. Sun, S.A. Khoso, L. Wang, W. Sun, A novel precipitant for separating lithium from magnesium in high Mg/Li ratio brine, Hydrometallurgy, 187 (2019) 125-133.

[12] Y. Zhang, Y. Hu, L. Wang, W. Sun, Systematic review of lithium extraction from salt-lake brines via precipitation approaches, Minerals Engineering, 139 (2019) 105868.

[13] Z. Xu, H. Zhang, R. Wang, W. Gui, G. Liu, Y. Yang, Systemic and direct production of battery-grade lithium carbonate from a saline lake, Industrial & Engineering Chemistry Research, 53 (2014) 16502-16507.

[14] H. ZHONG, Y.-f. Zhou, H.-a. YIN, Progress in technology for extracting lithium from Li-bearing brine resources, Multipurpose Utilization of Mineral Resources, 1 (2003) 23-28.

[15] H. Wang, Y. Zhong, B. Du, Y. Zhao, M. Wang, Recovery of both magnesium and lithium from high Mg/Li ratio brines using a novel process, Hydrometallurgy, 175 (2018) 102-108.

[16] X. Liu, M. Zhong, X. Chen, Z. Zhao, Separating lithium and magnesium in brine by aluminum-based materials, Hydrometallurgy, 176 (2018) 73-77.

[17] P. Xu, J. Hong, X.M. Qian, Z.W. Xu, H. Xia, X.C. Tao, Z.Z. Xu, Q.Q. Ni, Materials for lithium recovery from salt lake brine, Journal of Materials Science, 56 (2021) 16-63.

[18] Q. Wei, B. Shi, F. Wang, S. Shao, L. Zhu, X. Zhao, Simple and rapid preparation of MIL-121 with small particles for lithium adsorption from brine, Coatings, 11 (2021) 854.

[19] J. Zhong, S. Lin, J. Yu, Li^+ adsorption performance and mechanism using lithium/aluminum layered double hydroxides in low grade brines, Desalination, 505 (2021) 114983.

[20] R.E.C. Torrejos, G.M. Nisola, H.S. Song, L.A. Limjuco, C.P. Lawagon, K.J. Parohinog, S. Koo, J.W. Han, W.-J. Chung, Design of lithium selective crown ethers:

Synthesis, extraction and theoretical binding studies, Chem Eng J, 326 (2017) 921-933.
[21] C.J. Pedersen, Cyclic polyethers and their complexes with metal salts, Journal of the American Chemical Society, 89 (1967) 7017-7036.
[22] T. Hayashita, J.H. Lee, M.G. Hankins, J.C. Lee, J.S. Kim, J.M. Knobeloch, R.A. Bartsch, Selective sorption and column concentration of alkali-metal cations by carboxylic acid resins with dibenzo-14-crown-4 subunits and their acyclic polyether analogs, Analytical chemistry, 64 (1992) 815-819.
[23] Y. Pranolo, Z. Zhu, C.Y. Cheng, Separation of lithium from sodium in chloride solutions using SSX systems with LIX 54 and Cyanex 923, Hydrometallurgy, 154 (2015) 33-39.
[24] E. Kunugida, Extraction and separation of lithium and sodium by solvent extraction with β-diketone and neutral ligand, Kagaku Kogaku Ronbunshu, 15 (1989) 504-510.
[25] W. Xiang, S. Liang, Z. Zhou, W. Qin, W. Fei, Lithium recovery from salt lake brine by counter-current extraction using tributyl phosphate/$FeCl_3$ in methyl isobutyl ketone, Hydrometallurgy, 171 (2017) 27-32.
[26] S. Chen, X. Nan, N. Zhang, L. Li, X. Yu, Y. Guo, T. Deng, Solvent extraction process and extraction mechanism for lithium recovery from high Mg/Li-ratio brine, Journal of Chemical Engineering of Japan, 52 (2019) 508-513.
[27] C. Shi, Y. Jia, Y. Jing, Lithium and magnesium separation from salt lake brine by ionic liquids containing tributyl phosphate, CIESC J, 66 (2015) 253-259.
[28] D.S. Sholl, R.P. Lively, Seven chemical separations to change the world, Nature, 532 (2016) 435-437.
[29] Z.-y. Ji, Q.-b. Chen, J.-s. Yuan, J. Liu, Y.-y. Zhao, W.-x. Feng, Preliminary study on recovering lithium from high Mg^{2+}/Li^{+} ratio brines by electrodialysis, Separation and Purification Technology, 172 (2017) 168-177.
[30] C. Jiang, B. Chen, Z. Xu, X. Li, Y. Wang, L. Ge, T. Xu, Ion-“distillation” for isolating lithium from lake brine, AIChE Journal, 68 (2022).
[31] P. Marchetti, M.F. Jimenez Solomon, G. Szekely, A.G. Livingston, Molecular

separation with organic solvent nanofiltration: a critical review, Chem Rev, 114 (2014) 10735-10806.

[32] Z. Yang, Y. Zhou, Z. Feng, X. Rui, T. Zhang, Z. Zhang, A Review on Reverse Osmosis and Nanofiltration Membranes for Water Purification, Polymers (Basel), 11 (2019).

[33] M. Racar, D. Dolar, A. Špehar, K. Košutić, Application of UF/NF/RO membranes for treatment and reuse of rendering plant wastewater, Process Safety and Environmental Protection, 105 (2017) 386-392.

[34] Y. Zhao, T. Tong, X. Wang, S. Lin, E.M. Reid, Y. Chen, Differentiating solutes with precise nanofiltration for next generation environmental separations: a review, Environmental Science & Technology, 55 (2021) 1359-1376.

[35] C.H. Ji, Z. Zhai, C. Jiang, P. Hu, S.Z. Zhao, S.M. Xue, Z. Yang, T. He, Q.J. Niu, Recent advances in high-performance TFC membranes: A review of the functional interlayers, Desalination, 500 (2021).

[36] Z. Wang, X. Luo, J. Zhang, F. Zhang, W. Fang, J. Jin, Polymer membranes for organic solvent nanofiltration: Recent progress, challenges and perspectives, Advanced Membranes, 3 (2023).

[37] S. Sourirajan, Separation of hydrocarbon liquids by flow under pressure through porous membranes, Nature, 203 (1964) 1348-1349.

[38] A.K. Hołda, I.F. Vankelecom, Integrally skinned PSf-based SRNF-membranes prepared via phase inversion—Part B: Influence of low molecular weight additives, J Membrane Sci, 450 (2014) 499-511.

[39] M. Sairam, X. Loh, Y. Bhole, I. Sereewatthanawut, K. Li, A. Bismarck, J. Steinke, A. Livingston, Spiral-wound polyaniline membrane modules for organic solvent nanofiltration (OSN), J Membrane Sci, 349 (2010) 123-129.

[40] J. da Silva Burgal, L.G. Peeva, S. Kumbharkar, A. Livingston, Organic solvent resistant poly (ether-ether-ketone) nanofiltration membranes, J Membrane Sci, 479 (2015) 105-116.

[41] Y. Hai, J. Zhang, C. Shi, A. Zhou, C. Bian, W. Li, Thin film composite

nanofiltration membrane prepared by the interfacial polymerization of 1, 2, 4, 5-benzene tetracarbonyl chloride on the mixed amines cross-linked poly (ether imide) support, J Membrane Sci, 520 (2016) 19-28.

[42] M. Mertens, T. Van Dyck, C. Van Goethem, A. Gebreyohannes, I.F. Vankelecom, Development of a polyvinylidene difluoride membrane for nanofiltration, J Membrane Sci, 557 (2018) 24-29.

[43] I.B. Valtcheva, S.C. Kumbharkar, J.F. Kim, Y. Bhole, A.G. Livingston, Beyond polyimide: Crosslinked polybenzimidazole membranes for organic solvent nanofiltration (OSN) in harsh environments, J Membrane Sci, 457 (2014) 62-72.

[44] L. Liu, M. Son, S. Chakraborty, C. Bhattacharjee, H. Choi, Fabrication of ultra-thin polyelectrolyte/carbon nanotube membrane by spray-assisted layer-by-layer technique: characterization and its anti-protein fouling properties for water treatment, Desalination and Water Treatment, 51 (2013) 6194-6200.

[45] M. Hu, B. Mi, Enabling graphene oxide nanosheets as water separation membranes, Environmental science & technology, 47 (2013) 3715-3723.

[46] S. Shao, F. Zeng, L. Long, X. Zhu, L.E. Peng, F. Wang, Z. Yang, C.Y. Tang, Nanofiltration Membranes with Crumpled Polyamide Films: A Critical Review on Mechanisms, Performances, and Environmental Applications, Environ Sci Technol, 56 (2022) 12811-12827.

[47] G.-R. Xu, S.-H. Wang, H.-L. Zhao, S.-B. Wu, J.-M. Xu, L. Li, X.-Y. Liu, Layer-by-layer (LBL) assembly technology as promising strategy for tailoring pressure-driven desalination membranes, J Membrane Sci, 493 (2015) 428-443.

[48] W. Cheng, C. Liu, T. Tong, R. Epsztein, M. Sun, R. Verduzco, J. Ma, M. Elimelech, Selective removal of divalent cations by polyelectrolyte multilayer nanofiltration membrane: Role of polyelectrolyte charge, ion size, and ionic strength, J Membrane Sci, 559 (2018) 98-106.

[49] L. Wang, N. Wang, H. Yang, Q. An, T. Zeng, S. Ji, Enhanced pH and oxidant resistance of polyelectrolyte multilayers via the confinement effect of lamellar graphene oxide nanosheets, Separation and Purification Technology, 193 (2018) 274-

282.

[50] C. Wang, M.J. Park, H. Yu, H. Matsuyama, E. Drioli, H.K. Shon, Recent advances of nanocomposite membranes using layer-by-layer assembly, J Membrane Sci, 661 (2022) 120926.

[51] J. Borges, J.F. Mano, Molecular interactions driving the layer-by-layer assembly of multilayers, Chemical reviews, 114 (2014) 8883-8942.

[52] B. Lian, J. Deng, G. Leslie, H. Bustamante, V. Sahajwalla, Y. Nishina, R. Joshi, Surfactant modified graphene oxide laminates for filtration, Carbon, 116 (2017) 240-245.

[53] G. Liu, J. Shen, Q. Liu, G. Liu, J. Xiong, J. Yang, W. Jin, Ultrathin two-dimensional MXene membrane for pervaporation desalination, J Membrane Sci, 548 (2018) 548-558.

[54] M. Zhao, Q. Lu, Q. Ma, H. Zhang, Two-dimensional metal–organic framework nanosheets, Small methods, 1 (2017) 1600030.

[55] V.A. Kuehl, J. Yin, P.H. Duong, B. Mastorovich, B. Newell, K.D. Li-Oakey, B.A. Parkinson, J.O. Hoberg, A highly ordered nanoporous, two-dimensional covalent organic framework with modifiable pores, and its application in water purification and ion sieving, Journal of the American Chemical Society, 140 (2018) 18200-18207.

[56] M. Safarpour, S. Arefi-Oskoui, A. Khataee, A review on two-dimensional metal oxide and metal hydroxide nanosheets for modification of polymeric membranes, Journal of Industrial and Engineering Chemistry, 82 (2020) 31-41.

[57] S.Z. Butler, S.M. Hollen, L. Cao, Y. Cui, J.A. Gupta, H.R. Gutiérrez, T.F. Heinz, S.S. Hong, J. Huang, A.F. Ismach, Progress, challenges, and opportunities in two-dimensional materials beyond graphene, ACS nano, 7 (2013) 2898-2926.

[58] Y.-C. An, X.-X. Gao, W.-L. Jiang, J.-L. Han, Y. Ye, T.-M. Chen, R.-Y. Ren, J.-H. Zhang, B. Liang, Z.-L. Li, A critical review on graphene oxide membrane for industrial wastewater treatment, Environmental Research, 223 (2023) 115409.

[59] X. Liu, L. Zhang, X. Cui, Q. Zhang, W. Hu, J. Du, H. Zeng, Q. Xu, 2D material nanofiltration membranes: from fundamental understandings to rational design,

Advanced Science, 8 (2021) 2102493.
[60] S. Zheng, Q. Tu, J.J. Urban, S. Li, B. Mi, Swelling of graphene oxide membranes in aqueous solution: characterization of interlayer spacing and insight into water transport mechanisms, ACS nano, 11 (2017) 6440-6450.
[61] K. Wang, X. Wang, B. Januszewski, Y. Liu, D. Li, R. Fu, M. Elimelech, X. Huang, Tailored design of nanofiltration membranes for water treatment based on synthesis-property-performance relationships, Chem Soc Rev, 51 (2022) 672-719.
[62] D. Lu, Z. Yao, L. Jiao, M. Waheed, Z. Sun, L. Zhang, Separation mechanism, selectivity enhancement strategies and advanced materials for mono-/multivalent ion-selective nanofiltration membrane, Advanced Membranes, 2 (2022).
[63] J. Luo, Y. Wan, Mix-charged nanofiltration membrane: Engineering charge spatial distribution for highly selective separation, Chem Eng J, 464 (2023).
[64] P. Atkins, A. MacDermott, The Born equation and ionic solvation, Journal of Chemical Education, 59 (1982) 359.
[65] M. Born, Volumen und hydratationswärme der ionen, Zeitschrift für physik, 1 (1920) 45-48.
[66] C. Lu, C. Hu, C.L. Ritt, X. Hua, J. Sun, H. Xia, Y. Liu, D.-W. Li, B. Ma, M. Elimelech, In situ characterization of dehydration during ion transport in polymeric nanochannels, Journal of the American Chemical Society, 143 (2021) 14242-14252.
[67] S. Sahu, M. Di Ventra, M. Zwolak, Dehydration as a universal mechanism for ion selectivity in graphene and other atomically thin pores, Nano letters, 17 (2017) 4719-4724.
[68] C. Lu, C. Hu, C.L. Ritt, X. Hua, J. Sun, H. Xia, Y. Liu, D.W. Li, B. Ma, M. Elimelech, J. Qu, In Situ Characterization of Dehydration during Ion Transport in Polymeric Nanochannels, J Am Chem Soc, 143 (2021) 14242-14252.
[69] V. Pavluchkov, I. Shefer, O. Peer-Haim, J. Blotevogel, R. Epsztein, Indications of ion dehydration in diffusion-only and pressure-driven nanofiltration, J Membrane Sci, 648 (2022).
[70] T. Xu, B. Wu, L. Hou, Y. Zhu, F. Sheng, Z. Zhao, Y. Dong, J. Liu, B. Ye, X. Li, L.

Ge, H. Wang, T. Xu, Highly Ion-Permselective Porous Organic Cage Membranes with Hierarchical Channels, J Am Chem Soc, 144 (2022) 10220-10229.

[71] Y. Liang, Y. Zhu, C. Liu, K.R. Lee, W.S. Hung, Z. Wang, Y. Li, M. Elimelech, J. Jin, S. Lin, Polyamide nanofiltration membrane with highly uniform sub-nanometre pores for sub-1 A precision separation, Nat Commun, 11 (2020) 2015.

[72] R. Epsztein, R.M. DuChanois, C.L. Ritt, A. Noy, M. Elimelech, Towards single-species selectivity of membranes with subnanometre pores, Nat Nanotechnol, 15 (2020) 426-436.

[73] F.G. Donnan, Theorie der Membrangleichgewichte und Membranpotentiale bei Vorhandensein von nicht dialysierenden Elektrolyten. Ein Beitrag zur physikalisch-chemischen Physiologie, Zeitschrift für Elektrochemie und angewandte physikalische Chemie, 17 (1911) 572-581.

[74] W. Zhao, H. Gong, Y. Song, B. Li, N. Xu, X. Min, G. Liu, B. Zhu, L. Zhou, X.X. Zhang, J. Zhu, Hierarchically Designed Salt-Resistant Solar Evaporator Based on Donnan Effect for Stable and High-Performance Brine Treatment, Advanced Functional Materials, 31 (2021).

[75] T. Zhang, W. Zheng, Q. Wang, Z. Wu, Z. Wang, Designed strategies of nanofiltration technology for Mg^{2+}/Li^{+} separation from salt-lake brine: A comprehensive review, Desalination, 546 (2023).

[76] S. Choi, Z. Yun, S. Hong, K. Ahn, The effect of co-existing ions and surface characteristics of nanomembranes on the removal of nitrate and fluoride, Desalination, 133 (2001) 53-64.

[77] Z. Wang, X. You, C. Yang, W. Li, Y. Li, Y. Li, J. Shen, R. Zhang, Y. Su, Z. Jiang, Ultrathin polyamide nanofiltration membranes with tunable chargeability for multivalent cation removal, J Membrane Sci, 642 (2022).

[78] J. Zhao, X. You, G. Wang, J. Yuan, Y. Li, C. Yang, S. Zhang, X. Wang, R. Zhang, H. Wu, Mix-charged polyamide membranes via molecular hybridization for selective ionic nanofiltration, J Membrane Sci, 644 (2022) 120051.

[79] L. Fumagalli, A. Esfandiar, R. Fabregas, S. Hu, P. Ares, A. Janardanan, Q. Yang,

B. Radha, T. Taniguchi, K. Watanabe, Anomalously low dielectric constant of confined water, Science, 360 (2018) 1339-1342.

[80] A.E. Yaroshchuk, Dielectric exclusion of ions from membranes, Advances in colloid and interface science, 85 (2000) 193-230.

[81] X. Wen, P. Ma, C. Zhu, Q. He, X. Deng, Preliminary study on recovering lithium chloride from lithium-containing waters by nanofiltration, Separation and Purification Technology, 49 (2006) 230-236.

[82] L. Gong, W. Ouyang, Z. Li, J. Han, Direct numerical simulation of continuous lithium extraction from high Mg^{2+}/Li^{+} ratio brines using microfluidic channels with ion concentration polarization, J Membrane Sci, 556 (2018) 34-41.

[83] S.-Y. Sun, L.-J. Cai, X.-Y. Nie, X. Song, J.-G. Yu, Separation of magnesium and lithium from brine using a Desal nanofiltration membrane, Journal of Water Process Engineering, 7 (2015) 210-217.

[84] G. Yang, H. Shi, W. Liu, W. Xing, N. Xu, Investigation of Mg^{2+}/Li^{+} Separation by Nanofiltration, Chinese Journal of Chemical Engineering, 19 (2011) 586-591.

[85] B.K. Pramanik, M.B. Asif, S. Kentish, L.D. Nghiem, F.I. Hai, Lithium enrichment from a simulated salt lake brine using an integrated nanofiltration-membrane distillation process, Journal of Environmental Chemical Engineering, 7 (2019).

[86] A. Somrani, A.H. Hamzaoui, M. Pontie, Study on lithium separation from salt lake brines by nanofiltration (NF) and low pressure reverse osmosis (LPRO), Desalination, 317 (2013) 184-192.

[87] J. Antczak, M. Szczygiełda, K. Prochaska, Nanofiltration separation of succinic acid from post-fermentation broth: Impact of process conditions and fouling analysis, Journal of Industrial and Engineering Chemistry, 77 (2019) 253-261.

[88] L. Zhang, M. Hu, Y. Zhang, J. Hou, M. Zhang, C. Gao, W. Fu, H. Hui, Q. Liu, H. Ding, Phytic acid and ferric chloride compound additives-regulated interfacial polymerization for high-performance nanofiltration membrane, J Membrane Sci, 693 (2024) 122386.

[89] X. Li, C. Zhang, S. Zhang, J. Li, B. He, Z. Cui, Preparation and characterization

of positively charged polyamide composite nanofiltration hollow fiber membrane for lithium and magnesium separation, Desalination, 369 (2015) 26-36.

[90] P. Xu, W. Wang, X.M. Qian, H.B. Wang, C.S. Guo, N. Li, Z.W. Xu, K.Y. Teng, Z. Wang, Positive charged PEI-TMC composite nanofiltration membrane for separation of Li^+ and Mg^{2+} from brine with high Mg^{2+}/Li^+ ratio, Desalination, 449 (2019) 57-68.

[91] P. Xu, R.R. Gonzales, J. Hong, K. Guan, Y.-H. Chiao, Z. Mai, Z. Li, S. Rajabzadeh, H. Matsuyama, Fabrication of highly positively charged nanofiltration membranes by novel interfacial polymerization: Accelerating Mg^{2+} removal and Li^+ enrichment, J Membrane Sci, 668 (2023).

[92] Y.H. Li, S.H. Wang, W.Y. Wu, H.J. Yu, R.X. Che, G.D. Kang, Y.M. Cao, Fabrication of positively charged nanofiltration membrane with uniform charge distribution by reversed interfacial polymerization for Mg^{2+}/Li^+ separation, J Membrane Sci, 659 (2022).

[93] M.-B. Wu, H. Ye, Z.-Y. Zhu, G.-T. Chen, L.-L. Ma, S.-C. Liu, L. Liu, J. Yao, Z.-K. Xu, Positively-charged nanofiltration membranes constructed via gas/liquid interfacial polymerization for Mg^{2+}/Li^+ separation, J Membrane Sci, 644 (2022).

[94] C. Guo, Y. Qian, P. Liu, Q. Zhang, X. Zeng, Z. Xu, S. Zhang, N. Li, X. Qian, F. Yu, One-step construction of the positively/negatively charged ultrathin janus nanofiltration membrane for the separation of Li^+ and Mg^{2+}, Acs Appl Mater Inter, 15 (2023) 4814-4825.

[95] Z.-L. Qiu, W.-H. Yu, Y.-J. Shen, B.-K. Zhu, L.-F. Fang, Janus charged polyamide nanofilm with ultra-high separation selectivity for mono-/divalent ions, Chem Eng J, 416 (2021) 129023.

[96] D. Lu, T. Ma, S. Lin, Z. Zhou, G. Li, Q. An, Z. Yao, Q. Sun, Z. Sun, L. Zhang, Constructing a selective blocked-nanolayer on nanofiltration membrane via surface-charge inversion for promoting Li^+ permselectivity over Mg^{2+}, J Membrane Sci, 635 (2021).

[97] Z. Yang, W. Fang, Z. Wang, R. Zhang, Y. Zhu, J. Jin, Dual-skin layer nanofiltration membranes for highly selective Li^+/Mg^{2+} separation, J Membrane Sci, 620 (2021).

[98] R.R. He, S.S. Xu, R.Y. Wang, B.Y. Bai, S.H. Lin, T. He, Polyelectrolyte-based nanofiltration membranes with exceptional performance in Mg^{2+}/Li^{+} separation in a wide range of solution conditions, J Membrane Sci, 663 (2022).

[99] M. Zelner, P. Jahn, M. Ulbricht, V. Freger, A mixed-charge polyelectrolyte complex nanofiltration membrane: Preparation, performance and stability, J Membrane Sci, 636 (2021) 119579.

[100] P. Jin, V. Mattelaer, S. Yuan, M. Bassyouni, K. Simoens, X. Zhang, F. Ceyssens, K. Bernaerts, R. Dewil, B. Van der Bruggen, Hydrogel supported positively charged ultrathin polyamide layer with antimicrobial properties via Ag modification, Separation and Purification Technology, 284 (2022).

[101] C. Guo, N. Li, X. Qian, J. Shi, M. Jing, K. Teng, Z. Xu, Ultra-thin double Janus nanofiltration membrane for separation of Li^{+} and Mg^{2+}: "Drag" effect from carboxyl-containing negative interlayer, Separation and Purification Technology, 230 (2020).

[102] Z. Yang, X. Huang, J. Wang, C.Y. Tang, Novel polyethyleneimine/TMC-based nanofiltration membrane prepared on a polydopamine coated substrate, Frontiers of Chemical Science and Engineering, 12 (2017) 273-282.

[103] M. Wang, W. Dong, Y. Guo, Z. Zhai, Z. Feng, Y. Hou, P. Li, Q.J. Niu, Positively charged nanofiltration membranes mediated by a facile polyethyleneimine-Noria interlayer deposition strategy, Desalination, 513 (2021).

[104] F. Aghili, A.A. Ghoreyshi, B. Van der Bruggen, A. Rahimpour, A highly permeable UiO-66-NH_2/polyethyleneimine thin-film nanocomposite membrane for recovery of valuable metal ions from brackish water, Process Safety and Environmental Protection, 151 (2021) 244-256.

[105] H. Wu, H. Zhao, Y. Lin, X. Liu, L. Wang, H. Yao, Y. Tang, L. Yu, H. Wang, X. Wang, Positively-charged PEI/TMC nanofiltration membrane prepared by adding a diamino-silane coupling agent for Li^{+}/Mg^{2+} separation, J Membrane Sci, 672 (2023).

[106] H.-Z. Zhang, Z.-L. Xu, H. Ding, Y.-J. Tang, Positively charged capillary nanofiltration membrane with high rejection for Mg^{2+} and Ca^{2+} and good separation for Mg^{2+} and Li^{+}, Desalination, 420 (2017) 158-166.

[107] P. Xu, J. Hong, Z.Z. Xu, H. Xia, Q.Q. Ni, MWCNTs-COOK-assisted high positively charged composite membrane: Accelerating Li^+ enrichment and Mg^{2+} removal, Composites Part B-Engineering, 212 (2021).

[108] P. Xu, J. Hong, Z. Xu, H. Xia, Q.-Q. Ni, Novel aminated graphene quantum dots (GQDs-NH_2)-engineered nanofiltration membrane with high Mg^{2+}/Li^+ separation efficiency, Separation and Purification Technology, 258 (2021).

[109] Y. Zhao, N. Li, J. Shi, Y. Xia, B. Zhu, R. Shao, C. Min, Z. Xu, H. Deng, Extra-thin composite nanofiltration membranes tuned by γ-cyclodextrins containing amphipathic cavities for efficient separation of magnesium/lithium ions, Separation and Purification Technology, 286 (2022).

[110] F.A. Christy, P.S. Shrivastav, Conductometric studies on cation-crown ether complexes: a review, Critical Reviews in Analytical Chemistry, 41 (2011) 236-269.

[111] T. Li, X. Zhang, Y. Zhang, J. Wang, Z. Wang, S. Zhao, Nanofiltration membrane comprising structural regulator Cyclen for efficient Li^+/Mg^{2+} separation, Desalination, 556 (2023).

[112] H. Li, Y. Wang, T. Li, X.-K. Ren, J. Wang, Z. Wang, S. Zhao, Nanofiltration membrane with crown ether as exclusive Li^+ transport channels achieving efficient extraction of lithium from salt lake brine, Chem Eng J, 438 (2022).

[113] Z. Zha, T. Li, I. Hussein, Y. Wang, S. Zhao, Aza-crown ether-coupled polyamide nanofiltration membrane for efficient Li^+/Mg^{2+} separation, J Membrane Sci, 695 (2024).

[114] H. Luo, H. Peng, Q. Zhao, High flux Mg^{2+}/Li^+ nanofiltration membranes prepared by surface modification of polyethylenimine thin film composite membranes, Applied Surface Science, 579 (2022).

[115] F. Soyekwo, H. Wen, D. Liao, C. Liu, Nanofiltration Membranes Modified with a Clustered Multiquaternary Ammonium-Based Ionic Liquid for Improved Magnesium/Lithium Separation, ACS Appl Mater Interfaces, 14 (2022) 32420-32432.

[116] H.W. Peng, Q. Zhao, A Nano-Heterogeneous Membrane for Efficient Separation of Lithium from High Magnesium/Lithium Ratio Brine, Advanced Functional Materials, 31 (2021).

[117] Y. Xu, H. Peng, H. Luo, Q. Zhang, Z. Liu, Q. Zhao, High performance Mg^{2+}/Li^{+} separation membranes modified by a bis-quaternary ammonium salt, Desalination, 526 (2022).

[118] X. Liu, Y. Feng, Y. Ni, H. Peng, S. Li, Q. Zhao, High-permeance Mg^{2+}/Li^{+} separation nanofiltration membranes intensified by quadruple imidazolium salts, J Membrane Sci, 667 (2023).

[119] Q. Wang, Y. Wang, Y. Huang, H. Wang, Y. Gao, M. Zhao, L. Tu, L. Xue, C. Gao, Polyethyleneimine (PEI) based positively charged thin film composite polyamide (TFC-PA) nanofiltration (NF) membranes for effective Mg^{2+}/Li^{+} separation, Desalination, 565 (2023).

[120] J.Y. Zhu, J.W. Hou, S.S. Yuan, Y. Zhao, Y. Li, R.J. Zhang, M.M. Tian, J. Li, J. Wang, B. Van der Bruggen, MOF-positioned polyamide membranes with a fishnet-like structure for elevated nanofiltration performance, Journal of Materials Chemistry A, 7 (2019) 16313-16322.

[121] X. Lu, M. Elimelech, Fabrication of desalination membranes by interfacial polymerization: history, current efforts, and future directions, Chem Soc Rev, 50 (2021) 6290-6307.

[122] M. Elimelech, W.A. Phillip, The future of seawater desalination: energy, technology, and the environment, Science, 333 (2011) 712-717.

[123] M.A. Shannon, P.W. Bohn, M. Elimelech, J.G. Georgiadis, B.J. Marinas, A.M. Mayes, Science and technology for water purification in the coming decades, Nature, 452 (2008) 301-310.

[124] H. Guo, X. Li, W. Yang, Z. Yao, Y. Mei, L.E. Peng, Z. Yang, S. Shao, C.Y. Tang, Nanofiltration for drinking water treatment: a review, Front Chem Sci Eng, 16 (2022) 681-698.

[125] F. Zhang, J.B. Fan, S. Wang, Interfacial Polymerization: From Chemistry to Functional Materials, Angew Chem Int Ed Engl, 59 (2020) 21840-21856.

[126] Z. Tan, S. Chen, X. Peng, L. Zhang, C. Gao, Polyamide membranes with nanoscale Turing structures for water purification, Science, 360 (2018) 518-521.

[127] D.Y. Zheng, D. Hua, X. Cheng, J.Y. Pan, A.R. Ibrahim, H.M. Hua, P. Zhang, X.W. Cha, K.J. Xu, G.W. Zhan, Polyamide composite membranes for enhanced organic solvent nanofiltration performance by metal ions assisted interfacial polymerization method, Aiche Journal, 69 (2023).

[128] G.S. Lai, W.J. Lau, P.S. Goh, A.F. Ismail, Y.H. Tan, C.Y. Chong, R. Krause-Rehberg, S. Awad, Tailor-made thin film nanocomposite membrane incorporated with graphene oxide using novel interfacial polymerization technique for enhanced water separation, Chem Eng J, 344 (2018) 524-534.

[129] L. Valentino, M. Matsumoto, W.R. Dichtel, B.J. Marinas, Development and Performance Characterization of a Polyimine Covalent Organic Framework Thin-Film Composite Nanofiltration Membrane, Environ Sci Technol, 51 (2017) 14352-14359.

[130] F. Xiao, X. Hu, Y. Chen, Y. Zhang, Porous Zr-Based Metal-Organic Frameworks (Zr-MOFs)-Incorporated Thin-Film Nanocomposite Membrane toward Enhanced Desalination Performance, ACS Appl Mater Interfaces, 11 (2019) 47390-47403.

[131] L. Bai, Y. Liu, N. Bossa, A. Ding, N. Ren, G. Li, H. Liang, M.R. Wiesner, Incorporation of Cellulose Nanocrystals (CNCs) into the Polyamide Layer of Thin-Film Composite (TFC) Nanofiltration Membranes for Enhanced Separation Performance and Antifouling Properties, Environ Sci Technol, 52 (2018) 11178-11187.

[132] Y.T. Liu, L.M. Bai, X.W. Zhu, D.L. Xu, G.B. Li, H. Liang, M.R. Wiesner, The role of carboxylated cellulose nanocrystals placement in the performance of thin-film composite (TFC) membrane, J Membrane Sci, 617 (2021).

[133] Z. Zhou, S.Q. Zhou, X.X. Cheng, W.K. Liu, R.X. Wu, J. Wang, B. Liu, J.Y. Zhu, B. Van der Bruggen, Y.T. Zhang, Ultrathin polyamide membranes enabled by spin-coating assisted interfacial polymerization for high-flux nanofiltration, Separation and Purification Technology, 288 (2022).

[134] S.Q. Wu, F. Wang, S.H. Zhou, L. Long, Z. Yang, C.Y. Tang, Vacuum-assisted MPD loading toward promoted nanoscale structure and enhanced water permeance of polyamide RO membrane, Separation and Purification Technology, 297 (2022).

[135] Z. Wang, Z. Chen, Z. Zheng, H. Liu, L. Zhu, M. Yang, Y. Chen, Nanocellulose-

based membranes for highly efficient molecular separation, Chem Eng J, 451 (2023).
[136] X. Wu, Y. Li, X. Cui, J. Wang, X. Cao, P. Zhang, L. Zheng, Adsorption-Assisted Interfacial Polymerization toward Ultrathin Active Layers for Ultrafast Organic Permeation, ACS Appl Mater Interfaces, 10 (2018) 10445-10453.
[137] J.J. Wang, H.C. Yang, M.B. Wu, X. Zhang, Z.K. Xu, Nanofiltration membranes with cellulose nanocrystals as an interlayer for unprecedented performance, Journal of Materials Chemistry A, 5 (2017) 16289-16295.
[138] D. Bondeson, A. Mathew, K. Oksman, Optimization of the isolation of nanocrystals from microcrystalline cellulose by acid hydrolysis, Cellulose, 13 (2006) 171-180.
[139] C.Y. Zhu, H.N. Li, J. Yang, J.J. Li, J.R. Ye, Z.K. Xu, Vacuum-assisted diamine monomer distribution for synthesizing polyamide composite membranes by interfacial polymerization, J Membrane Sci, 616 (2020).
[140] Y. Li, X. You, Y. Li, J. Yuan, J. Shen, R. Zhang, H. Wu, Y. Su, Z. Jiang, Graphene quantum dot engineered ultrathin loose polyamide nanofilms for high-performance nanofiltration, Journal of Materials Chemistry A, 8 (2020) 23930-23938.
[141] Q.Q. Song, Y.Q. Lin, S.Y. Zhou, T. Istirokhatun, Z. Wang, Q. Shen, Z.H. Mai, K.C. Guan, H. Matsuyama, Highly permeable nanofilms with asymmetric multilayered structure engineered via amine-decorated interlayered interfacial polymerization, J Membrane Sci, 670 (2023).
[142] Q.Q. Song, Y.Q. Lin, T. Ueda, T. Istirokhatun, Q. Shen, K.C. Guan, T. Yoshioka, H. Matsuyama, Mechanism insights into the role of the support mineralization layer toward ultrathin polyamide nanofilms for ultrafast molecular separation, Journal of Materials Chemistry A, 9 (2021) 26159-26171.
[143] K.C. Guan, Y. Sasaki, Y.D. Jia, R.R. Gonzales, P.F. Zhang, Y.Q. Lin, Z. Li, H. Matsuyama, Interfacial polymerization of thin film selective membrane layers: Effect of polyketone substrates, J Membrane Sci, 640 (2021).
[144] X. You, H. Wu, R. Zhang, Y. Su, L. Cao, Q. Yu, J. Yuan, K. Xiao, M. He, Z. Jiang, Metal-coordinated sub-10 nm membranes for water purification, Nat Commun, 10

(2019) 4160.

[145] S. Yuan, G. Zhang, J. Zhu, N. Mamrol, S. Liu, Z. Mai, P. Van Puyvelde, B. Van der Bruggen, Hydrogel assisted interfacial polymerization for advanced nanofiltration membranes, Journal of Materials Chemistry A, 8 (2020) 3238-3245.

[146] Y. Shi, Z. Wang, Z. Mai, Q. Shen, Q. Song, W. Fu, S. Xiang, S. Fang, P. Zhang, Y.-H. Chiao, K. Guan, H. Matsuyama, Nanomorphogenesis of template-induced crumpled polyamide nanofiltration membranes, J Membrane Sci, 686 (2023).

[147] M.B. Wu, C. Zhang, J.K. Pi, C. Liu, J. Yang, Z.K. Xu, Cellulose nanocrystals as anti-oil nanomaterials for separating crude oil from aqueous emulsions and mixtures, Journal of Materials Chemistry A, 7 (2019) 7033-7041.

[148] L. Bai, J. Ding, H. Wang, N. Ren, G. Li, H. Liang, High-performance nanofiltration membranes with a sandwiched layer and a surface layer for desalination and environmental pollutant removal, Sci Total Environ, 743 (2020) 140766.

[149] W. Yang, M. Pan, J. Zhang, L. Zhang, F. Lin, X. Liu, C. Huang, X.Z. Chen, J. Wang, B. Yan, H. Zeng, A Universal Strategy for Constructing Robust and Antifouling Cellulose Nanocrystal Coating, Advanced Functional Materials, 32 (2021).

[150] L. Yang, X. Liu, X. Zhang, T. Chen, Z. Ye, M.S. Rahaman, High performance nanocomposite nanofiltration membranes with polydopamine-modified cellulose nanocrystals for efficient dye/salt separation, Desalination, 521 (2022).

[151] Y. Jiang, W. Su, G. Li, Y. Fu, Z. Li, M. Qin, Z. Yuan, Highly strong luminescent chiral nematic cellulose nanocrystal/PEI composites for anticounterfeiting, Chem Eng J, 430 (2022).

[152] T. Pöhler, A. Mautner, A. Aguilar-Sanchez, B. Hansmann, V. Kunnari, A. Grönroos, V. Rissanen, G. Siqueira, A.P. Mathew, T. Tammelin, Pilot-scale modification of polyethersulfone membrane with a size and charge selective nanocellulose layer, Separation and Purification Technology, 285 (2022).

[153] C. Zhao, X. Yu, X. Da, M. Qiu, X. Chen, Y. Fan, Fabrication of a charged PDA/PEI/Al_2O_3 composite nanofiltration membrane for desalination at high temperatures, Separation and Purification Technology, 263 (2021).

[154] F.Y. Zhao, Q.F. An, Y.L. Ji, C.J. Gao, A novel type of polyelectrolyte complex/MWCNT hybrid nanofiltration membranes for water softening, J Membrane Sci, 492 (2015) 412-421.

[155] P. Li, H. Lan, K. Chen, X. Ma, B. Wei, M. Wang, P. Li, Y. Hou, Q. Jason Niu, Novel high-flux positively charged aliphatic polyamide nanofiltration membrane for selective removal of heavy metals, Separation and Purification Technology, 280 (2022).

[156] Y. Feng, H. Peng, Q. Zhao, Fabrication of high performance Mg^{2+}/Li^{+} nanofiltration membranes by surface grafting of quaternized bipyridine, Separation and Purification Technology, 280 (2022).

[157] Y. Zhang, L. Wang, W. Sun, Y. Hu, H. Tang, Membrane technologies for Li^{+}/Mg^{2+} separation from salt-lake brines and seawater: A comprehensive review, Journal of Industrial and Engineering Chemistry, 81 (2020) 7-23.

[158] L. Li, V.G. Deshmane, M.P. Paranthaman, R. Bhave, B.A. Moyer, S. Harrison, Lithium Recovery from Aqueous Resources and Batteries: A Brief Review A review of the methods to produce lithium and approaches to recycling from end-of-life lithium-ion batteries, Johnson Matthey Technology Review, 62 (2018) 161-176.

[159] Y. Ogawa, H. Koibuchi, K. Suto, C. Inoue, Effects of the Chemical Compositions of Salars de Uyuni and Atacama Brines on Lithium Concentration during Evaporation, Resource Geology, 64 (2014) 91-101.

[160] H. Vikström, S. Davidsson, M. Höök, Lithium availability and future production outlooks, Applied Energy, 110 (2013) 252-266.

[161] J.F. Song, L.D. Nghiem, X.-M. Li, T. He, Lithium extraction from Chinese salt-lake brines: opportunities, challenges, and future outlook, Environmental Science: Water Research & Technology, 3 (2017) 593-597.

[162] H. Li, Y. Li, M. Li, Y. Jin, G. Kang, Y. Cao, Improving Mg^{2+}/Li^{+} separation performance of polyamide nanofiltration membrane by swelling-embedding-shrinking strategy, J Membrane Sci, 669 (2023).

[163] W. Li, C. Shi, A. Zhou, X. He, Y. Sun, J. Zhang, A positively charged composite nanofiltration membrane modified by EDTA for $LiCl/MgCl_2$ separation, Separation and

Purification Technology, 186 (2017) 233-242.
[164] S. Zhang, R. Zhang, R. Li, Z. Zhang, Y. Li, H. Deng, J. Zhao, T. Gu, M. Long, X. Wang, S. Zhang, Z. Jiang, Guanidyl-incorporated nanofiltration membranes toward superior Li^+/Mg^{2+} selectivity under weakly alkaline environment, J Membrane Sci, 663 (2022).
[165] H. Peng, K. Yu, X. Liu, J. Li, X. Hu, Q. Zhao, Quaternization-spiro design of chlorine-resistant and high-permeance lithium separation membranes, Nat Commun, 14 (2023) 5483.
[166] K. Wang, X. Wang, B. Januszewski, Y. Liu, D. Li, R. Fu, M. Elimelech, X. Huang, Tailored design of nanofiltration membranes for water treatment based on synthesis–property–performance relationships, Chemical Society Reviews, 51 (2022) 672-719.
[167] G. Zhao, Y. Zhang, Y. Li, G. Pan, Y. Liu, Positively charged nanofiltration membranes for efficient Mg^{2+}/Li^+ separation from high Mg^{2+}/Li^+ ratio brine, Advanced Membranes, 3 (2023).
[168] G.R. Xu, Z.H. An, Min-Wang, Ke-Xu, H.L. Zhao, Q. Liu, Polyamide layer modulation for PA-TFC membranes Optimization: Developments, Mechanisms, and implications, Separation and Purification Technology, 311 (2023).
[169] A. Hu, Y. Liu, J. Zheng, X. Wang, S. Xia, B. Van der Bruggen, Tailoring properties and performance of thin-film composite membranes by salt additives for water treatment: A critical review, Water Res, 234 (2023) 119821.
[170] J. Ding, H. Wu, P. Wu, Multirole Regulations of Interfacial Polymerization Using Poly(acrylic acid) for Nanofiltration Membrane Development, ACS Applied Material Interfaces, 13 (2021) 53120-53130.
[171] X. You, K. Xiao, H. Wu, Y. Li, R. Li, J. Yuan, R. Zhang, Z. Zhang, X. Liang, J. Shen, Z. Jiang, Electrostatic-modulated interfacial polymerization toward ultra-permselective nanofiltration membranes, iScience, 24 (2021) 102369.
[172] X.M. Zhang, W.J. Yang, Q.Y. Wang, F. Huang, C.J. Gao, L.X. Xue, Tuning the nano-porosity and nano-morphology of nano-filtration (NF) membranes: Divalent metal nitrates modulated inter-facial polymerization, J Membrane Sci, 640 (2021).

[173] S.Y. Zhou, Y. Qu, B.W. Yang, Q. Zhang, J. Wang, Y.M. Lin, Z. Chen, G.P. Lu, Bio-based tannic acid as a raw material for membrane surface modification, Desalination, 555 (2023).

[174] G. Sathishkumar, K. Gopinath, K. Zhang, E.T. Kang, L. Xu, Y. Yu, Recent progress in tannic acid-driven antibacterial/antifouling surface coating strategies, J Mater Chem B, 10 (2022) 2296-2315.

[175] Q.S. Yao, S.X. Li, R.R. Zhang, L.H. Han, B.W. Su, High-throughput thin-film composite membrane via interfacial polymerization using monomers of ultra-low concentration on tannic acid - Copper interlayer for organic solvent nanofiltration, Separation and Purification Technology, 258 (2021).

[176] Z. Yang, Z.W. Zhou, H. Guo, Z. Yao, X.H. Ma, X. Song, S.P. Feng, C.Y. Tang, Tannic Acid/Fe^{3+}Nanoscaffold for Interfacial Polymerization: Toward Enhanced Nanofiltration Performance, Environ Sci Technol, 52 (2018) 9341-9349.

[177] Q. Li, Z.P. Liao, X.F. Fang, J. Xie, L.H. Ni, D.P. Wang, J.W. Qi, X.Y. Sun, L.J. Wang, J.S. Li, Tannic acid assisted interfacial polymerization based loose thin-film composite NF membrane for dye/salt separation, Desalination, 479 (2020).

[178] N. Zhang, X.J. Song, Y.Q. Chen, B. Jiang, L.H. Zhang, H.Q. Jiang, A facile and economic route assisted by trace tannic acid to construct a high-performance thin film composite NF membrane for desalination, Environmental Science-Water Research & Technology, 7 (2021) 956-968.

[179] S. Deng, Y.P. Ting, Characterization of PEI-modified biomass and biosorption of Cu(II), Pb(II) and Ni(II), Water Res, 39 (2005) 2167-2177.

[180] M.Y. Hu, W.M. Fu, K.C. Guan, R.R. Gonzales, Q.Q. Song, A. Matsuoka, Z.H. Mai, Y.H. Chiao, P.F. Zhang, Z. Li, H. Matsuyama, Regulating interfacial polymerization a multi-functional calcium carbonate based interlayer for a highly permselective nanofiltration membrane, Journal of Materials Chemistry A, 11 (2023) 8836-8844.

[181] B. Ghosh, A.K. Ghosh, R.C. Bindal, Influence of metal salts in reaction medium on performance enhancement of novel aliphatic-aromatic-based polyamide thin-film

composite osmosis membranes, Separation Science and Technology, 54 (2019) 1363-1375.

[182] M. Yassari, A. Shakeri, H. Salehi, S.R. Razavi, Enhancement in forward osmosis performance of thin-film nanocomposite membrane using tannic acid-functionalized graphene oxide, Journal of Polymer Research, 29 (2022).

[183] X. Zhang, P.-F. Ren, H.-C. Yang, L.-S. Wan, Z.-K. Xu, Co-deposition of tannic acid and diethlyenetriamine for surface hydrophilization of hydrophobic polymer membranes, Applied Surface Science, 360 (2016) 291-297.

[184] A. Kanazawa, T. Daisaku, T. Okajima, S. Uchiyama, S. Kawauchi, T. Ohsaka, Characterization by electrochemical and X-ray photoelectron spectroscopic measurements and quantum chemical calculations of N-containing functional groups introduced onto glassy carbon electrode surfaces by electrooxidation of a carbamate salt in aqueous solutions, Langmuir, 30 (2014) 5297-5305.

[185] Z. Wang, M. Han, J. Zhang, F. He, S. Peng, Y. Li, Investigating and significantly improving the stability of tannic acid (TA)-aminopropyltriethoxysilane (APTES) coating for enhanced oil-water separation, J Membrane Sci, 593 (2020).

[186] C. Shen, H. Chen, S. Wu, Y. Wen, L. Li, Z. Jiang, M. Li, W. Liu, Highly efficient detoxification of Cr(VI) by chitosan-Fe(III) complex: process and mechanism studies, J Hazard Mater, 244-245 (2013) 689-697.

[187] X. Yang, Controllable Interfacial Polymerization for Nanofiltration Membrane Performance Improvement by the Polyphenol Interlayer, ACS Omega, 4 (2019) 13824-13833.

[188] K. Chen, F.Y. Li, T. Wei, H.Y. Zhou, T.F. Zhang, S.C. Zhao, T.T. Xie, H.X. Sun, P. Li, J.S. Niu, An interlayer-based positive charge compensation strategy for the preparation of highly selective Mg^{2+}/Li^{+} separation nanofiltration membranes, J Membrane Sci, 684 (2023).

[189] S. Han, J. Zhu, A.A. Uliana, D. Li, Y. Zhang, L. Zhang, Y. Wang, T. He, M. Elimelech, Microporous organic nanotube assisted design of high performance nanofiltration membranes, Nat Commun, 13 (2022) 7954.

[190] L.L. Ye, L. Wang, Z.A. Wei, S.H. Zhou, Z.K. Yao, F.Q. Fan, Y. Mei, Thin film composite nanofiltration membrane with tannic acid-Fe(III) complexes functionalized CNTs interlayer toward energy efficient remediation of groundwater, Desalination, 552 (2023).

[191] W. Huang, Z.Y. Wang, F. Xie, H.Z. Ding, W.X. Li, X.K. Liang, X.H. Ma, Z.L. Xu, High performance polyamide TFC reverse osmosis membrane fabricated on co-deposition hydrophilic modified polyethylene substrate, Desalination, 538 (2022).

[192] L. Wang, D. Rehman, P.F. Sun, A. Deshmukh, L. Zhang, Q. Han, Z. Yang, Z. Wang, H.D. Park, J.H. Lienhard, C.Y. Tang, Novel Positively Charged Metal-Coordinated Nanofiltration Membrane for Lithium Recovery, ACS Applied Material Interfaces, 13 (2021) 16906-16915.

[193] Y. Zhang, W.-S. Zou, W. Kong, X. Chen, W. Li, X. Huang, Y. Wang, Dual integration of amine-functionalized carbon dots endowed nanofiltration membranes with highly efficient biofouling/ acid/chlorine resistance for effective Mg^{2+}/Li^{+} separation, J Membrane Sci, 696 (2024).

[194] P. Zhao, F. Guo, L. Wang, H. Zhen, N. Zhang, S. Yin, G. Zhou, X. Ruan, G. He, X. Jiang, Nanofiltration membrane with modified nano-gradient structure and positive charge for Li separation from high Mg/Li ratio brine, Desalination, 577 (2024).

[195] M.B.M.Y. Ang, C.-L. Tang, M.R. De Guzman, H.L.C. Maganto, A.R. Caparanga, S.-H. Huang, H.-A. Tsai, C.-C. Hu, K.-R. Lee, J.-Y. Lai, Improved performance of thin-film nanofiltration membranes fabricated with the intervention of surfactants having different structures for water treatment, Desalination, 481 (2020).

[196] R. Dai, J. Chen, H. Han, H. Zhou, Z. Wang, Interfacial Wettability Regulation Enables One-Step Upcycling of the End-of-Life Polymeric Microfiltration Membrane, Acs Est Eng, 3 (2022) 479-486.

[197] X. Li, Z. Wang, X. Han, Y. Liu, C. Wang, F. Yan, J. Wang, Regulating the interfacial polymerization process toward high-performance polyamide thin-film composite reverse osmosis and nanofiltration membranes: A review, J Membrane Sci, 640 (2021).

[198] I. Nulens, A. Ben Zvi, I.F.J. Vankelecom, G.Z. Ramon, Re-thinking polyamide thin film formation: How does interfacial destabilization dictate film morphology?, J Membrane Sci, 656 (2022).

[199] L. Dai, F. Xu, K. Huang, Y. Xia, Y. Wang, K. Qu, L. Xin, D. Zhang, Z. Xiong, Y. Wu, Ultrafast water transport in two-dimensional channels enabled by spherical polyelectrolyte brushes with controllable flexibility, Angewandte Chemie, 133 (2021) 20086-20094.

[200] J. Chen, R. Li, S. Liu, W. Li, J. Zhang, X. Wu, J. Wang, Surfactant-assisted interfacial polymerization towards high-crystallinity COF membranes for organic solvent nanofiltration, J Membrane Sci, 694 (2024).

[201] Q.S. Qin Shen, Zhaohuan Mai*, Kueir-Rarn Lee, Tomohisa Yoshioka,, R.R.G. Kecheng Guan, Hideto Matsuyama*, When self-assembly meets interfacial polymerization, SCIENCE ADVANCES, (2023).

[202] B. Naskar, A. Dey, S.P. Moulik, Counter-ion effect on micellization of ionic surfactants: a comprehensive understanding with two representatives, sodium dodecyl sulfate (SDS) and dodecyltrimethylammonium bromide (DTAB), Journal of Surfactants and Detergents, 16 (2013) 785-794.

[203] Z. Chen, J. Penfold, P. Li, J. Doutch, Y. Fan, Y. Wang, Effects of length and hydrophilicity/hydrophobicity of diamines on self-assembly of diamine/SDS gemini-like surfactants, Soft Matter, 13 (2017) 8980-8989.

[204] Y. Mansourpanah, S.S. Madaeni, A. Rahimpour, Fabrication and development of interfacial polymerized thin-film composite nanofiltration membrane using different surfactants in organic phase; study of morphology and performance, J Membrane Sci, 343 (2009) 219-228.

[205] C. Jiang, L. Tian, Z. Zhai, Y. Shen, W. Dong, M. He, Y. Hou, Q.J. Niu, Thin-film composite membranes with aqueous template-induced surface nanostructures for enhanced nanofiltration, J Membrane Sci, 589 (2019).

[206] Y. Cui, X.-Y. Liu, T.-S. Chung, Enhanced osmotic energy generation from salinity gradients by modifying thin film composite membranes, Chem Eng J, 242 (2014) 195-

203.

[207] N. Yang, K. Li, Y. Hao, L. Zhang, Y. Sun, L. Zhang, B. Jiang, Advanced Mg^{2+}/Li^{+} separation nanofiltration membranes fabricated with Girard's reagent T based on functional end-capping strategy, J Membrane Sci, 695 (2024).

[208] F. Azarteimour, M. Amirinejad, M. Parvini, M. Yarvali, Organic phase addition of anionic/non-ionic surfactants to poly (paraphenyleneterephthalamide) thin film composite nanofiltration membranes, Chemical Engineering and Processing: Process Intensification, 106 (2016) 13-25.

[209] S. Fang, K. Guan, S. Zhou, Q. Song, Y. Shi, W. Fu, Z. Li, P. Xu, M. Hu, Z. Mai, P. Zhang, H. Matsuyama, Ternary-coordination-regulated polyamide nanofiltration membranes for Li^{+}/Mg^{2+} separation, Desalination, 581 (2024).

[210] L.-F. Fang, M.-Y. Zhou, L. Cheng, B.-K. Zhu, H. Matsuyama, S. Zhao, Positively charged nanofiltration membrane based on cross-linked polyvinyl chloride copolymer, J Membrane Sci, 572 (2019) 28-37.

Publication list

Chapter 2:

Fang S, Guan K, Mai Z, et al. Complexation of cellulose nanocrystals and amine monomer for improved interfacial polymerization of nanofiltration membrane [J]. Journal of Membrane Science, 2023, 687: 122048.

Chapter 3:

Fang S, Guan K, Zhou S, et al. Ternary-coordination-regulated polyamide nanofiltration membranes for Li^{+}/Mg^{2+} separation [J]. Desalination, 2024, 581: 117577.

Chapter 4:

Fang S, Guan K, Zhang A, et al. Multifunctional role of surfactant-controlled polyamide membranes for highly efficient Li^{+}/Mg^{2+} separation. (Submitted).

Doctoral Dissertation, Kobe University
"Development of advanced nanofiltration membranes for Mg^{2+}/Li^{+} separation (Mg^{2+}/Li^{+}分離のための革新的ナノろ過膜の開発)", 128 pages

Submitted on July 2, 2024
When published on the Kobe University institutional repository */Kernel/*, the publication date shall appear on the cover of the repository version.